UNIVERSIDAD CARLOS III DE MADRID

Corner Waves downstream from a partially submerged vertical plate.

Tesis Doctoral

Autor
Pablo Martínez-Legazpi

Directores
Javier Rodríguez-Rodríguez Juan C. Lasheras

Leganés, Octubre 2011

DEPARTAMENTO DE INGENIERÍA TÉRMICA Y DE FLUIDOS
Escuela Politécnica Superior

Corner Waves downstream from a partially submerged vertical plate.

Olas de Esquina aguas abajo de una placa parcialmente sumergida

Autor
Pablo Martínez-Legazpi

Directores de Tesis
Javier Rodríguez-Rodríguez Juan C. Lasheras

Leganés, Octubre 2011

A mi abuela.
A mis padres y hermanos.
A Diana.

Tesis doctoral

Corner Waves downstream from a partially submerged vertical plate.

Autor: Pablo Martínez-Legazpi

Directores de Tesis: Javier Rodríguez-Rodríguez Juan C. Lasheras

Firma del Tribunal Calificador:

Firma

Presidente: D. Alexander Korobkin
Vocal: D. Antonio Souto-Iglesias
Vocal: D. Jose Manuél Gordillo
Vocal: D. Carlos Martínez-Bazán
Secretario: Da. Carolina Marugán Cruz
Suplente: D. Alejandro Sevilla Santiago
Suplente: D. Wilfried Coenen

Calificación:

Leganés, 2 de Diciembre de 2011

Contents

Agradecimientos

Esta tesis no podría haberse llevado a cabo sin la ayuda y dedicación, principalmente de una persona: Javier Rodríguez-Rodríguez. A él tengo que agradecerle mucho más que acabar (finalmente) esta tesis. Javier me ha eseñado, predicando siempre con el ejemplo, no solo las herramientas para conseguir entender un problema científico, sino además, la ética, el esfuerzo y la dedicación necesarias. Como él mismo diría, "un mol de gracias".

Esta tesis y, es más, la idea de las olas de esquina, no hubiera existido de no ser por Juan C. Lasheras. Juan me acogió con los brazos abiertos en su grupo de investigación durante mis estancias en Universidad de California San Diego brindándome siempre todo el cariño y la ayuda necesaria para poder realizar allí mis campañas experimentales.

También debo agradecer a Antonio Sanchez la oportunidad que me brindó, allá en la lejanía, de empezar a trabajar en temas científicos y, por meterme el gusanillo de la investigación que tantos pequeños disgustos y grandes alegrías proporciona.

I want to thank, from these lines, the kindness and the wisdom of Professor Alexander Korobkin, who opened our eyes when we needed it most.

Durante estos años de doctorado, muchas son las personas del departamento de Ingeniería Térmica y de Fluidos de la Universidad Carlos III de Madrid a las que tengo que agredecer su apoyo y amistad. En general me gustaría dar las gracias a todas las personas de los grupos de investigación de Mecánica de Fluidos y del ISE y en particular a Ana, Mario, Nano, Nestor, Jorge, Sergi, Imma, Ulpi, Wil, Toni, Dani, Domingo y, especialmente, a Carol y Alejandro, que arrimaron el hombro y me ayudaron cuando más lo necesitaba. Tampoco me puedo olvidar de los técnicos de laboratorio del grupo de Mecánica de Fluidos, Isra y David, siempre a punto para echar una mano con los experimentos. Por último, pero no menos importante, agradecer el cariño y la amistad de Cristina Peraleda y Maria Pavón. Perdón si me olvido de alguien.

Baldo, Juancar y Urzay fueron mis compañeros de fatigas en California, a ellos también quiero agraderles su amistad y su impagable ayuda.

Quiero agradecer y dedicar esta tesis a mi familia y amigos, que son siempre la principal fuente de apoyo y ánimo en todos los aspectos de mi vida. Finalmente quiero a darle especialmente las gracias a Diana, solamente por ser como es.

Abstract

In this dissertation, the high-Reynolds-number flow near the corner of a vertical flat plate partially submerged across an uniform stream has been studied using a combination of experimental, numerical and analytical tools. In this configuration, a three dimensional wave forms at the corner of the plate which evolves downstream in a similar way as a time-evolving two dimensional plunging or spilling breaker, depending the occurrence of one or the other type of breaker on the flow conditions.

Experiments have been performed submerging a flat plate perpendicular to the free stream in the test section of a recirculating water channel. Experimental results show that the formation and the initial development of the wave is nearly unaffected by the presence of the channel walls and bottom even when their distance to the corner, where the wave originates, is of the order of the size of the wave itself. This is a remarkable observation, that suggests that the formation of the corner wave is a local process in a sense that it is only influenced by the characteristics of the velocity field very near the corner. Moreover, it has been observed that the jet formed when the corner wave adopts the plunging breaker configuration follows a nearly ballistic trajectory, has is the case in two-dimensional unsteady plunging breakers.

Theoretical analysis shows that, taking advantage of the slender nature of the flow, the 3D steady problem can be transformed into a two dimensional unsteady one using the so called 2D+T approximation. Together with the high Reynolds number of the flow, the 2D+T approximation makes the problem amenable to be simulated numerically using a Boundary Element Method (BEM).

Moreover, a pressure-impulse asymptotic analysis of the flow near the origin of the corner wave has been performed in order to describe the initial evolution of the wave and to clarify the physical mechanisms that lead to its formation. The analysis shows that the flow near the corner exhibits a self similar behavior at short times.

The problem considered in this dissertation is of interest in naval hydrodynamics as well as oceanography. Indeed, the flow resembles to the one found at the dry stern of high-speed surface vessels. The similarities between the waves formed in the wake of such ships and our laboratory breakers will be investigated. This experiment also shares many features with deep water waves in the ocean, and thus it will be applied to the study of their breaking process. A criterion for the transition between overturning laboratory

waves and spilling ones is proposed.

This work has been sponsored by the ONR through grant N00014-05-1-0121.

Resumen

En esta tesis se ha estudiado el flujo a altos números de Reynolds aguas abajo de la esquina de una placa vertical parcialmente sumergida en una corriente uniforme, usando para tal fin una combinación de herramientas experimentales, numéricas y analíticas. Este flujo se caracteriza por la aparición de una ola estacionaria, que permanece unida a la esquina de la placa. Tanto la amplitud como la pendiente del frente de la ola crecen a medida que la ola evoluciona aguas abajo de la placa, dando lugar ya sea, a una rotura de la ola en la cual la cresta se derrama sobre la propia ola, o a una rotura en forma de tubo.

Para estudiar este flujo experimentalmente, se sumergió una placa perpendicularmente a una corriente uniforme en un canal de recirculación. Los resultados experimentales demuestran que la presencia de las paredes y el suelo del canal no afectan a la formación y el desarrollo inicial de la ola, incluso cuando dichas paredes se encuentran a distancias del orden de magnitud de la propia ola. Esta es una observación importante dado que sugiere que la formación de la ola es un proceso local, en el sentido de que solamente se ve afectado por el campo de velocidades cerca de la esquina. Complementariamente se ha observado que, cuando la ola rompe en forma de tubo, la cresta de la ola sigue una trayectoria balística, al igual que en las olas en aguas profundas.

El análisis teórico muestra que, haciendo uso de la naturaleza esbelta del flujo, el problema tridimensional estacionario se puede transformar en un problema bidimensional no estacionario mediante el uso de la, así llamada, aproximación 2D+T. Combinando los altos números de Reynolds encontrados en el flujo con el uso de dicha aproximación, el problema puede ser tratado numéricamente mediante un método de elementos de contorno.

Para investigar el mecanismo físico que conduce a la formación de la ola y su posterior desarrollo, un análisis asintótico de la presión impulsiva en el flujo se ha llevado a cabo, capturándose con fiabilidad la evolución, a tiempos cortos, de la cresta de la ola, la cual se demuestra que exibe un comportamiento auto semejante en las etapas iniciales.

El problema considerado en esta tesis es de gran interés tanto en oceanografía como en el campo de la investigación naval. De echo, este flujo recuerda al que se encuentra aguas abajo de las popas de espejo en barcos de superficie de alta velocidad. En esta tesis se investiga la semejanza entre las olas que se forman en la estela de dichos barcos y las generadas en el laboratorio. Adicionalmente, se observa que las olas obtenidas en el laboratorio también comparten muchas características de las olas en aguas profundas, por

lo que se propone un criterio para separar ambos regímenes de rotura.

Este trabajo ha sido parcialmente patrocinado por la O.N.R. mediante el proyecto N00014-05-1-0121.

CHAPTER
ONE

Introduction

1.1 Introduction and Motivation

The structure of the wake generated by high-speed vessels has been studied over the last seventy years, contributing to the understanding of several important phenomena associated to current endeavors in naval hydrodynamics. Examples are the quantification of the drag force experienced by the ship, Newman (1977), the mass and energy transfer between the ocean and the atmosphere, the development of accurate tools for ship-maneuvering modeling, Molland (2008), and the design of reliable marine structures, Sumer & Fredsoe (1997).

Nonetheless, there still remain various challenges that are of paramount importance for the propulsive efficiency of high-speed vessels, and, in particular, for the prediction of the acoustic signature of the ships and, for unveiling the dynamics of some, non well known, aspects of the wake and the rooster tail.

In this thesis, the formation, development and breaking processes of a particular wave that emerges downstream from the side of the stern of high-speed vessels have been studied using numerical, experimental and analytical tools. In addition, this work explores the possibility of connecting the above mentioned wave with its deep-water counterpart.

1.1.1 Flow around High Speed Vessels

Any ship moving at a certain velocity through water creates a disturbance in the water surface which is manifested by a wave pattern. This wave pattern moves seemingly locked to the ship and it is a very significant, and at high speed even the dominant, portion of the ship's resistance. Through many years of analytical and experimental research, this wave pattern has been found to be directly related to the ratio of the inertia of the body to the gravitational forces and thus, to the Froude number, Fr.

The Froude number was originally introduced in open channel flow problems as the fraction of the flow velocity to the square root of the gravity acceleration times the flow

depth. Early in the XIX century it was found out that, if this quantity exceeded a critical value, $Fr = 1$, the information carried by the flow travels faster than the wave velocity and any disturbance to the flow does not propagate upstream. Resembling the "supersonic" nomenclature used in aerodynamics, these flows were called supercritical flows.

In naval hydrodynamics the value of the Froude number has been found to be determinant to quantify the resistance of ships, which was related, by the early Froude's experiments, with the shape of the waves caused by moving a hull through the water, Wright (1983). These waves, originated by the interaction of the hull with the sea, can be decomposed into three different types: bow waves, which arise at the bow of a ship. Kelvin waves, that produce a well-known free surface pattern downstream from the ship, at a fixed angle of 19.5°; and stern waves, which emerge downstream from the stern of the ship, Sorensen (1966). All of these contribute, with a certain weight, to the shape of the overall wake downstream the hull. A preliminary work which formulates the asymptotic behavior of the wake generated by a ship was done by Peregrine (1971).

To investigate the influence of the Froude number on the shape of the wake, the former is usually defined as the ratio of the ship's velocity U, to a characteristic length scale of the problem, being able to choose either the draught H or the ship's beam L. In works on wakes generated by high-speed vessels, the first of these is commonly accepted, i.e.

$$Fr = \frac{U}{\sqrt{gH}}. \tag{1.1}$$

When the Froude number is less than unity, the flow downstream from the stern is subcritical, and the wake could exhibit some features of a hydraulic jump, which is characterized by large unsteady eddies that produce considerable atmosphere-ocean air and momentum exchange, Rodríguez-Rodríguez *et al.* (2011). However, when the ship increases its velocity, while keeping constant its draught, and the flow becomes supercritical ($Fr > 1$), the wake acquires a very characteristic shape producing lower air entrainment. Figure 1.1 shows the dependence of the shape of the wake on an increasing Froude number using a ship model, in a towing tank at the Carderook Division.

Among other features, during high speed cruise, separation of the flow occurs at the intersection of the boards with the stern plane. The difference in height between the separated stream and the free surface level immediately downstream the stern induces a transversal velocity component to the separated water mass that deflects its otherwise stream-wise velocity towards the centerline of the hull. As a result, two symmetrical waves are formed that collide near the center plane of the wake.

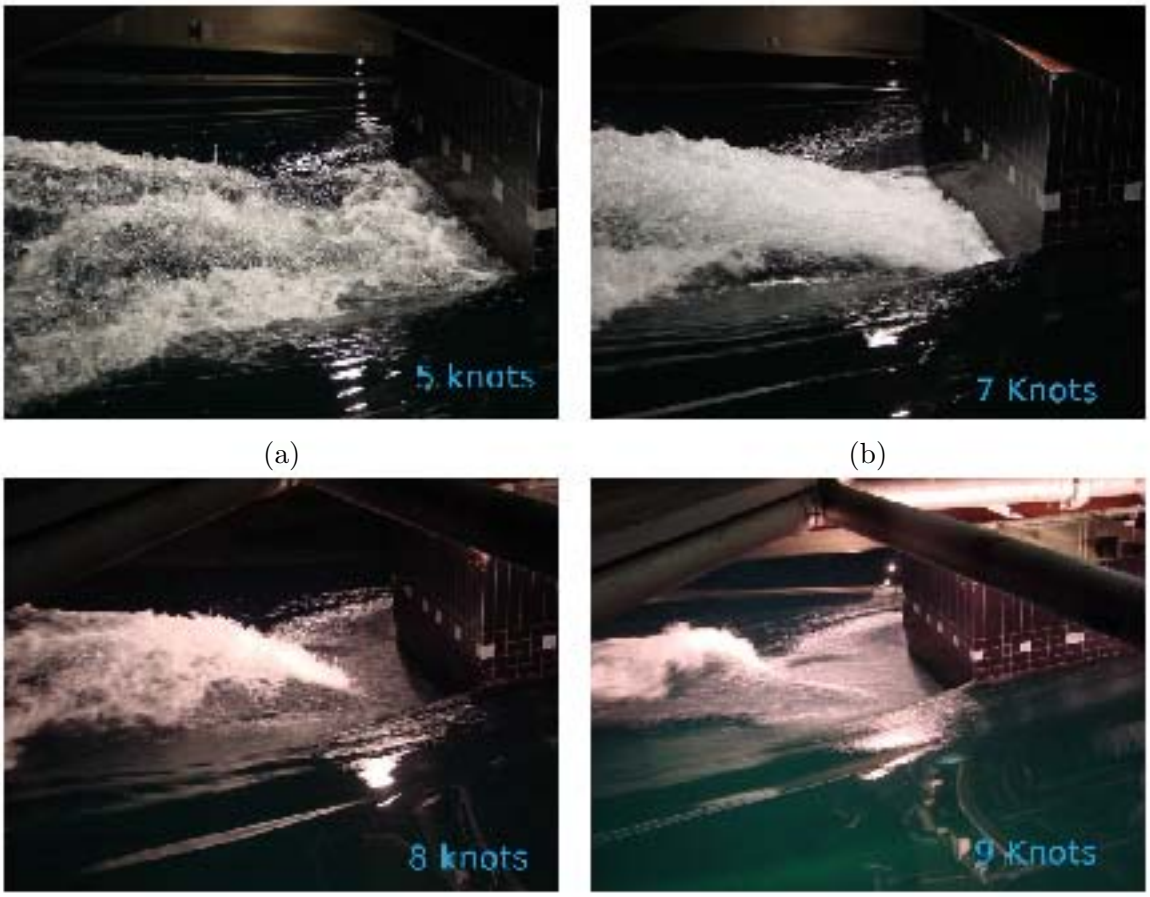

(a) (b)

(c) (d)

Figure 1.1: Different wake structures downstream from the stern of a ship for different ship velocities, keeping a constant draught. (a)= 5kn, (b)= 7kn, (c)= 8 kn, (d) 9 kn. Courtesy of Thomas Fu. Carderook Division, MD, USA.

Figure 1.2: A typical shape of a wake found in high-speed vessels. Notice that the structure known as rooster tail is born, in part, by the collision of the pair of waves, which raise from the corner and evolve towards the centerline of the hull.

The collision of these waves leads to a structure, known as *rooster tail*, which is responsible for an important fraction of the total amount of air entrainment and energy dissipation in the wake, as can be seen in figure 1.2.

This work focuses on the formation, growth and development of the above mentioned pair of waves, which, from this point on, will be called *corner waves*.

1.1.2 High Froude-Reynolds free surface flows

High Froude-Reynolds free surface flows flows around bodies often exhibit a strong nonlinear character, implying jet generation, breaking waves and air entrainment. This particular feature converts the possibility of obtaining exact solutions for these flows in an herculean task, mainly due to the non-linear boundary conditions at the free surface. Therefore, in an effort to facilitate accurate and simplified solutions, many authors made use of the slender-body theory. Tulin (1957) implemented this theory to a planing ship, obtaining reduced equations with errorless results, while Ogilvie (1967) evaluated the feasibility of formulating analytical and appropriate expressions for these problems.

The application of slender-body theory to steady-motion problems of ship hydrodynamics retains some features of the classical theory of aerodynamics, taking into account that free-surface flow problems involve extra difficulties.

In particular, depending on the the slenderness ratio of the ship and on the order of magnitude of the Froude number, different approaches must be taken. In naval hydrodynamics, it is common to express this slenderness ratio, ϵ, by the beam/length ratio, W/L, or the draught/length ratio, H/L, where L is usually assumed to be of order unity, $L \sim 1$.

Unlike in aerodynamics, when slender-body theory is applied to free surface flows, the gravitational terms should be evaluated, being commonly accepted $g = O(1)$. However, depending on the order of magnitude of gravity, four different types of problems, as explained in Ogilvie (1967), are found:

- $g = O(\epsilon^{-1})$. Gravity rules the free-surface conditions.
- $g = 0(1)$. Gravity is the leading parameter near the body and, at large distances from the body, there exists the possibility of finding gravity waves.
- $g = O(\epsilon)$ Gravity waves appear near the body, but gravity effects disappear far away.
- $g = O(\epsilon^2)$. The effects of gravity are neglected. This is the usual planing case.

It will be shown that the waves under study in this work can be described using the slender-body theory, taking $g = 0(1)$.

1.1.3 The 2D +T idea

Characterizing the free surface evolution and the velocity field in a steady three-dimensional high-Reynolds number flow, involves the resolution of a system of elliptic non-linear partial differential equations. However, when the Froude number is large enough, there exists an approximation that reduces the complexity of the problem. Such approximation takes advantage of the duality between steady slender three-dimensional flows and two-dimensional unsteady flows and is commonly known as 2D+1/2 or 2D+T theory. Tulin (1957) used this method for the analysis of high speed/low ratio vessels, while Tulin & Wu (1997), calculating bow waves, showed that this method can be used with very good results for ships at sufficiently high speed or, in other words, in flows with large Froude numbers. Since then, the applications of the 2D+T approximation in naval hydrodynamics have been numerous and fruitful (see the review article by Fontaine & Tulin (1998) and references therein).

The 2D+T approximation was first proposed by Max Munk (1924) to study the aerodynamics of slender bodies and Wagner (1932), made use of the approximation to formally associate the problem of a slender body planing on water with that of a plate impacting on a free surface.

Since that pioneering work, the method has been applied in free surface hydrodynamics mainly to simplify theoretical and numerical computations of the wave pattern around slender ship hulls, as well as for the loads they produce.

More recently, the 2D+T approximation has been used to study experimentally the dynamics of bow waves induced by slender hulls in a laboratory water channel as i.e. by Shakeri *et al.* (2009*a*,*b*). In these studies, it was found that the 2D+T approximation grants good results compared with fully 3D cases, see i.e. Iafrati & Broglia (2010).

The 2D+T approximation, reduces the 3D problem to a continuous sequence of unsteady 2-D problems in the cross-stream section, each one of which, assuming potential flow theory, can be solved using, i.e., a boundary element method (BEM). This method has demonstrated providing accurate results including in case of overturning jets.

It must be pointed out that, apart from its application to naval hydrodynamics, the 2D+T approximation is commonly applied to study flows where the free surface of a liquid, moving with a uniform speed, U, is steadily perturbed, originating height differences of size, h, provided $U \gg (gh)^{1/2}$. Under these conditions, the perturbation would propagate laterally (i.e. perpendicularly to the free stream) with speeds of the order $v \sim (gh)^{1/2} \ll U$. Therefore, by the time the perturbation has moved laterally a distance, y, it has been advected by the free stream a distance $L \sim y\,\mathrm{Fr}_h \gg y$, where $\mathrm{Fr}_h = U/(gh)^{1/2}$ is the Froude number. Thus, the flow can be considered slender, with an aspect ratio of the order of the inverse of the Froude number. More importantly, since variations in the streamwise velocity component are also of order v, the advection of the perturbation wave nearly occurs at the uniform velocity, U, which justifies the validity of the 2D+T formulation of slender flows.

1.1.4 *Corner Waves* downstream a partially submerged vertical plate

Figures 1.1 (d) and 1.2 show that the rooster tail is partially formed, *a priori*, as a result of the collision between the two twin corner waves that originate in each side of the stern. However, when trying to understand the dynamics that forms the rooster tail, it becomes clear that there exists many sources of information that must be previously detached. For this reason, a logical first step must be to study these waves separately.

Each one of these waves can be qualitatively reproduced, and isolated, in a recirculating water channel by using a simple experimental set-up, thus allowing an initial approach to fully understand the whole flow pattern.

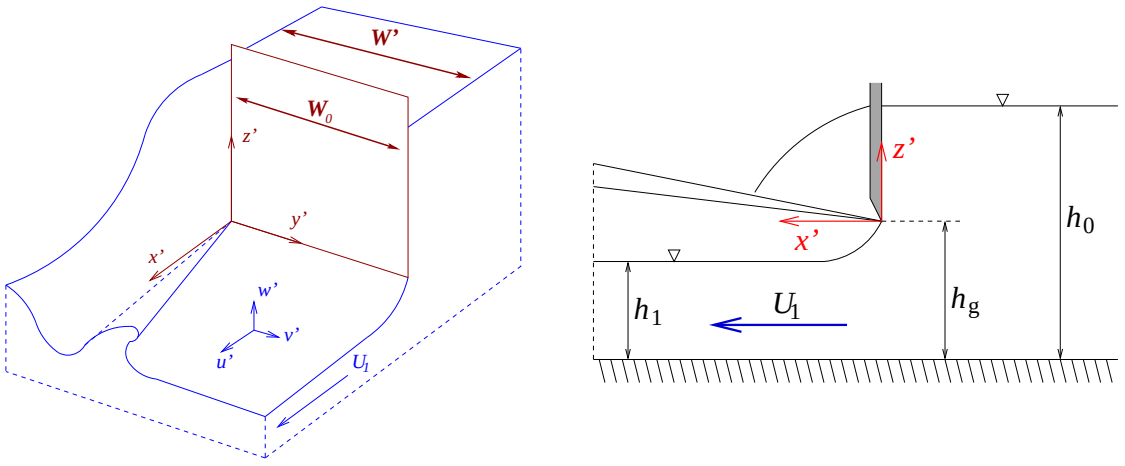

(a) (b)

Figure 1.3: Sketch of the flow set-up. (a) General view. (b) Side (x-z) view.

The experiment consists in the positioning of a vertical plate, with smaller width, W_0, than the channel one, W', partially submerged and perpendicular to an uniform stream, as sketched in figure 1.3. As mentioned above, the main feature of this flow is the formation of a three dimensional steady wave, qualitatively identical to the corner wave one and which retains its slender nature. The wave originates at corner of the plate and develops in the downstream direction in a similar way as a two dimensional wave evolves in time. Similarly to the two-dimensional case, the crest advances along the spanwise direction while the wave amplitude grows, which eventually leads, depending on the flow parameters, to the formation of either a plunging or a spilling breaker. As will be shown later, a remarkable characteristic of this wave is that its evolution and breaking are relatively unaffected by the presence of the channel side and bottom walls, even when their distances to the wave are comparable to the wave amplitude. These observations raise the following question: to what extent this simple laboratory flow can be considered to reproduce the physical processes that are involved in the corner waves observed in real transom flows and, in addition, can this experimental steady wave be used to study the time evolution and breaking of two-dimensional waves in deep waters?.

It ought to be underlined that, besides the applications in naval hydrodynamics, the experiment considered here is connected with a classical problem in civil engineering, namely the flow under a sluice gate. The first problem has been widely studied in the case of a two-dimensional gate, see for instance Benjamin (1956), Naghdi & Vongsrnpigoon (1986) or Vanden-Broeck (1986). However, very little has been published about the waves originated at the corner of the gate when it has a finite span. To the best of our knowledge, only Hager & Mazumder (1992) and Hager & Yasuda (1997) have considered this flow. In

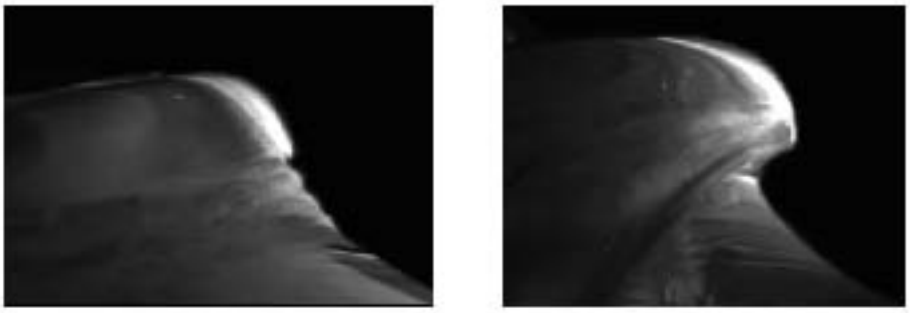

(a) (b)

Figure 1.4: Two images of different breaking conditions of the experimental corner wave. (a)Spilling breaker. (b)Plunging breaker. Notice that, in the spilling breaker configuration, the capillary ripples and the toe observed by Duncan *et al.* (1999) in unsteady deep-water waves are reproduced.

these papers, the authors integrate numerically the shallow water equations applying the 2D+T analogy to describe the flow in a sudden expansion of a channel. Although this flow has some similarities with the one described above, the fact that the waves formed there propagate on a dry basin changes completely their behavior with respect to ours. In fact, when treated with the 2D+T approximation, the problem of the sudden expansion is analogous to the classical dam-break problem, which differ considerably from ours.

1.1.5 Breaking waves in deep water

It is well known that breaking waves in deep waters play a very important role in the atmosphere-sea interaction and in energy exchange in the ocean. Furthermore, the study of the dynamics of the deep-water breaking process is important in the estimation of the mechanical loads that ships encounter in extreme sea conditions. The breaking process of these waves has been widely studied in the past (see i.e, Rapp & Melville (1990), Schultz *et al.* (1994), Banner & Peregrine (1993) or Bonmarin & Ramamonjiarisoa (1985)) and, attending to the way they break, they are usually divided into two different types: plunging breakers, in which the crest separates from the wave, as early described by Galvin (1968), and spilling ones, in which the crest tumbles down the front or face of the wave, (see the review Duncan (2001)). However, despite the large amount of studies on this subject, the unsteadiness associated to the breaking process entails a lack of detail in the experimental results, which can be over-passed using a steady wave, as the one presented in this work.

For example, using this laboratory set up, the transition between the different breaker configurations can be parametrically studied. Figure 1.4 shows examples of both kind of

breakers observed in the laboratory corner wave and its similarities with deep water ones.

1.1.6 Summary

With the above ideas in mind, this thesis is structured as follows: in chapter 2, the flow is presented and formulated, and some dimensionless parameters are defined based in the 2D+T approximation theory. In chapter 3, the experimental facility, the measurement techniques and the experimental results are described.

In chapter 4, some numerical receipts which describe the corner wave flow are tested and validated with the experimental evidences of chapter 3. Interestingly, it will be shown that, although strictly speaking the 2D+T is applicable only for large Froude numbers, the approximation, in the considered flow, remains valid also for moderate values. This observation, together with the *small* effect that the presence of the channel walls and the finite depth, will be demonstrated to have on the corner wave trajectories, allow the extrapolation of some of the results obtained in this simple laboratory flow to more complex flows found in nature as well as in ocean engineering applications.

In chapter 5, the formation, the initial evolution and the development of the corner wave are studied and a discussion about the self-similar structure of the flow at short times is presented. Finally, chapter 6 is committed to conclusions.

CHAPTER
TWO

Problem Formulation

2.1 Corner Wave flow description

This chapter is devoted to formulate the Corner Wave flow, which is the flow around a vertical plate partially submerged into a recirculating water channel, wider than the plate width. The highlighting aspect of this flow resides in the formation and development of a wave, which arises from the corner of the plate and whose front is bent towards the centerline of the resulting wake.

As sketched in figure 2.1, the flow around a vertical plate that is partially submerged into a recirculating water channel of width W', wider than the plate width W_0, is considered. The streamwise, spanwise and vertical coordinates are denoted as x', y' and z' respectively, and the origin of coordinates is placed at the corner of the plate. The lower edge of the plate is at a distance h_g above the bottom of the channel, whereas the water level upstream from the plate has a depth h_0.

Except for a region near the corner of the plate, where three-dimensional effects are important, the flow downstream from the plate behaves exactly as a two-dimensional sluice gate: after a short distance where the depth decreases due to the *vena contracta* effect, a uniform height $h_1 < h_g$ is attained. This depth, h_1, the lowest water level found in this configuration, plays a central role in the flow. Indeed, all the relevant lengths that will be used to determine the dimensionless parameters, will be defined below as height differences with respect to h_1. The velocity distribution in the region of depth h_1 has an almost uniform value, U_1, as has been reported in similar flows, i.e Roth & Hager (1999) or Kim (2007). This velocity can be estimated applying the continuity equation and energy conservation to a streamline connecting the free surface upstream and downstream the plate:

$$U_1 \cdot h_1 = U_0 \cdot h_0 \tag{2.1}$$

$$h_0 + \frac{U_0^2}{2g} = h_1 + \frac{U_1^2}{2g} \tag{2.2}$$

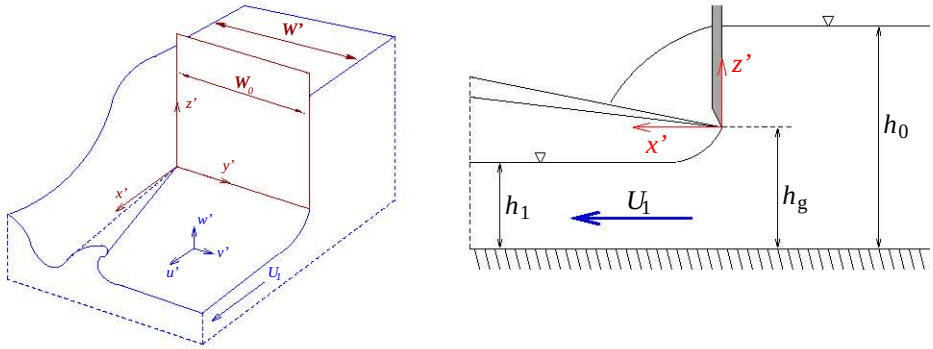

(a) (b)

(c) (d)

Figure 2.1: (a) and (b). Sketch of the flow set-up. (a) General view. (b) Side $(x-z)$ view. (c) and (d), Two views of the flow configuration under typical experimental conditions. (c) Top view. (d) Side view.

Combining both equations, U_1 results,

$$U_1 = \sqrt{\frac{2gh_0}{1+\frac{h_1}{h_0}}}, \tag{2.3}$$

which can be taken as the characteristic velocity of the problem in absence of an experimental one. Except for this velocity, the rest of the flow parameters used hereafter will be defined solely as a function of height differences with respect to the minimum depth, h_1. As will be explained later, this procedure will allow the connection of the results obtained in this experiment with deep water waves.

In particular, two lengths that may be defined are $\delta = (h_g - h_1)$ and $\Delta h = (h_0 - h_1)$. The former is the reduction of the depth in the *vena contracta* region, which coincides with the height between the point where the corner waves originates and the downstream depth. The later is the maximum height difference of the free surface. The ratio between both magnitudes, $\Delta h^* = \frac{\Delta h}{\delta} = \frac{h_0 - h_1}{h_g - h_1}$, can be interpreted as a measure of the potential energy which is at disposal in the flow in order to rise up the wave.

2.2 Problem formulation

The system of equations that describes the formation and development of the corner wave is based in two realistic hypotheses that will be confirmed by the experiments of chapter 3. On one hand, the Reynolds number is assumed to be large, $Re \sim 10^5$, taking in account the characteristics scales found in the problem, $\Delta h \sim 10^{-1}$m and $U_1 \sim 1$ m/s. Consequently, the viscous terms will be neglected. On the other hand, the Webber number is considered large enough, $We \sim 10^4$, neglecting therefore, the surface tension terms.
These two hypotheses merge in the Euler equations, which describe the velocity field, $\vec{u'} = (u', v', w')$ and the evolution of the free surface $h'(x', y')$ downstream from the plate, where h' can be multi-valued:

$$\begin{aligned} \partial_{x'}u' + \partial_{y'}v' + \partial_{z'}w' &= 0 \\ u'\partial_{x'}u' + v'\partial_{y'}u' + w'\partial_{z'}u' &= -\rho'^{-1}\partial_{x'}p' \\ u'\partial_{x'}v' + v'\partial_{y'}v' + w'\partial_{z'}v' &= -\rho'^{-1}\partial_{y'}p' \\ u'\partial_{x'}w' + v'\partial_{y'}w' + w'\partial_{z'}w' &= -\rho'^{-1}\partial_{z'}p' - g' \end{aligned} \tag{2.4}$$

This system must be completed with the boundary conditions at the channel walls, as well as at the free surface, $F'(x', y') = z' - h'(x', y') = 0$. The former are the usual zero normal velocity conditions, $\partial_{\vec{n}}\vec{u'} = 0$, whereas the latter, taking into account that the free surface is a fluid surface, might be written as:

$$\begin{aligned} u'\partial_{x'}h' + v\partial_{y'}h' - w' &= 0 \\ p' &= p_a \end{aligned} \tag{2.5}$$

where $z' = h'(x', y')$ in $(x' > 0, -(W' - W_0) < y' < W_0)$.
The formulation of the problem is supplemented by the consideration of the supercritical character of the flow, and therefore, an appropriate defined Froude number,

$$Fr_{\Delta h} = \frac{U_1^2}{g\Delta h}, \tag{2.6}$$

is assumed to be much larger than unity, $Fr_{\Delta h} \gg 1$. For simplicity, in the rest of this chapter $Fr_{\Delta h}$ will be written as Fr.

For an irrotational flow, as the one described by the equations (2.4-2.5), the curl of the velocity is zero $\nabla \times \vec{u'} = 0$. It then follows, that the condition of irrotationality can be identically satisfied by choosing a scalar function $\phi' = \phi'(x', y'z')$, such that the velocity is defined as its gradient $\vec{u'} = \nabla\phi'$. This scalar function, has been traditionally referred to as the velocity potential, and the flow as a potential flow. Applying the velocity potential

definition to the continuity equation, it becomes possible to represent the flow by the Laplace's equation, instead of the coupled system of nonlinear Euler equations:

$$\nabla^2\phi' = \phi'_{x'x'} + \phi'_{y'y'} + \phi'_{z'z'} = 0 \tag{2.7}$$

Equation (2.7) remains valid in the domain Ω, where $\Omega = (x' > 0, -(W' - W_0) < y' < W_0, -h_g < z' < h'(x', y'))$, unknown in advance. Complementing the Laplace's equation and using the potential flow formulation, the boundary conditions become:

$$\begin{aligned} \partial_{y'}\phi' = 0 \qquad \text{in} \qquad & (y' = -(W' - W_0), -h_g < z' < h'(x', -(W' - W_0))) \\ & \text{and,} \quad (y' = W_0, -h_g < z' < h'(x', W_0)) \end{aligned} \tag{2.8}$$

$$\partial_{z'}\phi' = 0 \qquad \text{in} \qquad z' = -h_g \tag{2.9}$$

$$\partial_{z'}\phi' = \partial_{x'}h'\partial_{x'}\phi' + \partial_{y'}h'\partial_{y'}\phi', \quad \text{and,} \quad p' = 0 \quad \text{in} \quad z' = h'(x', y')), \tag{2.10}$$

where equation (2.10) is usually called the kinematic condition. The hydrodynamic pressure, maintaining the potential formulation, is described by the non-linear Bernoulli equation:

$$\frac{1}{\rho}p' + \frac{1}{2}(\nabla\phi')^2 + gz' = \frac{1}{2}U_0^2 + g\Delta h \tag{2.11}$$

Applying equation (2.11) to the free surface we obtain the, so called, dynamic boundary condition, which assumes that the free surface is a stream line and reads,

$$\frac{1}{2}(\nabla\phi')^2 + gh'(x', y') = \frac{1}{2}U_0^2 + g\Delta h. \tag{2.12}$$

In equation 2.12 we have considered that, far upstream, as $x' \to -\infty$, $h' \to \Delta h$, ϕ_y, $\phi'_z \to 0$ and $\phi'_x \to U_0$, where U_0 is assumed to be the constant component of the uniform velocity profile, at that location, where $F'(x', y') = h_0$.

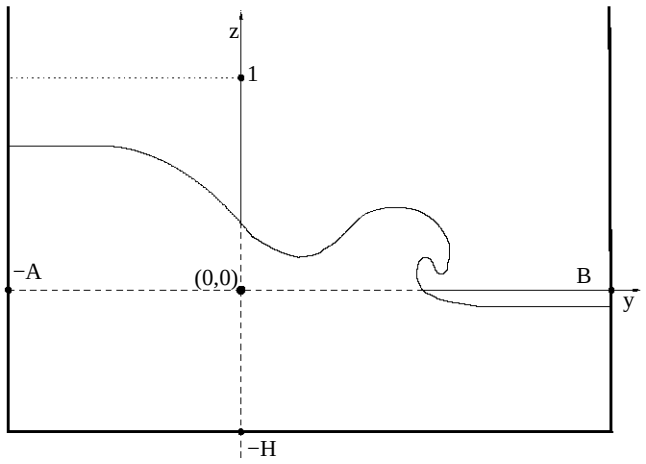

Figure 2.2: Cross View of the dimension-less flow domain $\Omega(t)$ of a corner wave for $x > 0$.

2.2.1 Dimensionless form of the equations

The system of equations (2.7)-(2.12) can be written in non-dimensional form by introducing the following variables:

$$x = x'/\Delta h,\ y = y'/\Delta h,\ z = z'/\Delta h,\ h = h'/\Delta h,\ \phi = \phi'/(U_1 \Delta h) \text{ and } p = p'/\rho U_1^2,$$

and therefore, the limits of the flow domain $\Omega(t)$ turn into: $A = (W' - W_0)/\Delta h$, $B = W_0/\Delta h$ and $H = h_g/\Delta h$, as sketched in figure 2.2.

In consequence, the system (2.7)-(2.12) assumes the following form:

$$\nabla^2 \phi = \phi_{xx} + \phi_{yy} + \phi_{zz} = 0 \qquad \text{in} \qquad (x > 0, -A < y < B, -H < z < h(x,y)) \tag{2.13}$$

with the boundary conditions at the walls:

$$\partial_y \phi = 0 \quad \text{in} \quad (y = -A, -H < z < h(x,y)) \cup (y = B, -H < z < h(x,y)) \tag{2.14}$$

$$\partial_z \phi = 0 \quad \text{in} \quad z = -H \tag{2.15}$$

At the free surface, the kinematic boundary condition becomes,

$$\partial_z \phi = \partial_x h \partial_x \phi + \partial_y h \partial_y \phi, \tag{2.16}$$

whereas the dynamic boundary condition,

$$(\nabla \phi)^2 - 1 = 2Fr^{-2}(1 - h(x,y)). \tag{2.17}$$

Notice that, using non-dimensional variables the flow assesses, far upstream, $h \to 1$, $\phi_x \to \sqrt{U_1^2 - 2g\Delta h}$ and $\phi_y = \phi_z = 0$.

2.3 2D+T approach

It can be observed that when we approach the limit $Fr \gg 1$, equation (2.17) can be approximated as:

$$(\nabla\phi)^2 = 1, \tag{2.18}$$

which has a trivial solution, $\phi = x$. The aforementioned solution can be expanded in terms of a higher approximation,

$$\phi = x + \Phi(x, y, z, Fr) \qquad \text{with} \qquad \Phi \to 0 \qquad \text{as} \qquad Fr \to \infty \tag{2.19}$$

Substituting the expression (2.19) into equation (2.17), and using $|\nabla(x+\Phi)|^2 = |(\vec{e_x} + \nabla\Phi)|^2 = (\vec{e_x}+\nabla\Phi).(\vec{e_x}+\nabla\Phi) = 1+2\partial_x\Phi+|\nabla\Phi|^2$, the dynamic condition and, proceeding likewise in equation (2.16), the kinematic boundary condition, can be written as:

$$\begin{aligned} &\partial_x\Phi + \frac{1}{2}|\nabla\Phi|^2 = Fr^{-2}\cdot(1-h) \\ &\partial_z\Phi = \partial_x h + \partial_x\Phi\partial_x h + \partial_y\Phi\partial_y h \end{aligned} \tag{2.20}$$

Expressions (2.20) indicate that, at distances $x \sim O(\Delta h)$ and approaching the limit $Fr \to \infty$, the dominant term in the dynamic condition is $Fr^2\partial_x\Phi$, and therefore,

$$\Phi = O(Fr^{-2}) \qquad \text{and} \qquad \partial_x h = O(Fr^{-2}), \tag{2.21}$$

Consequently, at the leading order, the boundary conditions, (2.20), assume the form of:

$$\partial_x\Phi^{(0)} = Fr^{-2}(1-h) \qquad \text{and} \qquad \partial_x h^{(0)} = \partial_z\Phi^{(0)}. \tag{2.22}$$

This pair of boundary conditions, (2.22), should be imposed on the the free surface $z - h(x, y) = 0$. It is worth noticing that, as $x \to \infty$, the dynamic boundary condition of equation (2.22) results in $\Phi^{(0)} \simeq Fr^{-2}x$. And assuming that the kinematic one, $\partial_z\phi^{(0)}$ behaves similarly, it can be written that, at the leading order:

$$h^{(0)} \sim x^2 Fr^{-2} \tag{2.23}$$

All the above suggest, that small-distance solution grows as $x \to \infty$ and the assumption $\Phi = O(Fr^{-2})$ is not valid at distances $x \sim Fr$.

The hypothesis $Fr \gg 1$, will be tested in following chapters and it will be demonstrated that all the conclusions remain valid not only for large values of the Froude number but also, for moderate ones, provided the supercritical character of the flow $Fr > 1$.

2.3.1 2D+T approximation

In section 1.1.3, the benefits of applying the 2D+T approximation to convert an steady 3D case to an unsteady 2D one were highlighted. Now, once the non-dimensional variables are defined and the new scales for x and ϕ proposed, the transformation can be accomplished through a simple rescaling of the streamwise coordinate and the velocity potential,

$$x = Fr \cdot t \qquad \Phi = Fr^{-1} \cdot \phi(y, z, t, Fr). \tag{2.24}$$

Subsequently, introducing the rescaling variables into (2.20), the boundary conditions become:

$$\partial_t \phi + \frac{1}{2}|(\partial_y \phi)^2 + (\partial_z \phi)^2| = (1 - h) - \frac{1}{2} Fr^{-2} \cdot (\partial_t \phi)^2 \tag{2.25}$$
$$\partial_t h + \partial_y \phi \partial_y h = \partial_z \phi - Fr^{-2} \partial_x \phi \partial_x h$$

Assuming now, as mentioned above, that the Froude number is large enough, $Fr \gg 1$, the flow field can be described rewriting the system (2.13)-(2.17), without the the streamwise coordinate, becoming an unsteady bi-dimensional problem, $\phi = \phi(y, z, t)$,

$$\nabla^2 \phi = 0 \qquad (t > 0, (y, z) \ni \Omega(t)) \tag{2.26}$$

$$\partial_t \phi + \frac{1}{2}|(\partial_y \phi)^2 + (\partial_z \phi)^2| = (1 - h) \tag{2.27}$$
$$\partial_t h + \partial_y \phi \partial_y h = \partial_z \phi$$

in which, the boundary conditions (2.27) must be imposed in the free surface ($t > 0, -H < z < h(y, t)$). The boundary conditions at the channel walls and the bottom of the channel read now $\partial_y \phi = 0$ in $(y = -A, y = B)$ and $\partial_z \phi = 0$ in $(z = -H)$.

The system of equations (2.26)-(2.27), can be considered, at sufficient large distances from the plate, as 2D and non-linear. Note that, in the leading order, the far field flow corresponds to a 2D gravity-driven flow and the referred equations can be solved by using a Boundary Element Method.

In order to facilitate the calculations, the potential will be redefined as $\phi = \bar{\phi} + t$, becoming,

$$\nabla^2 \bar{\phi} = 0 \qquad (t > 0, (y, z) \ni \Omega(t)) \tag{2.28}$$
$$\partial_t \bar{\phi} + \frac{1}{2}|\nabla \bar{\phi}|^2 + h = 0$$
$$\partial_t h + \partial_y \bar{\phi} \partial_y h - \partial_z \bar{\phi} = 0$$

System (2.28) will be used along the rest of this work to describe the corner wave flow and, for simplicity, the notation for the potential $\bar{\phi}$ will be replaced by ϕ.

2.4 Concluding Remarks

In this chapter, a mathematically formulation for the corner wave flow has been presented. The non dimensional parameters involved in the formulation have been proposed and all the variables rescaled assuming large Froude numbers. Finally, the transformation from the original 3D steady Euler equations to a 2D+T system has been carried out. This formulation will be numerically validated, and compared with experimental results in Chapter 4.

2.5 Acknowledgements

We would like to thanks Prof. Alexander Korobkin for his useful comments and his kindly advice and aid in this chapter.

CHAPTER
THREE

Experimental Work

3.1 Introduction

An experimental study of the flow downstream from the corner of a partially submerged vertical plate, placed in a recirculating water channel wider than the plate, is presented in this chapter. The particularity of this flow, compared with the classic flow configurations around objects, consists in the formation of a three dimensional steady wave, hereafter named *corner wave*. This wave originates at the corner of the plate and develops in the downstream direction in a similar way as a two dimensional wave evolves in time. Likewise the two-dimensional case, the crest advances along the spanwise direction while the wave amplitude grows, eventually leading to the formation of either a plunging or a spilling breaker, depending on the flow parameters. A remarkable characteristic of this wave is that its evolution and breaking is largely unaffected by the presence of the channel side and bottom walls, even when their distance to the wave is comparable to the wave amplitude. These observations, together with the formulation presented in Chapter 2, complement the possibility of broadening the applicability of this simple laboratory flow to the study of the evolution and breaking of two-dimensional deep-water waves.

3.2 Experimental set-up

The experiments were carried out in two recirculating water channels, one at the Department of Mechanical and Aerospace Engineering of University of California San Diego (UCSD) and the other at the Fluid Mechanics Group at Universidad Carlos III, Madrid (UC3M). Both channels are similar in design, although they differ in the dimensions of the test section. The UC3M channel, built one third scale of the UCSD one, was used only for flow visualizations. In particular, the experiments shown below refer only to the UCSD one.

The UCSD channel had a capacity of about five cubic meters. The test section was 2 m long with a [0.6 m $\times$ 0.6 m] square cross section. The plenum was connected to the test section by a series of grids and honeycombs, followed by a contraction, to ensure that the fluctuations originated at the pump were damped out before the flow reached the test section. A sketch of the facility can be found in Rodríguez-Rodríguez *et al.* (2011).

	W	h_g (mm)	h_1 (mm)	h_0 (mm)	Δh (mm)	δ (mm)	U_1 (m/s)	Fr_{h_g}	$Fr_{\Delta h}$
A	0.5	155	105	310	205	50	2.09	2.87	2.17
B	0.5	155	105	252	147	50	1.84	2.23	2.35
1	0.5	95	58	374	316	37	2.48	6.60	1.99
2	0.5	95	58	352	294	37	2.41	6.23	2.01
3	0.5	95	58	239	181	37	1.94	4.04	2.11
4	0.5	95	58	127	69	37	1.31	1.84	2.53
5	0.5	162	108	306	198	54	1.95	2.40	1.96
6	0.7	140	93	257	164	47	1.71	2.13	1.81
7	0.3	118	77	230	153	41	1.75	2.64	2.04

Table 3.1: Summary of some representative experimental conditions, where W is the non-dimensional width of the plate, h_0 the water level upstream the plate, h_1 the water level downstream the plate and h_g the height of the lower edge of the plate with respect to the basin. The experimental error in the determination of all the heights involved in this work was estimated to be ± 2 mm.

Three Plexiglas plates of different widths (0.3, 0.5 and 0.7 times the channel width (0.6 m) $\times$ 0.0127 m $\times$ 1 m) were manufactured, placed vertically across the test section, and fixed to one of the walls of the water channel to produce the corner wave. To place the plate inside the test section, and fix the value of h_g, a vertical traverse was used.

The dependence of the breaker configuration (spilling or plunging) on the flow speed, U_1, and on the characteristic length scales, $\Delta h = (h_0 - h_1)$ and $\delta = (h_g - h_1)$, was investigated through a parametric study. To that end, several velocity profiles were measured, in the region of constant height h_1, using a Pitot tube for every flow configuration reported in this work. It was found that the experimental value of the velocity does not separate more than a 15% from the theoretical one, stated in equation (2.3). In addition, all the heights involved in this study, as well as other geometrical features of the corner wave discussed below, were obtained using digital image processing. Moreover, the velocity profile upstream the plate was also measured, in some canonical cases, to ensure its uniformity, as stated by Roth & Hager (1999).

Table 3.1 contains a summary of the experimental conditions obtained in this work. In each run, one among three different plates of width 30%, 50% and 70% of the channel width, W', were used. Correspondingly, the value of the plate width is expressed as $W = 0.3$, $W = 0.5$ and $W = 0.7$, with $W = W_0/W'$. Table 3.1 also shows the relevant parameters of the flow h_0, h_g and h_1, sketched in Fig. 2.1, the Froude number, based on

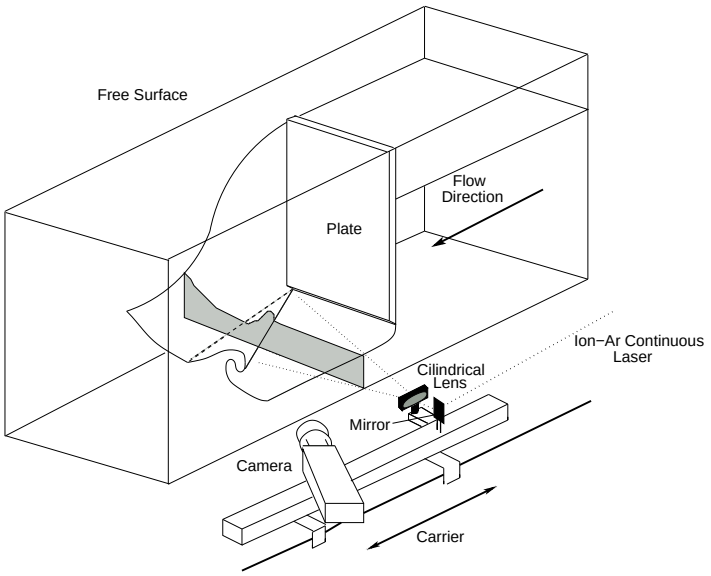

Figure 3.1: Sketch of the Laser Induced Fluorescence (LIF) set-up. The laser sheet, parallel to the plate, passes through the free surface of the flow which is captured by a CCD camera attached to the traverse.

Δh defined as $Fr_{\Delta h} = U_1^2/g\Delta h$, and the Froude number based on the height from the bottom of the channel to the lower edge of the plate, h_g defined as $Fr_{h_g} = U_1^2/gh_g$.

3.2.1 Laser Induced Fluorescence (LIF)

A series of Laser Induced Fluorescence (LIF) measurements were performed in the UCSD channel to characterize the elevation of the free surface. To that end, as sketched in figure 3.1, a 7W Ion-Argon laser beam (Coherent Innova 90) operating in all lines mode, was mounted on an optical table near the channel. The beam was aligned parallel to the lateral walls of the test section using a set of mirrors. One additional mirror, mounted in a traverse parallel to the wall, was used to direct the beam perpendicular to the test section and lined up with the plate. A combination of cylindrical and spherical lens were used to produce a laser sheet in the plate's plane ($y' - z'$). In addition, the water ($\sim 6\text{m}^3$) was seeded with around 50 grams of fluorescein ($\sim$ 10 ppm), in order to facilitate the visualization of the flow.
The intersection of the flow with the laser sheet was captured using a digital (CCD) camera (Kodak Megaplus 1.0 ES) with a resolution of 1008 $\times$ 1010 pixels, together with a NIKON lens of 30 mm of focal distance and 1.4f. A band-pass filter was placed in front of the lens to avoid any reflections that could have damaged the camera sensor. The viewing direction of the camera was set at an angle of 45 degrees to the normal of the laser sheet to ensure optimal spatial resolution.

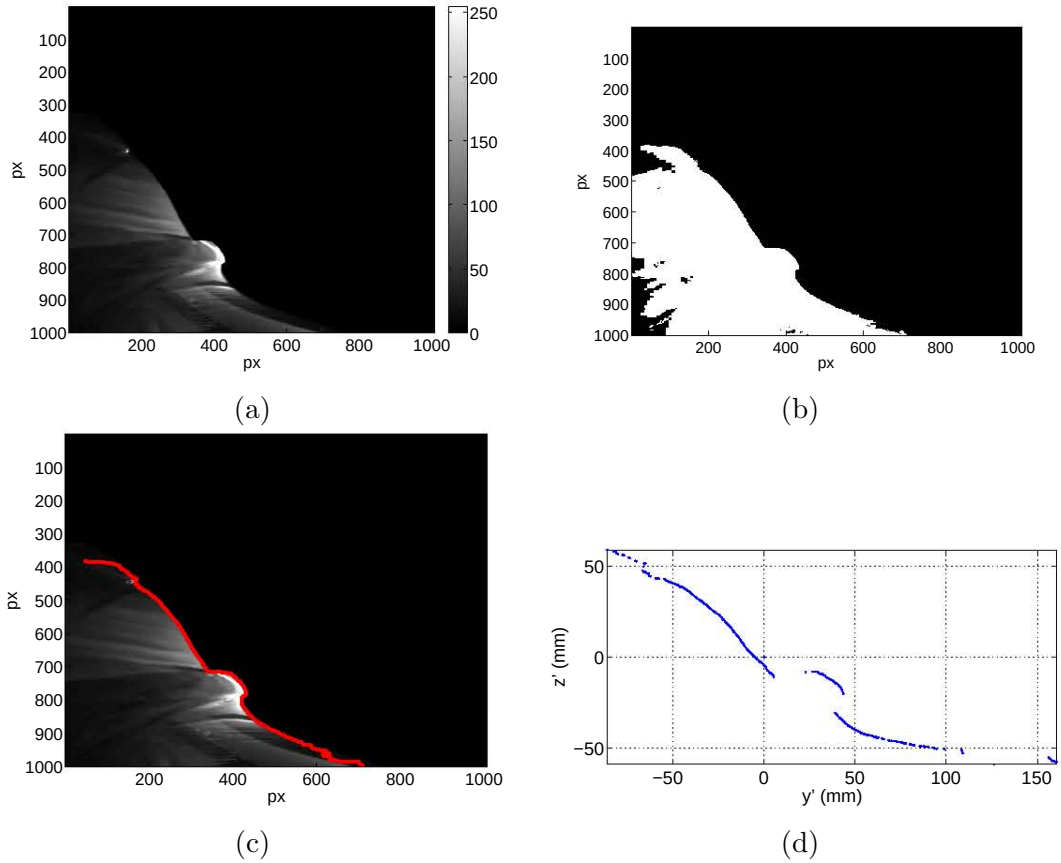

Figure 3.2: Image processing routine used to extract the free surface location in the LIF experiments. (a) Raw cross-view image of a plunging breaker in which the lateral bar represents the gray intensity in each pixel. (b) Results of applying a binary threshold to figure (a). (c) Free surface location after using an edge-detection algorithm. (d) Free surface location in the original axis. Notice that, by illuminating the flow from the side of the channel, the parts of the free surface with negatives or horizontal slopes can not be precisely determined and should be removed from the results.

Calibration images were acquired using a grid attached to the downstream face of the plate, as shown in figure 3.3(d). The laser sheet and the camera, placed on the same traverse, were moved together in the streamwise direction, thus ensuring that the camera was always focused on the light sheet in a region that covered the corner wave.

The field of view of the camera was about 0.4 m, corresponding to a resolution of approximately 2.5 px/mm. In the proximity of the plate, where the wave is starting to develop and the free surface shape is smooth, its location could be determined with an accuracy of ± 3 mm, taking into account all possible experimental errors. However, in

regions where the free surface shape was more complex, as the region near the splash of plunging breakers, the accuracy of the method was estimated to be ±6 mm.

Once the images were acquired, the location of the free surface was determined by an image image processing routine written in MATLAB.
Figure 3.2 shows the different steps of such process. In figure 3.2(a), a raw acquired image is shown together with the gray intensity levels of each pixel. Notice that, when illuminating the flow, the addition of fluorescein allows the visualization only of the section bisected by the laser beam and its downstream development. Hence, as shown in figure 3.2(b), a threshold can be applied to the image to convert the regions with less gray intensities to a single one with an assigned value of gray intensity and the process can be similarly applied to the other areas of the image. Therefore, the gray intensity gradient can be used as a marker to determine the position of the free surface, as shown in figure 3.2(c). It is important to notice that, by illuminating from one side of the channel, there exists regions of the free surface which, depending on its curvature, can create shadows in the image. The existence of shadows in the image leads to errors in the determination of the interface. In this study all the regions of the free surface in which negative or zero vertical slopes were observed, are declared invalid and removed from the final result to minimize the above mentioned effect.

The previously exposed LIF technique was applied to the two typical breaker configurations, namely plunging and spilling, denoted in table 3.1 as cases A and B. Figure 3.3 shows the free surface reconstruction of both breakers, together with an image of the calibration grid.

Specifically, figure 3.3 (a), shows the free surface evolution of the case A of table 3.1. This case corresponds to a typical plunging breaker. Notice that, as mentioned above, the curl of the crest produces shadow regions that limits the ability of the technique to characterize the totality of the free surface location in this configuration. To illustrate this effect, a red line representing the shape of a plunging breaker is added to the mentioned figure. Figure 3.3 (b), shows the free surface evolution of the case B of table 3.1. In this figure, it can be appreciated that the wave becomes steeper as it evolves, until the crest becomes unstable, resulting in whitewater spilling down the face of the wave, as described by Duncan *et al.* (1999). Figure 3.3 (c), shows the numerical evolution of the free surface, of case A of table 3.1, by using the 2D+T approximation described in Chapter 2. To facilitate the comparison with (c), in (a) and (b), all magnitudes are plotted in the 2D+T dimensionless form by using $x = x'/\Delta h \cdot Fr_{\Delta h}$, $y = y'/\Delta h$ and $z = z'/\Delta h$ (see again Chapter 2).

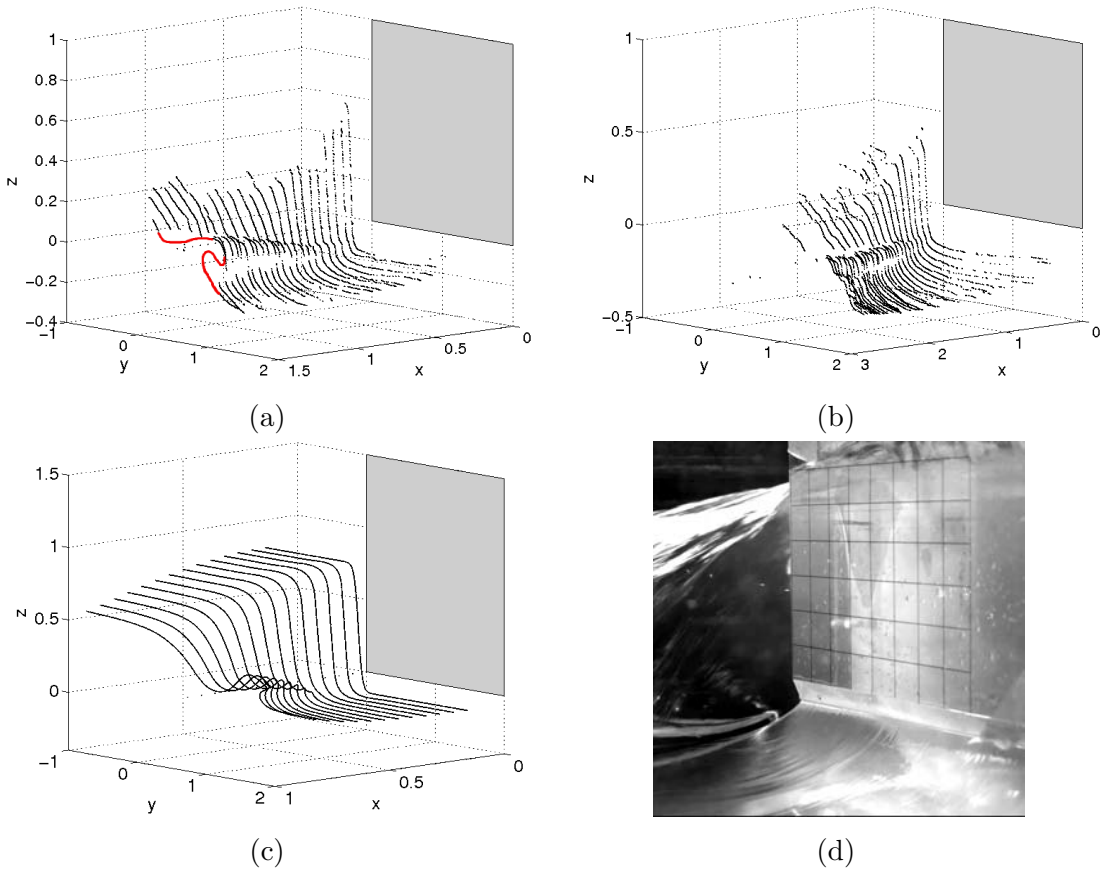

Figure 3.3: LIF Results of the different breaking conditions: (a) plunging breaker. (b) spilling breaker. The plunging breaker corresponds to case A in table 3.1 and the spilling one to case B. A line marking the corner of the plate is plotted together as a reference in both figures. To clarify the plunging configuration a sketch of the real free surface, plotted in red color, is added in (a), showing the limitations of the method. (c) Numerical result of the plunging breaker (a), using a 2D+T approximation code, as described in Chapter 2. (d) LIF calibration grid.

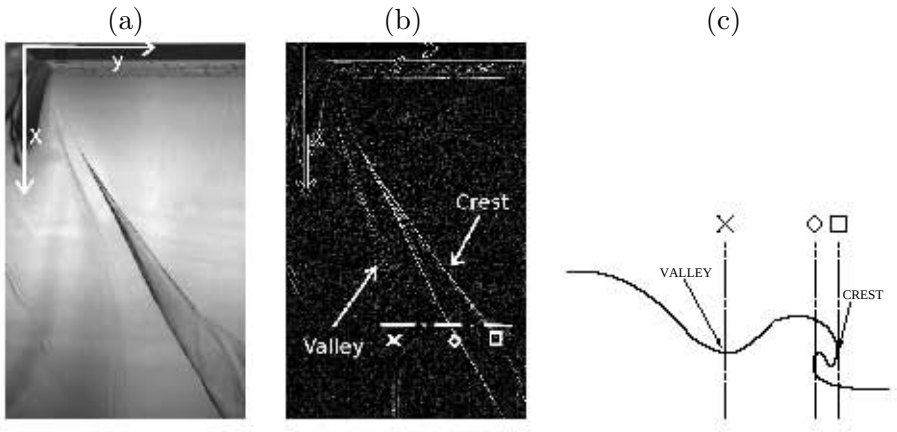

Figure 3.4: Image processing method used to obtain the trajectories of a corner wave. (a) Top view of a typical plunging breaker. Notice that the shaded region of the wave coincides with the overturning of the crest. (b) Edge detection algorithm with the crest (leading edge) and valley (trailing edge) identification. (c) Sketch of the cross-section view identified in (b) as the dash-dotted line.

3.3 Results and discussion

3.3.1 Influence of the channel walls

In this section the influence of both, the finite depth of the water stream, and the presence of the channel walls, is explored. It will be shown that, under the experimental conditions considered, the development of the corner wave is only slightly affected by these boundaries. This is a remarkable conclusion, as the distance of the corner of the plate to one of the walls and to the bottom, is of the order of the amplitude of the wave.

To quantify the possible effects of the finite depth and the walls, high-resolution images of corner waves, corresponding to cases 1-7 of table 3.1, were acquired from above with the aim of detecting the trajectory of the leading and trailing edges. The leading edge is identified by the line in which the maximum curl in the free surface is attained, whereas the trailing edge is determined by the depression, or valley, which is left backwards the wave in its development. An example of these images is shown in figure 3.4(a), whereas figure 3.4(b) illustrates the detection of both edges using image processing tools. The error in the identification of the location of the crest was estimated to be of the order of the height of the capillary ripples as ± 5 mm. However, for the valley, the error increases up to ± 10 mm, due to the the absence of a steep free surface shape in that location, which produces large light reflections and therefore, large light intensity gradients in the acquired image, facilitating the post-processing.

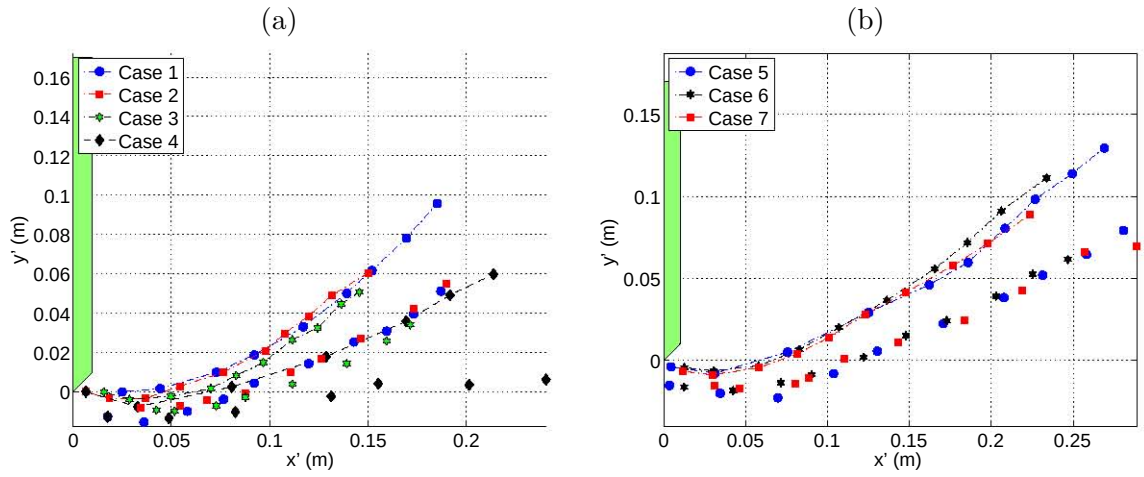

Figure 3.5: Wave crest and valley trajectories. (a) Wave trajectories of cases 1-4 of table 3.1. (b) Wave trajectories of cases 5-7 of table 3.1, obtained using three different plates of $W = 0.3$, 0.5 and 0.7 for the same $Fr_{\Delta h}$. In both figures, the dash-dotted line represents the leading edge trajectory.

The dimensional parameter that controls the depth of penetration of the plate is the height of its lower edge, h_g. In dimensionless terms, this parameter yields a Froude number, $\mathrm{Fr}_{h_g} = U_1^2/gh_g$. The influence of this parameter in the wave trajectories, compared to the previously defined Froude number, based in the maximum difference of heights of the free surface, $\mathrm{Fr}_{\Delta h} = U_1^2/g\Delta h$, can be seen in figure 3.5(a), where the trajectories of four different waves, identified as cases 1-4 in table 3.1, are plotted. The first three trajectories were obtained keeping the Froude number $\mathrm{Fr}_{\Delta h}$ almost constant, while varying h_g and thus Fr_{h_g}. Figure 3.5(a) reveals that moderate variations of the Froude number based on the distance h_g do not produce significant changes in the trajectory of the wave. However, variations of similar magnitude in the Froude number $\mathrm{Fr}_{\Delta h}$ (as can be seen in the fourth trajectory of the figure) significantly changes the trajectory. In particular, this result reveals that the corner wave is not affected by the presence of the bottom in the range of parameters we consider.

Regarding the influence of the lateral channel walls, similar experiments were performed keeping $\mathrm{Fr}_{\Delta h}$ constant, but changing the plate width. Figure 3.5(b) shows the wave trajectories, close to the plate, for three experiments with different plate widths ($W = 0.3$, 0.5 and 0.7) and similar $Fr_{\Delta h}$. It can be seen that the influence of the width of the plate on the emergence angles of the crest of the wave is negligible.

With the above results in mind, it can be concluded that, for all the experiments reported herein, the wave trajectories are solely a function of the Froude number, $Fr_{\Delta h}$.

Type of breaker.	h_g (mm)	h_1 (mm)	h_0 (mm)	Δh (mm)	U_1 (m/s)	$Fr_{\Delta h}$	Fr_g
Plunging	95-191	32 - 134	203-363	130-270	1.6-2.1	1.5-2.3	5.4-12.4
Spilling	95-191	67-142	120-265	47-135	1.3-1.7	1.8-2.5	4.2-7.1

Table 3.2: Ranges of the relevant parameters of the flow used to investigate the ballistic path of the crest of the corner wave and its breaking process.

However, it is important to point out that this analysis is expected to remain valid only as long as the corner wave trajectories do not interact with the boundary layers at the walls, whose effects are not explored in this work.

These results confirm that the corner wave is a local phenomenon which is mainly driven by the conditions near the corner of the plate, being not overly affected by the solid boundaries of the channel.

3.3.2 Ballistic Trajectories and Plunging-Spilling transition

It is well known that, in the dimensional deep water plunging breakers, the sheet ejected after the separation of the crest, hereafter referred to as jet, follows a ballistic trajectory in its evolution. Previous works, and in particular Longuet-Higgins (1995), describe theoretically that "when the tangent of the free surface of the wave near the crest makes a sharp right-angle turn, there is a large pressure gradient in the fluid that accelerates the fluid near the crest horizontally and propels a jet forward from the crest. From about, the jet narrows rapidly, and the pressure within the jet diminishes drastically; the fluid is then almost in a state of a free-fall in a parabolic trajectory". This assertion has been verified experimentally, among others, by Shakeri *et al.* (2009*b*) or Drazen *et al.* (2008). The goal of this section is to check that this 3D steady flow configuration can be used to study such phenomenon.

Assuming, for the sake of the argument, that the crest of the corner wave behaves similarly to that of a deep water wave, it would be natural to define the range of its ballistic path, x_r, as the distance between the separation point, that occurs in the vicinity of the corner of the plate, and the point where the jet impacts on the free surface downstream from the plate, in the downstream direction. This assumption is motivated by the observation of figures 2.1(c), 2.1(d) and 3.4(a), where, in the top view, the crest of the corner

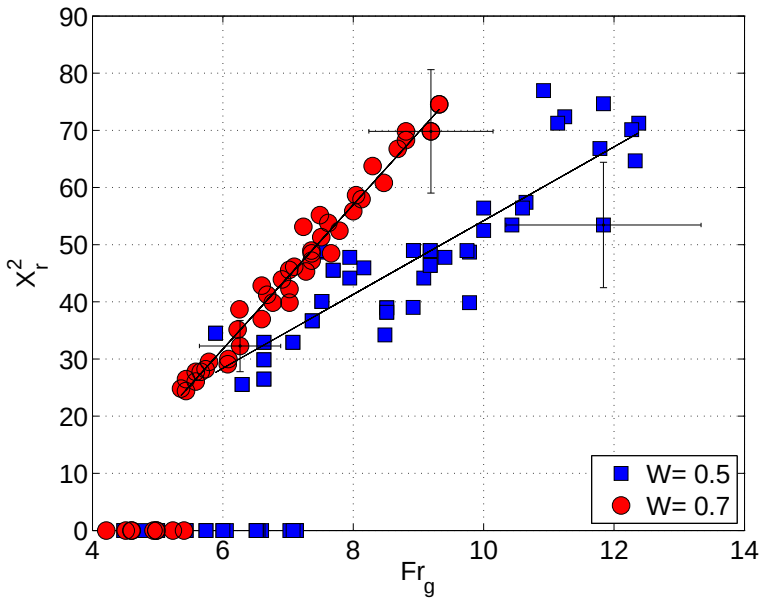

Figure 3.6: Square dimensionless range as a function of the modified Froude number, Fr_g. The blue squares represent $W = 0.5$ and the red circles $W = 0.7$. The linear relation between X_r and Fr_g, for each plate, validates the ballistic trajectory assumption.

wave is seen to follow a straight line starting almost at the plate. It should be emphasized that, contrarily to the wave trajectory, the range of the ballistic trajectory in the (y'-z') plane will be shown to be more sensitive to δ than to Δh.

Following the ballistic flight theory, the range x_r should scale with the time of flight of a particle falling a distance equal to the height of the plate edge with respect to the free surface, $\delta = (h_g - h_1)$, i.e. $t_f = (\delta/g)^{1/2}$. Thus,

$$x_r \sim U_1 \, t_f = U_1 \, (\delta/g)^{1/2} \tag{3.1}$$

Equation (3.1) suggests that the square of the dimensionless range of the ballistic path, $X_r^2 = (x_r/\delta)^2$, must follow a linear relation with a modified Froude number defined as, $Fr_g = Fr_{\Delta h}\Delta h^* = U_1^2/g(h_g - h_1)$, where $\Delta h^* = \frac{\Delta h}{\delta} = \frac{h_0 - h_1}{h_g - h_1}$ is the initial potential energy of the jet, made dimensionless with the height of the plate h_g, relative to the free surface depth h_1. Therefore, $X_r^2 \sim Fr_g$.

In figure 3.6, the experimental values of the squared dimensionless range are plotted against the Froude number, Fr_g, for a wide range of variation of the characteristic length scales, shown in table 3.2, including also, variations in the plate/channel width ratio, W. The detection of the range x_r is done by experimentally determining, from the acquired images, the location of the splash point. The error bars in figure 3.6 take into account the

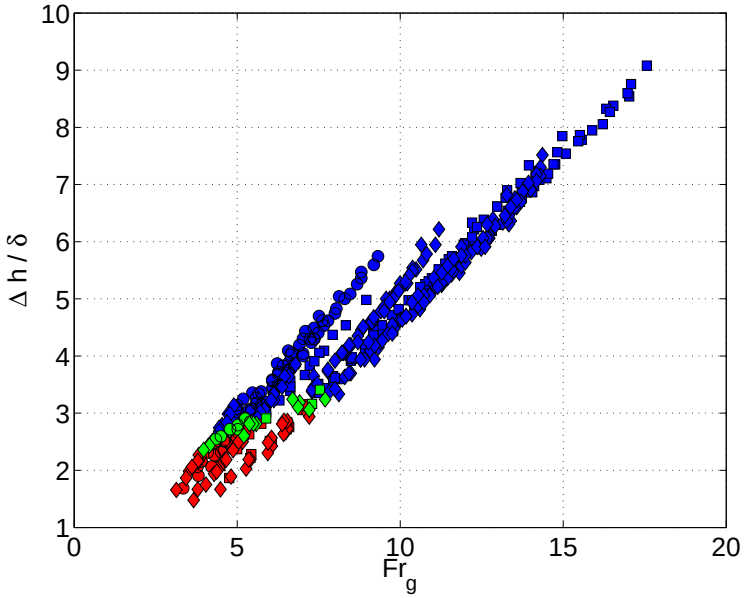

Figure 3.7: Ratio of the potential energy of the corner wave as a function of the modified Froude number, Fr_g. The squares represent $W = 0.5$, the circles $W = 0.7$ and the diamonds $W = 0.3$. In addition, the blue color denoted plunging waves cases whereas the red one represents spilling ones. The green color was used when it cannot be determined if the wave was either plunging or spilling.

oscillations observed in the splash point as well as the error in the velocity determination. For the cases that correspond to spilling waves a null value was assigned to the range ($x_r = 0$), since there is not jet. Notice that, for each plate, the data are well fitted by a straight line for each width of the plate W, which validates the ballistic flight hypothesis.

A remarkable conclusion that can be drawn from this experimental study is that, whereas the trajectory of the wave does not seem to be significantly affected by the height of the plate with respect to the bottom, the range of the ballistic flight of the jet is strongly dependent on this parameter. The explanation for the former conclusion is that the formation of the wave is determined by the local structure of the flow near the corner, that is fairly similar to that of a plate immersed into a uniform stream of velocity U. In that ideal case, the available water height above the corner, Δh, emerges as the only parameter, together with U, affecting the flow. In other words, the velocity field near the corner would vary along distances of the order of the flow depth, that are much larger than the size of the wave at the location where the jet detaches. From that point on, changes in the flow field due to the presence of the bottom will not affect the jet trajectory, that is solely determined by the "launch" conditions.

Differently, the range of the ballistic flight of the jet must depend on the height that the jet will fall from its origin. Obviously, this free-fall height is determined by the *vena contracta* effect, that leads to the lowering of the free surface far downstream with respect to the height of the corner, where the jet nearly originates. It is well known (Montes (1997), Chow (1959)), that the water depth far downstream, h_1, is proportional to the height of the plate with respect to the bottom, h_g, thus the free-fall height, $h_g - h_1$, can be considered to be also proportional to h_g.

Figure 3.7 shows that the transition between the different breaking regimes nearly occurs when the ratio between the available water height above the corner, Δh, and the contraction of the free surface due to the *vena contracta* effect, δ, adopts a value of about $\Delta h/\delta \approx 3$. Although the exact value has been seen to depend slightly on the Froude number based on δ, Fr_g, this criterion is independently of the plate width, W. More specifically, when the height ratio $\Delta h/\delta$ exceeds the critical value, a plunging breaker is observed.

The difference between the slopes observed in figure 3.6, is likely due to the absence of experiments with similar Froude numbers, $Fr_{\Delta h}$, in the experiments with different plate width W, as shown in figure 3.8. In the mentioned figure, it can be seen that due to the experimental limitations of our facility, we can not achieve waves with similar $Fr_{\Delta h}$ and different W. To clarify this point further experiments should be performed, recommending for such purpose, the use of a calm water towing tank, in which the effect of the boundaries can always be neglected, instead of a recirculation channel.

3.4 Concluding Remarks

In this chapter we have presented an experimental study of several aspects associated to the corner wave. In particular, it has been demonstrated that the corner wave trajectories do not depend on the location of the walls and bottom, being a local phenomenon affected only by the Froude number $Fr_{\Delta h}$. A criterion for the transition between overturning corner waves and spilling ones has been proposed, based on the geometrical parameter $\Delta h/\delta \simeq 3$. Moreover, it has been proven that the crest of the corner wave follows a ballistic path when separating from the body of the wave, as occurs in deep water waves. Further experiments, in a calm water towing tank, must be carried out in order to clarify the existence of a, Froude dependent, breaking criterion.
The fact that the bounding walls of the channel, in the reported experiments, do not affect the corner wave trajectory, allow us to establish a relationship between the corner wave flow with deep water waves, and with the corner waves that appear in the wake of high

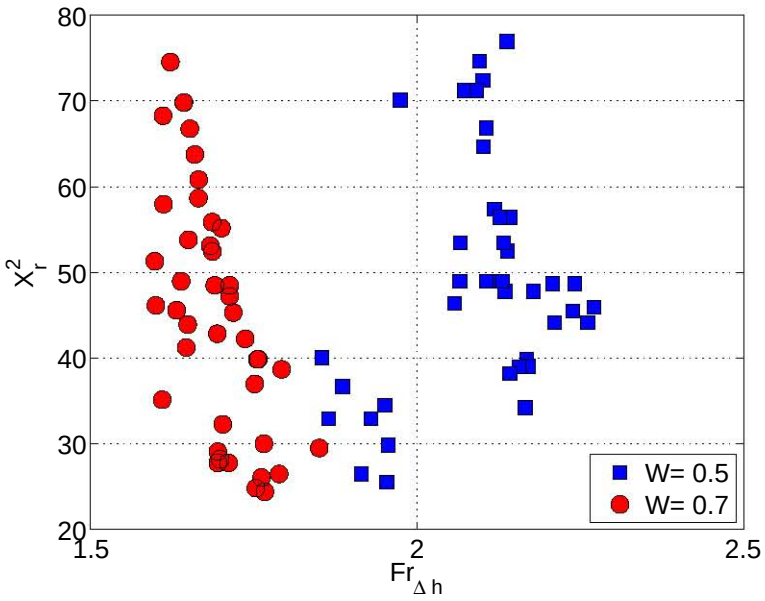

Figure 3.8: Square dimensionless range as a function of the Froude number, $Fr_{\Delta h}$. The blue squares represent $W = 0.5$ and the red circles $W = 0.7$. Notice that there exists a region in which .

speed vessels for sufficiently large Froude numbers.

CHAPTER
FOUR

Numerical Strategy

4.1 Introduction

The interface between a gas and a liquid, *the free surface*, takes its name from the large difference in densities between the gas and liquid phases. This large density ratio, generally leads to negligible inertia associated with the gas, which allows the liquid to move independently , "freely", of the gas. Therefore, the presence of a free surface involves the existence of moving boundaries that difficult the solution and treatment of the problems, becoming necessary to resort to numerical solutions.

Independently of the method employed to solve problems with free surface, there are three basic steps that should be taken into account:

- Define a proper numerical scheme that returns the free surface shape and location.
- Determine how the free surface will evolve in time.
- Apply and update the kinematic and dynamic conditions to the free surface in each time step.

Following the above mentioned steps, the computation of flows with free surface has experienced a complete renovation over the last twenty years. In the lately years of computational fluid dynamics (CFD), the treatment of free surface problems has led to two different approaches, Lagrangian and Eulerian. An overall inspection of the treatment of this kind of problems can be found in the reviews written by Yeung (1982) and Tsai & Yue (1996).

In the Lagrangian approaches, also called interface-tracking methods, only the liquid phase is computed. These methods use a grid that varies over time and space, adapting its boundary to the shape and position of the free surface. In the interface-tracking methods, the free surface is part of the boundaries of the computational domain and is subject to the usual kinematic and dynamic boundary conditions.

The main advantage of the Lagrangian method is that the interface is delineated accurately and its shape is precisely captured. This fact makes the Lagrangian methods very adequate for viscous or laminar flows.

On the other hand, the continuous tracking of the free surface entails problems of mesh distortion, that commonly result in instabilities and lack of internal physics. Sudden variations in the interface shape, as those encountered in overturning or breaking waves, also generate problems in the accuracy of Lagrangian methods. An early approximation to the Lagrangian approach to free surface problems can be found in Hirt *et al.* (1970) and Nichols & Hirt (1974).

The Eulerian approach based methods, also called interface-capturing methods, consider both phases as an effective fluid, with variable properties. Subsequently, the free surface is determined by sudden changes, or peaks in the gradient of those properties. This approximation avoids the inconvenient determination of the exact free surface location in each time step, but requires the resolution of an additional transport equation to follow the variations of an specific property, i.e. the volume fraction.

The Eulerian approach forces the fluid to travel between the cells of a fixed mesh, avoiding the problem of mesh distortion found in the Lagrangian approach. In the last twenty years, the advances in the adaptive mesh techniques have increased up to the limit, the resolution of the Eulerian methods.

The main advantage of this approach is that it can be applied to flows with an arbitrary deformation of the interface, and also works accurately in the case of drops or bubbles taking into account buoyancy and surface-tension effects. The possibility of capturing complicated free surface shapes makes this approach ideal to use in the corner wave problem. In fact, when looking at the literature, it can be seen that the interface-capturing methods are widely used in breaking waves simulations, see i.e. Helluy & Golay (2005).

The Eulerian approach is the basis of several methods. In particular, the more used are the following:

Surface Height Method

The surface height method is commonly applied when the free surface does not have significant deviations from its initial shape. This method is based on the assumption that the free surface location can be always determined using its distance to the basin, H, which is not multi-valued. Obviously, this definition becomes a problem in case of overturning

waves, limiting the capabilities of this method. However, such approximation allows the simplification of the Navier-Stoke equations, as i.e. by using the shallow-water equations, which provide fast calculations, with good resolution, in some problems as i.e in low amplitude sloshing tanks or in certain problems associated with shallow water waves.

This method uses the conservative form of the equations, which can be solved using finite difference schemes. The basis of the surface height methods were stated by Godunov (1959) and since then, the technique has been improved over the years, resulting in high-resolution schemes as the ones written by Kurganov & Tadmor (2000) or Alcrudo & Garcia-Navarro (1993). In Nichols & Hirt (1971) and Nichols & Hirt (1975) there are also good examples of this method.

Marker-and-Cell (MAC) Method

The Marker-and-Cell (MAC) method, originally introduced by Harlow & Welch (1965), was the first method able to solve time-dependent free surface flows. The MAC method is based on a fixed Eulerian grid, in which the fluid transports a set of imaginary marker points that move along with it. The markers are present only in one of the phases and the cells that do not contain markers are empty. In this method, the free surface is determined by isolating the cells with a marker that are surrounded by, at least, one empty cell.

This method has demonstrated to provide accurate solutions for a wide range of complicated free-surface problems. However, the MAC method has fallen into disuse due to the considerable computational time and the large amounts of memory that requires.

Boundary Element Method (BEM)

As mentioned above, one of the main problems associated to the MAC method, is the large amount of memory and CPU time that it requires. On the contrary, the Boundary Element Method solves this inconvenience working with marker points placed only in the interface, instead in all the cells of one of the phases. Therefore, only the boundaries are traced with markers and the general equations that rule the problem are solved only in those boundaries.

Since only elements on interfaces are involved in the solution, the set-up of the problem, or later modifications, can be done easily and quickly. In addition, the amount of CPU time and memory consumed by this approach are ridiculous compared with the ones employed by the MAC method with similar levels of resolution. The books Pozrikidis (1997) and

Ang (2007) are a good approach to the ideas proposed by this method.

Despite all of the advantages of this method, the Boundary Element Method presents certain difficulties in the implementation of unsteady 3D cases, mainly associated with the placement and tracking of the markers on a 3D interface. One common situation is the loss of information in the regions where the markers disappear or remain at large distances from each other. In Nichols & Hirt (1975) the advantages and limitations of this method are revised.

In the section 4.3, the BEM method is widely explained and applied to the corner wave flow.

Volume-of-Fluid (VOF) Method

The Volume of fluid method (VOF) is part of the family of the Eulerian models. The main characteristic of this method is that it solves a single set of momentum equations and, later, calculates the volume fraction of each phase associated to each cell of the computational grid. Then, the free surface is determined in the nodes of the grid in which the maximum gradient of the volume fraction is found. This method was originally formulated by Nichols & Hirt (1980) and Hirt & Nichols (1981),

As mentioned above, the basis of this method lay down on the precise determination of the volume fraction of each single phase in all the cells of the domain. Hence, if the q^{th} fluid's volume fraction in the cell is denoted as α_q, the following three conditions are possible:

* $\alpha_q = 0$: The cell is empty (of the q^{th} fluid).

* $\alpha_q = 1$: The cell is full (of the q^{th} fluid).

* $0 < \alpha_q < 1$: The cell contains the interface between the q^{th} fluid and one or more other fluids.

Based on the local value of α_q, the appropriate properties and variables are assigned inside of the control volume of every cell within the domain. In consequence, in each cell of the grid, the volume fractions of all phases sum to unity. Once the distribution over the cells of the volume fraction of a single phase is known, a geometry-reconstruction-algorithm is used to build up the location of the free surface.

The VOF method has demonstrated to be as powerful as the MAC method, while avoiding the computational cost of the second. Applications of the VOF model include stratified flows, free-surface flows, filling, sloshing, the motion of large bubbles in a liquid, the motion of liquid after a dam break, the prediction of jet breakup (with surface tension), and the steady or transient tracking of any liquid-gas interface. With these ideas in mind, in the next section 4.2, the VOF method is widely explained and applied to the

corner wave flow.

4.2 Corner Wave modeling using Volume-of-Fluid (VOF) Method

The VOF model has demonstrated to be very useful when the shape of the interface presents abrupt transitions. In particular, the application of the VOF model in the simulation of breaking waves, as the corner wave, has provided accurate and fast results. An example of the usability of such method in breaking waves can be found in Andrillon & Alessandri (2004), Jeong & Yang (1998) or Storr & Behnia (2000).

The VOF method tracks the interface between the phases involved in the problem by solving a continuity equation for the volume fraction of a single phase, α_q. For the q^{th} phase, this equation has the following form:

$$\frac{1}{\rho_q}\left[\frac{\partial}{\partial t}(\alpha_q\rho_q) + \nabla\cdot(\alpha_q\rho_q\vec{v}_q) = S_{\alpha_q} + \sum_{p=1}^{n}(\dot{m}_{pq} - \dot{m}_{qp})\right] \tag{4.1}$$

where ρ_q and $\vec{v}_q$ are the density and the velocity of the phase q, $\dot{m}_{qp}$ is the mass transfer rate from the phase q to the phase p while $\dot{m}_{\text{pq}}$ is the opposite and n is the number of phases. This method also provides the possibility of adding a source term, S_{α_q} to the right-hand side of the equation. In case of working with only two phases (i.e. water-air), the equation (4.1) is solved only once (in general $n-1$ times), since the volume fraction of the other phase is directly returned by the conservation of volume fraction in each cell,

$$\sum_{q=1}^{n}\alpha_q = 1. \tag{4.2}$$

The continuity volume fraction equation, (4.1), may be solved either through an implicit or explicit time scheme. The use of an implicit scheme is appropriate to compute steady-state solutions when the intermediate-steps results are not relevant. These schemes have proved to be more accurate for similar orders than the explicit ones. An example of a discretization implicit scheme is:

$$\frac{\alpha_q^{k+1}\rho_q^{k+1} - \alpha_q^k\rho_q^k}{\Delta t}V + \sum_f(\rho_q^{k+1}U_f^{k+1}\alpha_{q,f}^{k+1}) = \left[S_{\alpha_q} + \sum_{p=1}^{n}(\dot{m}_{pq} - \dot{m}_{qp})\right]V, \tag{4.3}$$

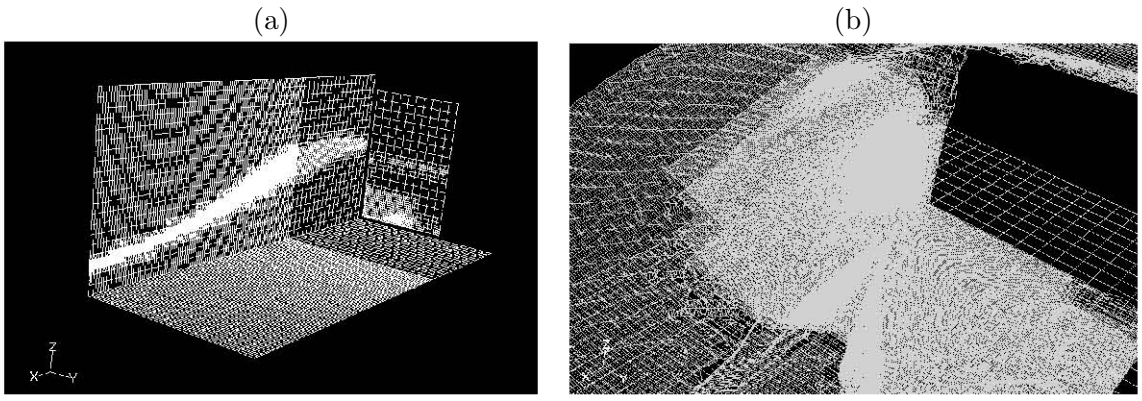

Figure 4.1: (a) Grid used to implement the VOF model in the corner wave problem. In order to obtain an accurate free surface shape and location, the grid was refined several times around $\alpha_{water} \in [0.4 - 0.6]$. (b) A detail of the grid refinement near the corner wave.

where $k+1$ is the index for the new time step, k is the index for previous time step, $\alpha_{q,f}$ is the face value of α_q, V is the cell's volume and U_f is the norm volume flux through the face f of the cell. Due to the implicit character of this formulation, equation (4.3) requires an estimation of the α_q^{n+1} volume fraction values at the $n+1$ time step. To approximate this value, equation (4.3) is solved iteratively for $n-1$ of the phase volume fraction at each time step. Once the volume fraction is computed over the grid domain, the free surface is determined by reconstruction schemes that interpolate the fluxes between cells with different volume fraction.

To apply the VOF method to the corner wave studied in this work the commercial software FLUENT was used. To set up the problem, a grid with 2.5 million of cells, 7.5 million of faces and 2.7 million of nodes was used. This grid, was built as similar as possible to the San Diego water channel (see Chapter 3) and refined several times around the free surface location. A general view of the grid is shown in figure 4.1 whereas a detailed view of the cross-section of the grid near the free surface location is shown in figure 4.2.

To solve the problem, an inviscid formulation was applied to the flow while the time was used as the convergence parameter, resulting the final free surface location when its shape and location remained steady. The Pressure-Velocity coupling was managed with a PISO solver. To reconstruct the free surface, a geometric reconstruction scheme, namely GEO-reconstruct, implemented in FLUENT, was used. This scheme reconstructs the free surface in three steps:

- Firstly, the scheme calculates the position of the linear interface relative to the center

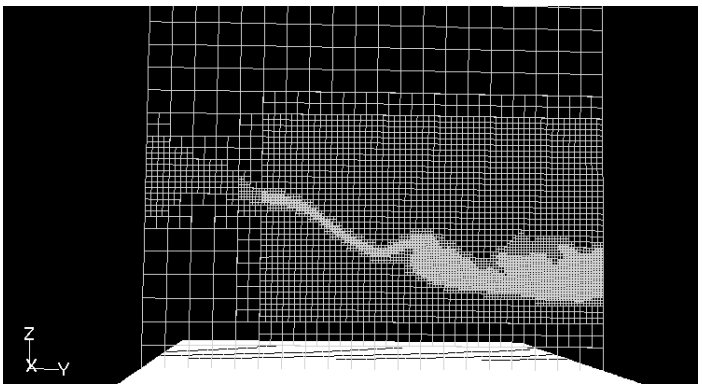

Figure 4.2: A cross section of the grid showing the different levels of refinement around the free surface.

of each partially-filled cell.

- Secondly, the scheme calculates the advecting amount of fluid through each face using the computed linear interface representation.
- Finally, the scheme calculates the volume fraction in each cell using the balance of fluxes calculated during the previous step .

In order to initialize the flow, a canonical case of the corner waves was settled in the laboratory. Then, all the geometric parameters involved were measured and implemented into the initial conditions of the numerical set-up. Finally, to provide an accurate initial condition for the velocity field, PIV measurements were performed upstream of the plate. A detailed explanation of the PIV measurements is exposed in the appendix B.

The convergence time was around 7-10 days. To obtain an accurate free surface location from the simulation, an isosurface of $\alpha_{water} = 0.5$ was computed. A general result of the simulation for a volume fraction range $\alpha_{water} \in [0.5 - 1]$ can be seen in figure 4.3.

The results of the simulation of the corner wave using the VOF model were compared with the LIF experiments reported in Chapter 3. In figures 4.4 and 4.5, the free surface location calculated with the VOF method is plotted with the results of the LIF experiments showing the ability of the code to capture the emplacement of the free surface.

4.2.1 Volume-of-Fluid (VOF) Method Limitations

Although the ability of the VOF method to capture the free surface location is clear, the method has a series of disadvantages. One of the main problems associated with the VOF method, is the possibility of finding discontinuities, or numerically smoothed velocity and

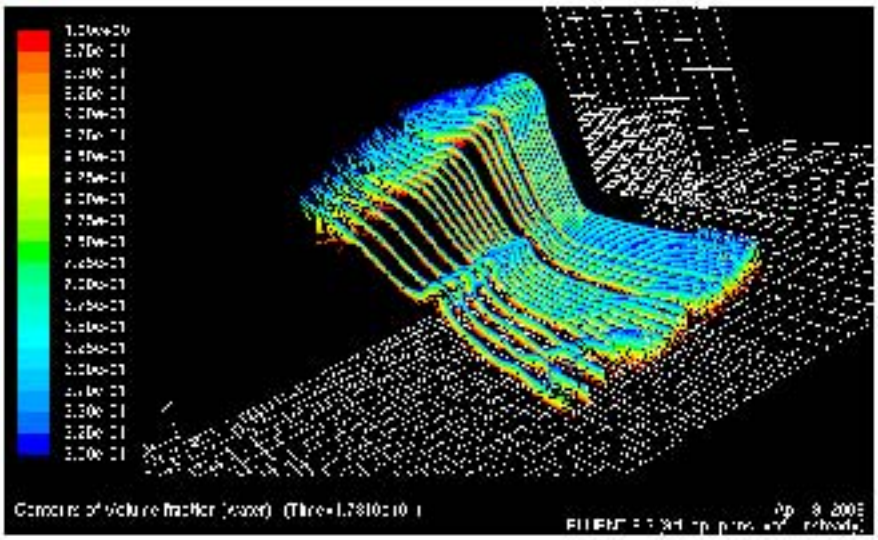

Figure 4.3: Result of the volume fraction range $\alpha_{water} \simeq [0.5 - 1]$ for the corner wave flow. Notice that the superior level of refinement near the corner wave allows a fine determination of the free surface in that region whereas the flow near the walls can not be determined precisely due to lowers levels of refinement.

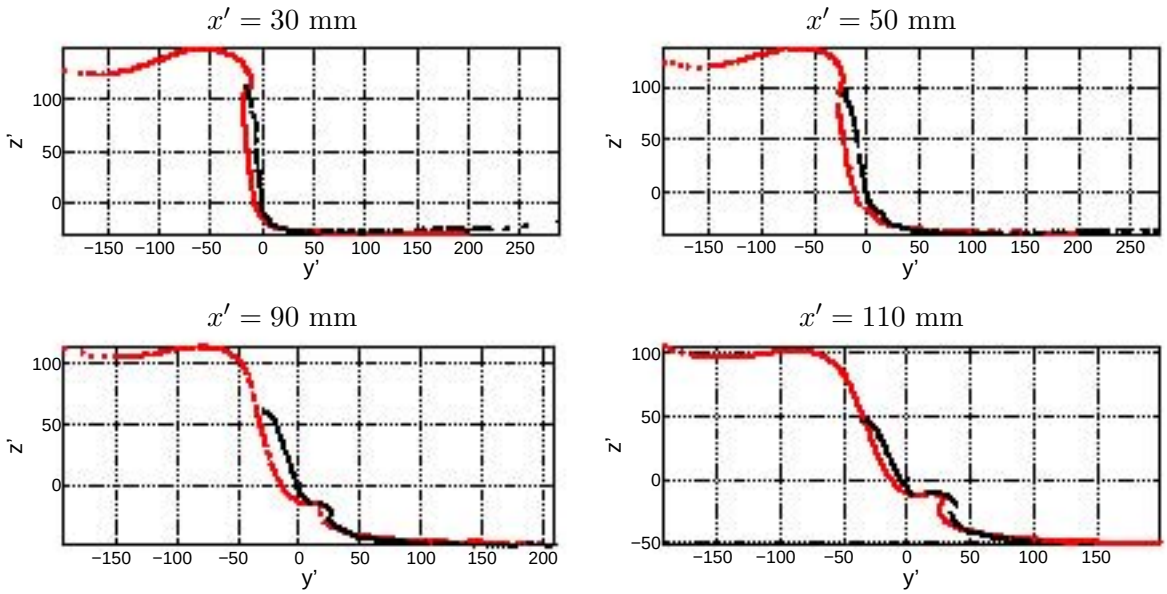

Figure 4.4: Comparison between cross section slides of the free surface location computed with the VOF model and the one obtained with the LIF experiments. The red line represents the VOF's free surface location for $\alpha_{water} = 0.5$. The black line represents the free surface location obtained with the LIF experiments. The sections are placed at $x' = 30$ mm, $x' = 50$ mm, $x' = 90$ mm and $x' = 110$ mm.

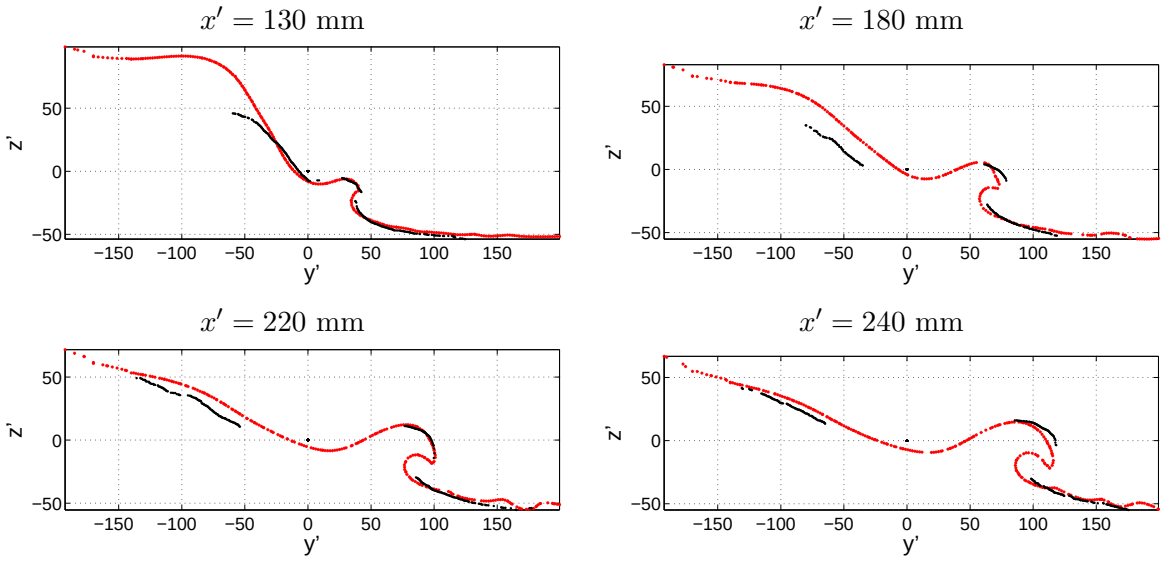

Figure 4.5: Comparison between cross section slides of the free surface location computed with the VOF model and the one obtained with the LIF experiments. The red line represents the VOF's free surface location for $\alpha_{water} = 0.5$. The black line represents the free surface location obtained with the LIF experiments. The sections are placed at $x' = 130$ mm, $x' = 180$ mm, $x' = 220$ mm and $x' = 240$ mm.

pressure profiles, at the free surface location.

This problem is found to be associated not only to the thickness of the interface, in which the free surface reconstruction scheme dissipates the velocity along the cells with $\alpha < 1$ but also, to the difficulty achieving the zero divergence condition to a high degree of precision at every time step. Carlson *et al.* (2008) relate unexpected free surface profiles while using FLUENT and Abdolmaleki *et al.* (2004), applying the same software to the case of a breaking dam problem, found disagreements in the velocity profile at the free surface when comparing them with the predicted ones. Wood *et al.* (2003) also report numerical problems associated with the VOF method in the analysis of steep gravity waves.

For this reason, even when the free surface location is captured precisely, the information of the velocities and pressure in the free surface can not be entirely trusted and an alternative numerical approach should be used to model the corner wave.

4.3 Corner Wave modeling using Boundary Element Method (BEM)

It has been demonstrated that the VOF model, presented in section 4.2, describes precisely the free surface location. However, as explained in 4.2.1, even thought the free surface is properly located, the method is dissipative near the free surface leading to unphysical velocities near the air-water interface.

In order to capture not only the shape of the free surface but also its precise velocity field, this section applies a Boundary Element Method (BEM) to the corner wave flow by using the 2D+T approximation explained in Chapter 2.

As demonstrated in chapter 2, the velocity field in the 2D+T approximation can be written in terms of the harmonic velocity potential ϕ that satisfies the Laplace's equation $\nabla^2\phi = 0$. Complementing this formulation, the no-penetration conditions $\partial_{\vec{n}}\phi = 0$ are applied to the walls and the bottom of the channel and finally, the Bernoulli equation can be used to predict the evolution of the velocity potential along the free surface,

$$\frac{D\phi}{Dt} = \frac{|\nabla\phi|^2}{2} - \frac{P_{atm}}{\rho} + \vec{g}\cdot\vec{x}, \tag{4.4}$$

where $\frac{D}{Dt}$, is the substantial derivative, $\vec{g}$ is the acceleration of the gravity vector, ρ is the water density and $\vec{x}$ is the position vector. Finally, the kinematic condition declaring the free surface as a fluid surface, completes the formulation.

In Pozrikidis (1997) it can be found that, using the appropriate boundary conditions, the harmonic potential, ϕ, and its normal derivative along the free surface, $\partial_{\vec{n}}\phi$, can be expressed in terms of the standard boundary-integral representation,

$$\phi(\vec{x_0}) = -2\int_C G(\vec{x},\vec{x_0})[\vec{n}(\vec{x})\cdot\nabla\phi(\vec{x})]\,dl(\vec{x}) + 2\int_C^{PV} \phi(\vec{x})[\vec{n}(\vec{x})\cdot\nabla G(\vec{x},\vec{x_0})]\,dl(\vec{x}), \tag{4.5}$$

in which, $\vec{x_0}$ is a point that lies on the free surface C, l is the arc length along C and $\vec{n}$ is the normal vector pointing to the fluid side. In this formulation, the integral $\int_C^{PV}$ is an improper but convergent integral called *a principle-value integral*.
Notice that, when applying equation (4.5) to the corner wave flow, the Green's function $G(\vec{x},\vec{x_0})$ is the Neumann function of the Laplace's equation for a semi-infinite strip confined by the three walls (left, right and bottom), $G(\vec{x},\vec{x_0}) = -\frac{1}{2\pi}\ln r$. Keep in mind that to impose the no-penetration condition at the walls, the Green's function has to include also the potential of the symmetry image points with respect to the rigid boundaries.

Therefore, equation (4.5) takes the following form;

$$\phi(\vec{x_0}) = -\frac{1}{\pi}\int_{W,C}^{PV} \frac{\vec{x}-\vec{x_0}}{r^2}[\vec{n}(\vec{x})\phi(\vec{x})]dl(\vec{x}) + \quad \frac{1}{\pi}\int_C \ln r\vec{u}(\vec{x})\cdot\vec{n}(\vec{x})\,dl(\vec{x}), \qquad (4.6)$$

which returns the value of the potential in a certain point of the free surface, $\vec{x_0}$, in our problem. In equation (4.6), W denotes the channel walls and bottom of the channel, whereas $\vec{u}$ is the velocity vector and $r = |\vec{x} - \vec{x_0}|$.

Nakayama (1990) proposes an efficient computational procedure to solve the coupled equations (4.4)-(4.6) based in the following steps :

- Compute the velocity potential, ϕ, using (4.4).
- Solve the integral equation (4.6) for $\vec{n}(\vec{x})\cdot\nabla\phi(\vec{x})$ and obtain the normal component of the velocity vector.
- Compute the tangential derivative of the potential ϕ, and obtain the tangential velocity.
- Using the velocity field, evolve the free surface with a time marching scheme to its new location and return to first step.

Following these four steps, the evolution of the free surface can be traced and the values of the potential and the velocities at that location obtained, at each time step.

Numerical Procedure

In order of applying the numerical procedure exposed in the previous section to the considered problem, the initial free surface should be traced with marker points that evolve with the free surface velocity in each time step. Observe that, if the marker points move only with the normal component of the velocity of the free surface, they can be considered as material point particles. However, if the markers are allowed to move with both components of the velocity, they should be treated as computational markers.

The free surface shape can be approximated by a function that passes through the instantaneous position of the marker points. This function can be obtained by the use of polygonal functions or by interpolated splines. It is obvious that, as the number of marker points increases, the precision in the determination of the free surface is also improved. However, the election of the number of marker points should also take in account the Courant condition to prevent numerical instabilities.

The segments that connect a pair of markers are considered moving boundary elements. Each one of them, i, of a total of N, has its own constant velocity potential ϕ_i and its derivative, denoted by $(\frac{\partial\phi}{\partial n})_i$. Under this nomenclature, the integral equation (4.5), can be discretized as,

$$\sum_{i=1}^{N}(\frac{\partial\phi}{\partial n})_i \int_{E_i} G(\vec{x},\vec{x_0})dl(\vec{x}) = \ -\frac{1}{2}\phi(\vec{x_0}) + \sum_{i=1}^{N}\phi_i \int_{E_i}^{PV} \vec{n}(\vec{x})\cdot\nabla G(\vec{x},\vec{x_0})dl(\vec{x}), \quad (4.7)$$

where $\vec{x_0}$ is identified as the central point of the j^{th} boundary element, $x_j^{\vec{M}}$. With this in mind, it becomes possible, to derive a system for the N unknown values of the normal derivative of the potential $(\frac{\partial\phi}{\partial n})_i$, calling $\phi(x_j^{\vec{M}}) = \phi_j$,

$$\sum_{i=1}^{N}(\frac{\partial\phi}{\partial n})_i \int_{E_i} G(x_j^{\vec{M}},\vec{x_0})\, dl(\vec{x}) = \ -\frac{1}{2}\phi_j + \sum_{i=1}^{N}\phi_i \int_{E_i}^{PV} \vec{n}(\vec{x})\cdot\nabla G(x_j^{\vec{M}},\vec{x_0})dl(\vec{x}) \quad (4.8)$$

where,

$$-\frac{1}{2}\phi_j+\sum_{i=1}^{N}\phi_i \int_{E_i}^{PV} \vec{n}(\vec{x})\cdot\nabla G(x_j^{\vec{M}},\vec{x_0})dl(\vec{x}) = \sum_{i=1}^{N}\phi_i \left[\int_{E_i}^{PV} \vec{n}(\vec{x})\cdot\nabla G(x_j^{\vec{M}},\vec{x_0})dl(\vec{x}) - \frac{1}{2}\delta_{i,j}\right] \quad (4.9)$$

for $j = 1, ..., N$. The integrals contained in expression (4.9) can be computed using a Gauss Legendre quadrature and the system solved by Gauss elimination. Once the solution is attained, the location of the markers must be updated. If the marker is moved with both components of the free surface velocity, the new position can be obtained using $\frac{d\vec{x}}{dt} = \vec{u}$, whose scalar components are:

$$\frac{dx_i}{dt} = u_x(x_i, y_i); \qquad \frac{dy_i}{dt} = u_y(x_i, y_i) \quad (4.10)$$

where the free surface velocity comes from $\vec{u} = (\frac{\partial\phi}{\partial n})\vec{n} + (\frac{\partial\phi}{\partial l})\vec{t}$, being l the arc length along the free surface with normal vector $\vec{n}$ and tangential vector $\vec{t}$.

On the other hand, if the marker points displacement depends only on the normal free surface velocity, equations (4.10) become:

$$\frac{dx_i}{dt} = (\frac{\partial\phi}{\partial n})_i n_x(x_i, y_i); \qquad \frac{dy_i}{dt} = (\frac{\partial\phi}{\partial n})_i n_y(x_i, y_i), \quad (4.11)$$

and after relocating the markers, the potential should be updated using a slightly varied form of equation (4.4):

$$\frac{\partial\phi}{\partial t} = |\vec{u}\cdot\vec{n}|^2 - \frac{1}{2}|\vec{u}|^2 - \frac{P_{atm}}{\rho} + \vec{g}\cdot\vec{x} \quad (4.12)$$

To implement the above discretization a Fortran code was developed. The core of the code was the BEMLIB software written by Pozrikidis (see Pozrikidis (2002)), in which some modifications were made in order to refine the results and improve the convergence.

With the aim to achieve these purposes, part of the original code was rewritten using FORTRAN 95 in order to take advantage of the dynamic memory managing function. The use of dynamic memory functions allowed us to increase the number of points without impacting heavily on the memory consumption. Summarizing, the following modifications have been introduced:

- The nodes are redistributed at each time step, increasing the nodes density in the areas in which the curvature of the free surface is maximum, enlarging, in consequence, the spatial resolution of such zones. More precisely:

$$ds_i = ds_{min} + \alpha_s \frac{|k'_{max}| - |k'_i|}{|k'_{max}| - |k'_{min}|}, \tag{4.13}$$

  where ds_{min} is the minimum element length, k' is the curvature, smoothed with a median filter,

$$k'_i = \frac{1}{3}(k'_{i-1} + k'_i + k'_{i+1}), \tag{4.14}$$

  and α_s is a constant chosen in order to maintain the total length of the free surface, S_{total}, after the redistribution,

$$\sum_{i=1}^{N} ds_i = S_{total} \Rightarrow S_{total} = N \cdot ds_{min} + \alpha_s \frac{N|k'_{max}| - \sum_{i=1}^{N} |k'_i|}{|k'_{max}| - |k'_{min}|}. \tag{4.15}$$

  Finally, the nodes are redistributed using linear interpolation.

- The original time marching scheme, an explicit Euler scheme, is substituted by a modification of a third order Runge-Kutta scheme. This modification consists in a low-storage, hybrid implicit/explicit, three-sub-step scheme of third order. However, instead of fixing the time step, Δt, it is computed maintaining constant the CFL condition, such ,

$$\Delta t^{k+1} = \mathrm{CFL} \cdot \frac{\mathrm{ds_{min}}}{\mathrm{Un,max^k}}, \tag{4.16}$$

  where $\mathrm{Un,max^k}$ is the maximum of the normal velocity in the previous time step. The details of this scheme can be found in the Appendix of Spalart *et al.* (1991).

- The memory is allocated dynamically, which has eliminated the limitation of nodes.

- The linear system is solved using the routine DGESV from LAPACK.

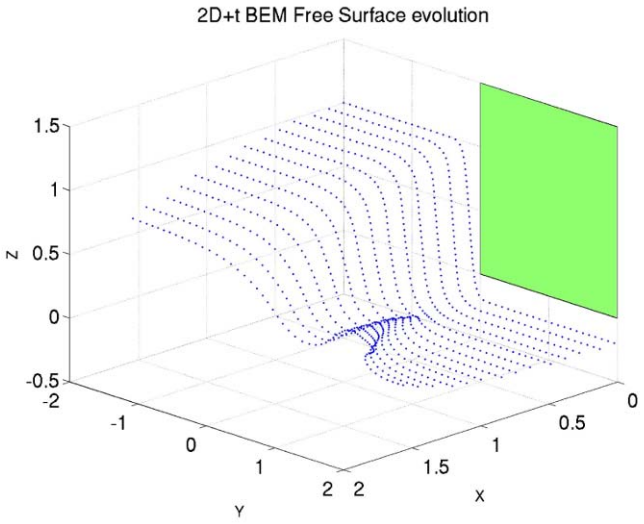

Figure 4.6: Free surface evolution computed with the BEM represented in three dimensions using $x = U_1 t$

To test the accuracy of the code, an experimental free surface profile of a canonical plunging breaker, identified as case A of table 3.1, was reconstructed and used as the initial condition. Such profile was obtained using the LIF experiments (see figure 3.3(a)) immediately downstream from the plate at $x = 0.12$, ($x' = 25$ mm). Finally, the initial velocity potential was set to zero, $\phi = 0$.

Figure 4.6 shows the results of the simulation when undoing the 2D+T approximation by $x = U_1 t$. As can be seen, the couple BEM-2D+T approximation qualitatively reproduces the development of the corner wave.

Figure 4.7 shows the comparison between the experimental free surface location, obtained using the LIF experiments reported in Chapter 3, and the computed free surface obtained with the 2D+T approximation. To avoid the "vena contracta" effect of the 3D case, the numerical free surface location is shown with its origin of coordinates relocated to the crest of the wave, at each cross section x'.

As shown, this method is not able to capture some three dimensional effects of the sluice gate case due to the assumption that the potential ϕ is originally null. On the other hand, the uses of a BEM provides exact information of the velocities at the free surface, which are critical to understand the formation mechanism of the corner wave.

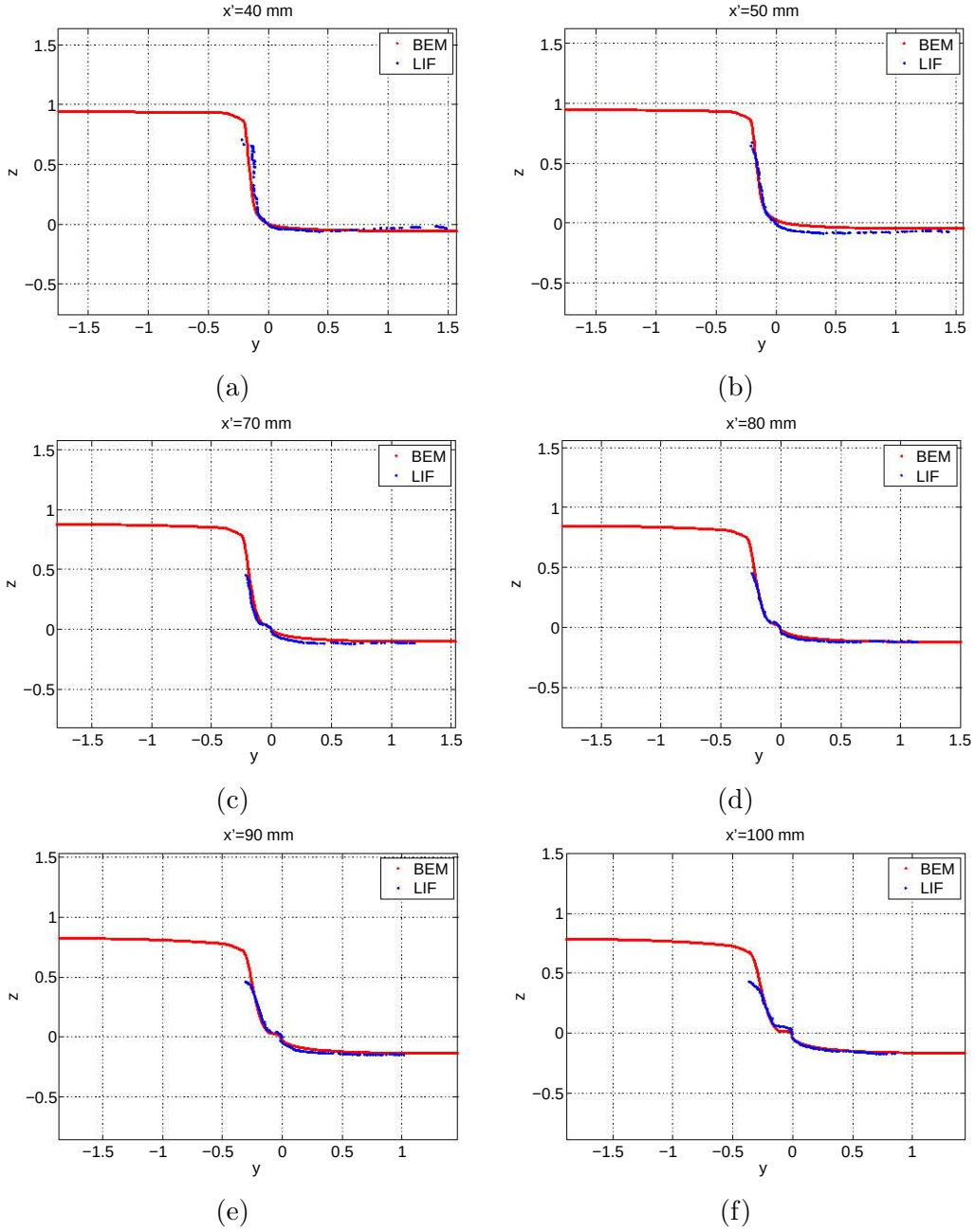

Figure 4.7: Results of the numerical 2D+T free surface location versus the experimental one. The sections $y - z$ are located at (a) $x' = 30mm$, (b) $x' = 50mm$, (c) $x' = 70mm$, (d) $x' = 80mm$, (e) $x' = 90mm$, (f) $x' = 100mm$, from the plate. The blue line represents the LIF experiments and the red one the results of the Boundary element method for the 2D+T equations. Both lines are plotted using the crest location as the coordinate origin in order to represent the good agreement between both methods when approaching to the corner wave.

4.4 Concluding Remarks

In this chapter, a numerical receipt to reproduce the corner wave flow has been investigated. The Volume of Fluid (VOF) method has demonstrated to be a very suitable method to capture the free surface shape and location, but presents difficulties in obtaining accurate results of the velocity field near the free surface.

The Boundary Element method (BEM) reproduces the corner wave flow, validating the 2D+T approximation for the flow, which is shown to remains adequate not only for large Froude numbers but also for the moderate ones found in the experiments. However, the assumption of a initial null potential velocity , $\phi = 0$, limits the possibility of reproducing the *vena contracta* effect, which appears in the three-dimensional case.

In the next chapter the velocity results of the Boundary Element Method and its implications are explored and analyzed.

CHAPTER
FIVE

Formation and Initial Development of a Corner Wave

5.1 Introduction

This chapter is dedicated to discuss and unveil the formation and development mechanisms of a corner wave. To that purpose, a combination of analytical and numerical tools, of which some were previously described in chapters 2, 3 and 4, are used. To face this challenge, and considering that the potential boundary element method reproduces qualitatively the flow, as shown in section 4.3, the 2D+T approximation will be maintained all along this chapter. To study separately the different aspects involved in both processes this chapter is divided into five sections;

1. Section 5.2 undertakes the way to understand the physics involved in the formation of the corner wave, using the results of the velocity profiles obtained with the Boundary Element Method. Subsection 5.2.2 presents a Pressure-Impulse Asymptotic analysis which, by expanding the problem in integer powers of time, reproduces such velocity profiles.

2. Section 5.3 contains an analysis of the selfsimilar structure of the flow near the corner at short times.

3. In section 5.4 an analysis of the initial development of the free surface near the corner at short times is carried out.

4. Section 5.5 contains an analysis of the different parameters of the flow which can affect the formation or the initial development of the wave.

5. Section 5.6 presents an analytical solution for the far field of the wave corner flow.

Finally, section 5.7 is committed to conclusions.

5.2 Formation mechanism of a corner wave

5.2.1 Glimpsing the physics ...

In Chapter 4, the potential flow theory was applied to study the corner wave flow, under the 2D+T approximation, providing accurate results of the free surface evolution, except for the region driven by the *vena contracta* effects, due to the initial assumption of null potential at the free surface immediately downstream the plate. It will be shown that, the careful analysis of the velocity field at the free surface reveals the underlying mechanism responsible for the formation of the corner wave.

Figures 5.1 and 5.2 show the time evolution of the tangential and normal velocities, u_t and u_n, at a typical free surface found in the experiments reported in Chapter 3. Looking at the time development of the tangential velocity, it can be seen that, at short times, the fluid particles at the free surface experience a fast acceleration and a later deceleration near the point of maximum curvature. Moreover, when time advances and the wave rises up, the tangential velocity changes in sign.

It is essential to examine in detail the meaning of the form of the tangential velocity distribution at the free surface, because it unveils the initial formation mechanism that rises up the corner wave. Observing the initial time steps, it can be reasonably asserted that, due to these changes in the mentioned velocity distribution, the fluid particles are directed towards the point of maximum curvature where, by conservation of mass, they cannot concur simultaneously and therefore, require a vertical outlet in the form of a jet. This jet is the ultimate responsible for the emergence of a bump that, over time, will result in the formation of the corner wave.

Assaying carefully the normal velocity profile at the free surface a maximum can be appreciated, which coincides with the point of maximum curvature at short times. This maximum in the normal velocity profile changes in position in subsequent stages, evolving fixed to the head of the jet, which later becomes the crest of the wave.

This coincidence of the maximum of the normal velocity distribution with the crest of the wave along time, allows the optimal monitoring of its location, which grants an appropriate tracking of the trajectory of the crest of the wave.

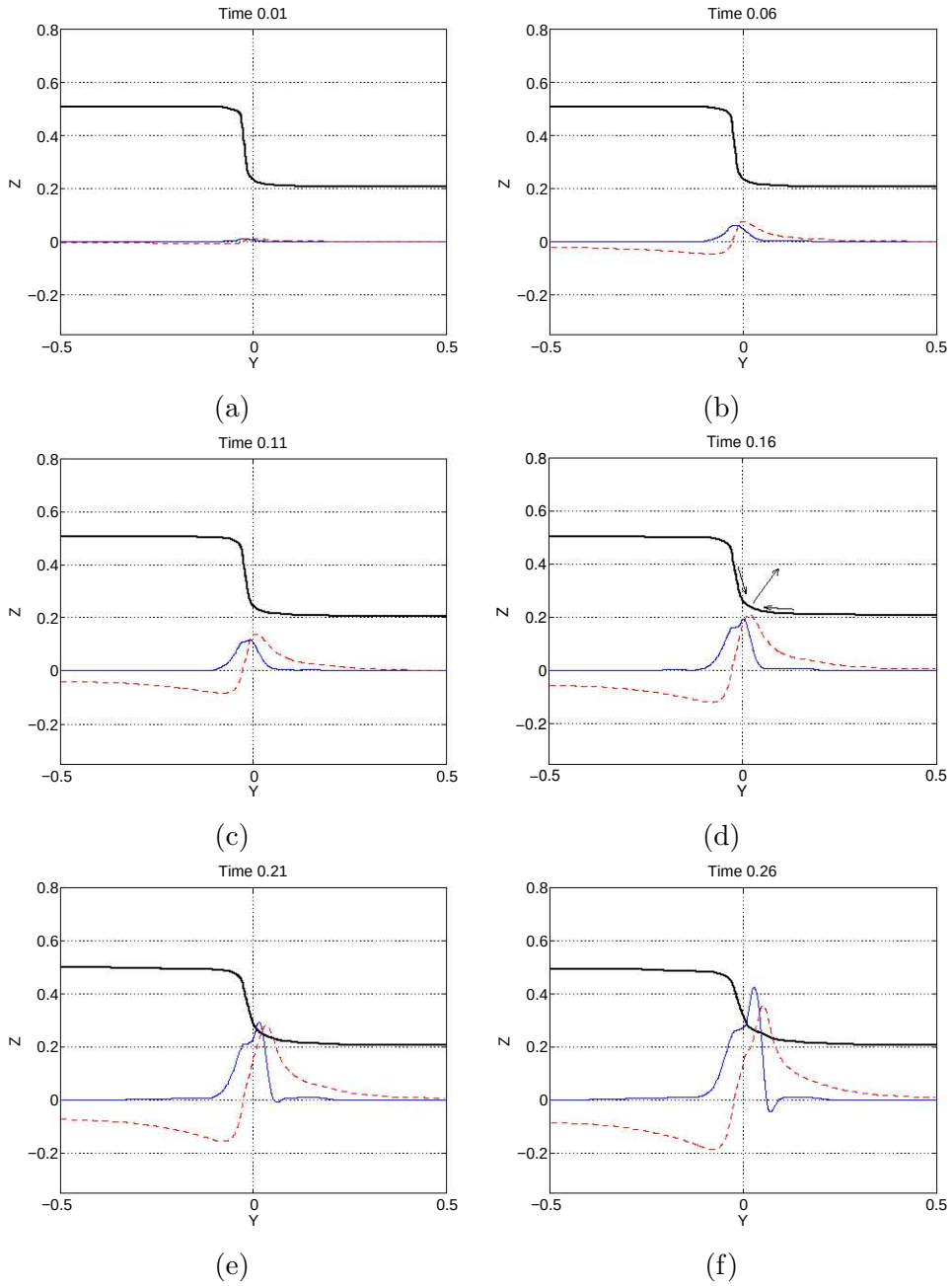

Figure 5.1: Results of the BEM numerical free surface evolution together with the tangential velocity and the normal velocity for the dimensionless time (a) $t = 0.001$, (b) $t = 0.006$,(c) $t = 0.011$,(d) $t = 0.016$, (e) $t = 0.21$, (f) $t = 0.26$. The thick line represents the free surface evolution. The blue solid line is the instantaneous value of the tangential velocity, u_t, whereas the red dashed line is the instantaneous value of the normal velocity, u_n. A hyperbolic tangent function was used to describe the initial free surface shape and used to initialize the BEM code. In this figure, the free surface is scaled and the origin of coordinates displaced in order to clarify the velocity profiles. In (d), the arrows schematize the normal and tangential velocities near the point of maximum curvature.

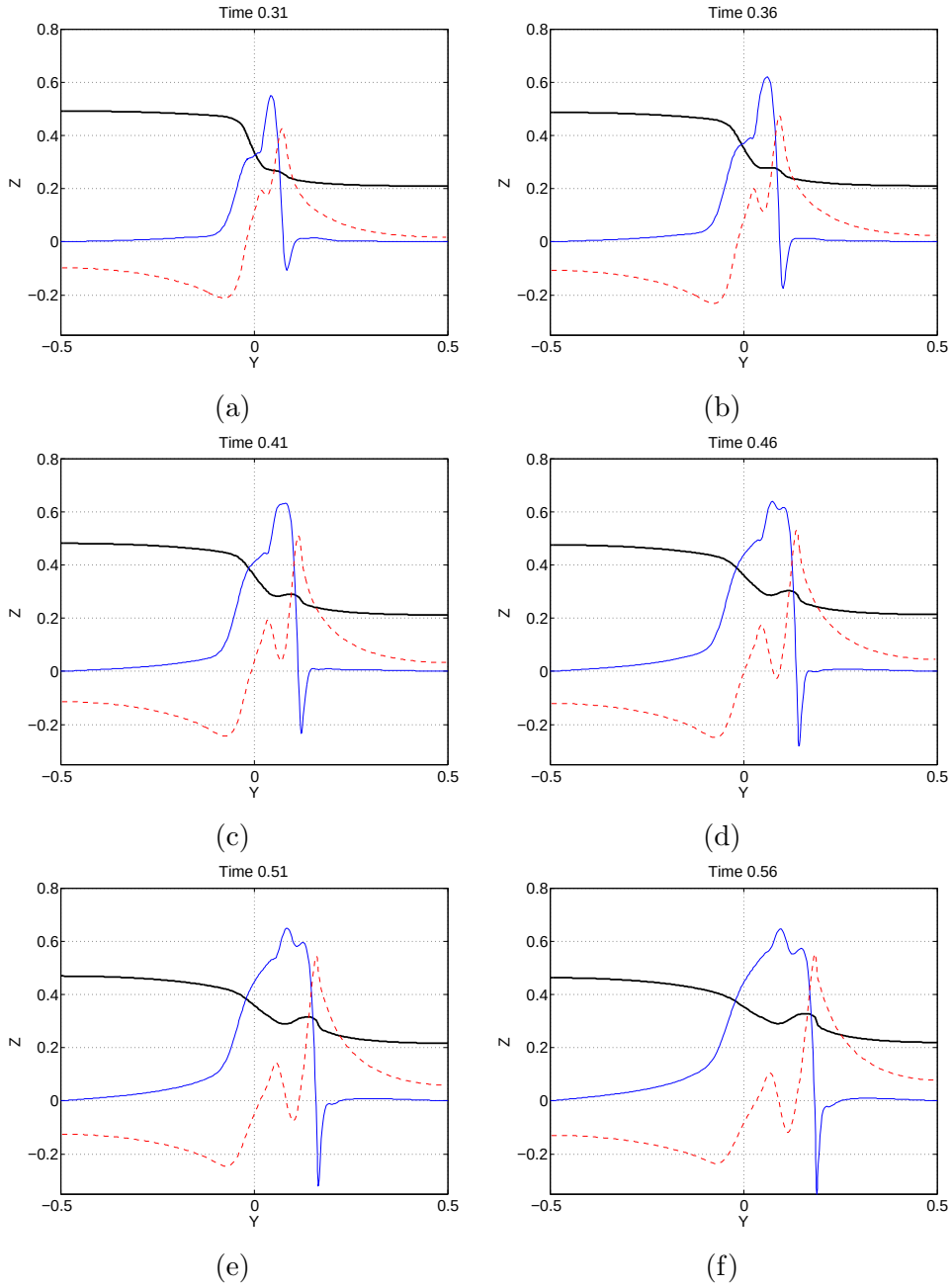

Figure 5.2: Results of the BEM numerical free surface evolution together with the tangential velocity and the normal velocity for the dimensionless time (a) $t = 0.311$, (b) $t = 0.36$,(c) $t = 0.41$,(d) $t = 0.46$, (e) $t = 0.51$, (f) $t = 0.56$. The thick line represents the free surface evolution. The blue solid line is the instantaneous value of the tangential velocity, u_t,whereas the red dashed line is the instantaneous value of the normal velocity, u_n.

5.2.2 Pressure-Impulse (P-I) Asymptotic analysis at short times $t \ll 1$

At the time that the flow starts its motion, at $t = 0$ or in the 3D case, immediately downstream from the plate, there exists a sudden change in the boundary conditions. This alteration of the boundary conditions causes a pressure impulse in the fluid, as explained by Batchelor (1967) (p.471). Once this impulse is created, the free surface deformation starts, given $t = 0^+$. This instantaneous impulsive motion can be captured, for short times, $t \ll 1$, using a Pressure-Impulse (P-I) asymptotic analysis combined with the 2D+T approximation. This kind of analysis has demonstrated to provide accurate results in similar problems, as i.e. in the ones studied by Iafrati & Korobkin. (2004) or Needham *et al.* (2007).

As explained in chapter 2, the 2D+T approximation leads to the system of equations (2.28):

$$\nabla^2\phi = 0 \qquad (t > 0, (y, z) \quad \text{in} \quad \Omega(\text{t})) \tag{5.1}$$

$$\partial_t\phi + \frac{1}{2}|\nabla\phi|^2 + h = 0 \tag{5.2}$$

$$\partial_t h + \partial_y\phi\partial_y h - \partial_z\phi = 0, \tag{5.3}$$

where equations (5.2) and (5.3), are the dynamic and kinematic conditions that must be applied on the free surface, $F(y, t) = z - h(y, t) = 0$.

The P-I asymptotic analysis consists in expanding the potential, ϕ, and the free surface function, h, in powers of a small parameter, in this case the time, t, with the aim of predicting the initial deformation at the free surface. Applying this idea to the system (5.1), both functions read, up to terms of order $O(t^3)$,

$$\phi = \varphi_1(y, z)t + \varphi_2(y, z)t^2 + \varphi_3(y, z)t^3 + O(t^3), \tag{5.4}$$

for the potential and,

$$h = h_0 + \xi_1(y)t + \xi_2(y)t^2 + O(t^2) \tag{5.5}$$

for the free surface function.

This "initial" asymptotic expansion corresponds to the region between the "initial" solution, where $t \sim 1/Fr_l$, where Fr_l is the local, time depending, Froude number based on the characteristic length of the flow near the corner, $Fr_l \sim \frac{O(\nabla\phi)}{O(\sqrt{h})}$, and the "intermediate" solution where t becomes of order $t \sim O(1)$

Introducing expressions (5.4) and (5.5) into system (5.1), the first order, $O(1)$, of the perturbed problem, with the initial condition $h(y, t = 0) = h_0$, becomes:

$$\begin{aligned} \nabla^2\varphi_1 = 0; \qquad h &= h_0 + \xi_1(y) \\ \varphi_1 + h_0 &= 0 \\ \partial_t h + \partial_y\varphi_1\partial_y h - \partial_z\varphi_1 &= 0 \end{aligned} \tag{5.6}$$

The condition $\varphi_1 + h_0 = 0$ in system (5.6), brings to light that the leading order of the potential ϕ, at the free surface, is directly described by the form of the initial free surface profile. Hence, the tangential velocity, at first order, can be exactly formulated as:

$$U_t = \frac{\partial\varphi_1}{\partial s} = \frac{-\partial_y h_0}{\sqrt{1 + (-\partial_y h_0)^2}}, \tag{5.7}$$

where s is the arc length of the free surface profile at each time step and h_0, the initial free surface profile.

Increasing the order of the solution to the order $O(t^2)$, we obtain,

$$\begin{aligned} \nabla^2\varphi_2 =& 0 \\ O(1) \Rightarrow& \varphi_1 + h_0 = 0 \\ O(t) \Rightarrow& 2\varphi_2 + \xi_1 = 0 \\ O(t^2) \Rightarrow& 3\varphi_3 + \frac{|\nabla\varphi_1|^2}{2} + \xi_2 = 0 \\ h =& h_0 + \xi_1 t + \xi_2 t^2 \\ O(1) \Rightarrow& \xi_1 = 0 \\ O(t) \Rightarrow& h\xi_2 + \varphi_{1,y} h_{0,y} - \varphi_{1,z} = 0 \end{aligned} \tag{5.8}$$

At order $O(t^2)$ the tangential and normal components of the velocity come out of the expressions $u_n = \partial_n\varphi_1 t + \partial_n\varphi_3 t^3$ and $u_t = \partial_t\varphi_1 t + \partial_t\varphi_3 t^3$, where φ_1 should be obtained by solving $\nabla^2\varphi_1 = 0$.

The second order of the potential, φ_3, is then obtained using,

$$3\varphi_3 + \frac{|\nabla\varphi_1|^2}{2} + \xi_2 = 0. \tag{5.9}$$

Pressure-Impulse Asymptotic validation

With the aim of checking the validity of the Pressure-Impulse formulation to describe the inception point and the initial development of the corner wave, the Laplace's equation, for the leading order of the potential, $\nabla^2\varphi_1 = 0$, must be solved. In the mentioned order, the boundary condition at the free surface depends on the form of its initial profile, $\varphi_1 = -h_0$,

whereas the no-penetration condition, $\partial_n \varphi_1 = 0$, applies at the walls.

The initial free surface profile was approximated by a hyperbolic tangent of the form $h_0 = a + b \cdot \tanh(y/\delta)$, where δ was used to smooth the curvature at the corner points $(0, 1)$ and $(0, 0)$. The parameter δ can be associated with the dimensionless "vena contracta effect" that appears in the steady 3D case, $\delta^* = \frac{\delta}{\Delta h} = \frac{h_g - h_1}{\Delta h}$, which for simplicity will be written in this section as δ. The use of such expression is justified for its similarity with the initial free surface profiles obtained in the LIF experiments reported in Chapter 3.

Using the mentioned initial free surface profiles, the Laplace's equation for φ_1 was solved using the BEM solver but adding the new boundary conditions. Figures 5.3 and 5.4 show the resulting tangential velocity distribution compared with the one obtained using the BEM for the original problem (5.1).

As shown in the mentioned figures, the leading order of the impulsive solution agrees fairly well with the original problem but only at short times, detaching from the original solution as time progresses. However, when including the $O(t^2)$ order terms, the solution is extended to longer times, which makes possible the application of the Pressure-Impulse analysis to capture the initial velocity profiles at the free surface and, therefore, the formation of the wave.

It must be pointed out that the usage of an hyperbolic tangent to set up the initial profile of the free surface schematically represents several types of hulls of real transom sterns. Thus, looking to the applicability of the above analysis in naval hydrodynamics, the possibility of tracking the crest of the wave, using the maximum in the normal velocity, can help to determine some non-well known aspects of the high speed vessel wake.

The knowledge of the different trajectories of the corner wave, can shed light on the potential location of the rooster tail. It is well known that the rooster tail appears in the symmetry plane of the hull, where the port side corner wave collides with the starboard one. Therefore, the time taken for the crest of one of the both corners waves to reach the midpoint of the stern, undoing the 2D+T transformation, determines the point of emergence of the rooster tail in three dimensions.

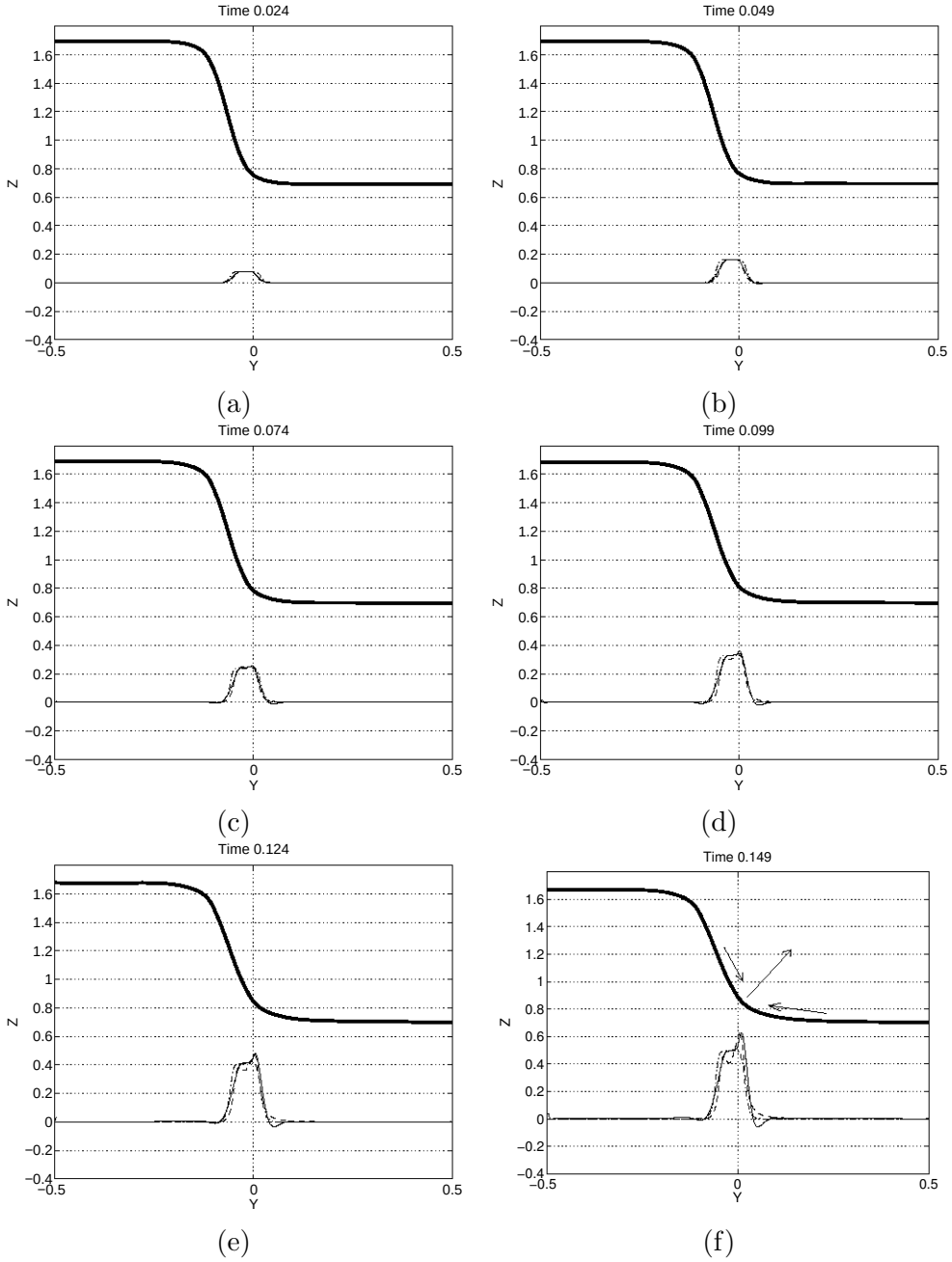

Figure 5.3: Results of the BEM numerical free surface evolution and tangential velocity compared with the pressure-impulse asymptotic solutions for time (a) $t = 0.024$, (b) $t = 0.049$,(c) $t = 0.074$,(d) $t = 0.099$, (e) $t = 0.124$, (f) $t = 0.149$. The thick line represents the free surface evolution. The solid line is the numerical instantaneous value of the tangential velocity u_t. The dashed line is the $O(t^2)$ order solution of the asymptotic and the dash-dot line is the $O(1)$ order one. As in figures 5.1 and 5.2, the initial free surface shape was approximated using an hyperbolic tangent. In this figure, the origin of coordinates is displaced in order to clarify the velocity profiles. In (f), the arrows schematize the normal and tangential velocities near the point of maximum curvature.

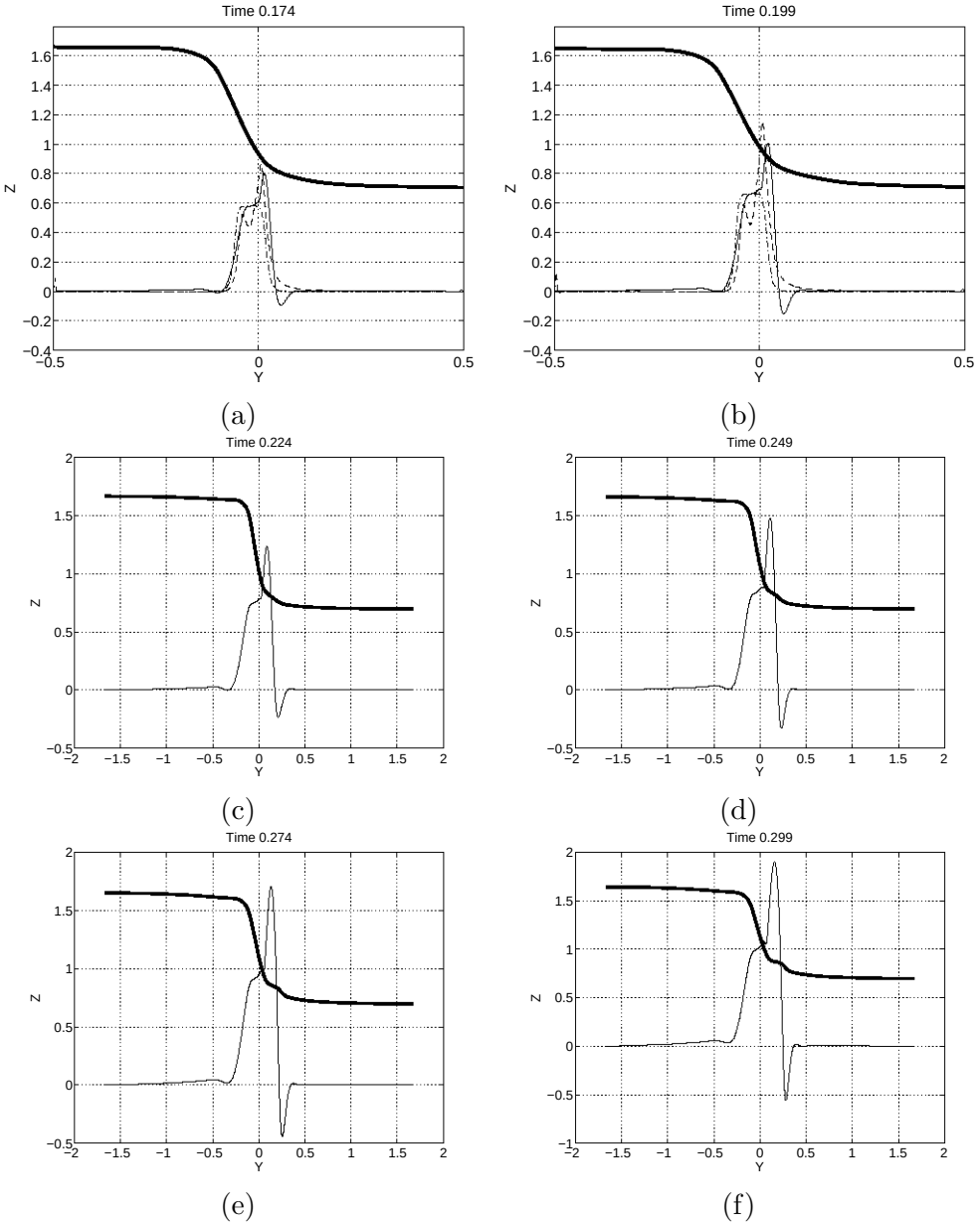

Figure 5.4: Results of the BEM numerical free surface evolution and tangential velocity compared with the pressure-impulse asymptotic solutions for time (a) $t = 0.174$, (b) $t = 0.199$ (c) $t = 0.224$, (d) $t = 0.249$,(e) $t = 0.274$,(f) $t = 0.299$. The thick line represents the free surface evolution. The solid line is the numerical instantaneous value of the tangential velocity u_t. The dashed line is the $O(t^2)$ order solution of the asymptotic and the dash-dot line is the $O(1)$ order one. At large times, when the wave starts to displace, the view field is expanded to show that the asymptotic results are not able to reproduce the tangential velocity profile, remaining only the numerical one plotted.

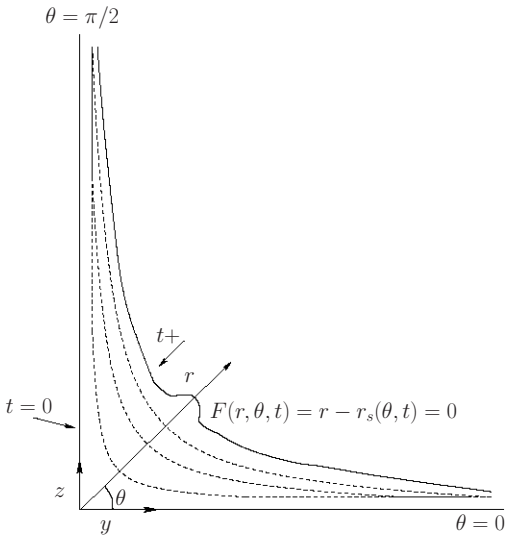

Figure 5.5: Sketch of the flow near the corner of the plate.

5.3 Flow structure near the corner at short times

In order to investigate the structure of the flow near the corner of the plate it is convenient to work with polar coordinates, (r, θ). Consider therefore, an inner region in the vicinity of the corner of the plate, $r = \sqrt{y^2 + z^2} \to 0$, for short times, $t \ll 1$, with the free surface function identified as $F = r - r_s(\theta, t) = 0$, as sketched in figure 5.5. In consequence, the original 2D+T system (5.1), reads

$$\begin{aligned} \nabla^2\phi &= 0 \\ \partial_t r_s + \partial_\theta r_s \frac{\partial_\theta \phi}{r_s^2} - \partial_r \phi &= 0 \\ \partial_t \phi + \frac{1}{2}((\partial_r \phi)^2 + \frac{(\partial_\theta \phi)^2}{r_s^2}) + r_s \sin\theta &= 0 \end{aligned} \tag{5.10}$$

Assuming that the corner wave is a local phenomenon near the corner point $(0, 0)$, the possibility of achieving a self-similar solution must be investigated. Notice that the self similar behavior of the flow near the corner must be of the second kind since, near the corner, the velocities depend on the hydrostatic pressure gradient, provided by Δh. This condition, as will be shown later, does not impose the exponents of the scaling, which will have to be adjusted by matching the outer region. Thus, we will look for solutions in the form

$$\begin{aligned} \phi(r, \theta, t) &= a(t)\varphi(\rho, \theta) \\ r &= b(t)\rho \\ r_s(\theta, t) &= b(t)\rho_s(\theta). \end{aligned} \tag{5.11}$$

Introducing the expressions (5.11) into the system (5.10), the boundary conditions now read:

$$\begin{aligned} \frac{\dot{b}b}{a}\rho_s + \partial_\theta \rho_s \partial_\theta \varphi - \partial_\rho \varphi = 0 \\ \dot{a}\varphi - \frac{\dot{b}a}{b}\rho_s \partial_\rho \varphi + \frac{1}{2}(\frac{a}{b})^2 \left((\partial_\rho \varphi)^2 + \frac{(\partial_\theta \varphi)^2}{\rho_s^2} \right) + b\rho_s \sin\theta = 0. \end{aligned} \tag{5.12}$$

The dynamic boundary condition of system (5.12), when is multiplied by $\frac{b^2}{a^2}$, turns into

$$\frac{\dot{a}b^2}{a^2}\varphi - \frac{\dot{b}b}{a}\rho_s \partial_\rho \varphi + \frac{1}{2}\left((\partial_\rho \varphi)^2 + \frac{(\partial_\theta \varphi)^2}{\rho_s^2} \right) + \frac{b^3}{a^2}\rho_s \sin\theta = 0, \tag{5.13}$$

in which the term $\frac{\dot{b}b}{a}$ will be denoted as λ, whereas $\frac{\dot{a}b^2}{a^2}$ will be denoted as μ.
Using now λ and μ, it is possible to sought solutions in the form

$$a(t) = t^\alpha \qquad\qquad b(t) = t^\beta, \tag{5.14}$$

and consequently, λ and μ are rewritten as:

$$\begin{aligned} \lambda &= \beta t^{2\beta-\alpha-1} \\ \mu &= \alpha t^{-1-\alpha+2\beta} \end{aligned} \tag{5.15}$$

Notice that solutions in form of power laws, are the only solutions that can fit the initial condition $\phi = 0$ when $t \to 0$. Introducing now the system (5.15) into (5.12), the boundary conditions then read:

$$\begin{aligned} \beta\rho_s + \frac{\dot{\rho_s}}{\rho_s^2}\partial_\theta \varphi - \partial_\rho \varphi = 0 \\ \alpha\varphi - \beta\rho_s \partial_\rho \varphi + \frac{1}{2}\left((\partial_\rho \varphi)^2 + \frac{(\partial_\theta \varphi)^2}{\rho_s^2} \right) + t^{\beta-\alpha+1}\rho_s \sin\theta = 0. \end{aligned} \tag{5.16}$$

where $\dot{\rho_s} = \partial_\theta \rho_s$.
It should be pointed out that, for the unsteady and convective terms to be of the same order in (5.16), the exponents α and β must satisfy,

$$2\beta - \alpha - 1 = 0, \tag{5.17}$$

coming out with the first condition needed to determine the exponents α and β. The second condition needed to determine the exponents, and thus the structure of the similarity solution, can be found imposing that, in the limit $\rho \to \infty$, the rescaled potential φ matches the double limit $r \to 0$ and $t \to 0$ of the original potential ϕ. In other words, when $t \to 0$,

$$\lim_{r\to 0} \phi_{out} = \lim_{\rho\to\infty} \phi_{in} = \lim_{\rho\to\infty} t^\alpha \varphi(\rho, \theta). \tag{5.18}$$

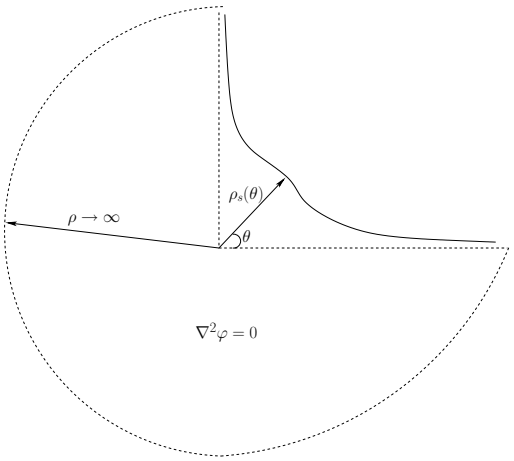

Figure 5.6: Sketch of the inner region of the corner flow.

Observe that the potential ϕ_{out} can be obtained in the limit $r \to 0$ of the solution of the first order of the Pressure Impulse Asymptotic analysis, $\phi_{out} = t\varphi_1$, which reads,

$$\lim_{r\to 0} \phi_{out} = t\varphi_1 + O(t^2) \approx t(Jr^{2/3} \sin\frac{2}{3}\theta - r\sin\theta) + O(tr^{4/3}), \tag{5.19}$$

where J is obtained as a part of the solution. An extensive analysis of the analytical form of φ_1 can be found in Appendix C.

Thus imposing the aforementioned matching solution between the leading order of ϕ and φ, when $\rho \gg 1$ and $t \ll 1$,

$$t^\alpha \varphi = t(Jt^{2\beta/3}\rho^{2/3} \sin\frac{2}{3}\theta - t^\beta \rho \sin\theta), \tag{5.20}$$

and, considering $t^\beta \ll t^{2\beta/3}$ the second condition to obtain the values of β and α becomes,

$$t^\alpha = t^{1+2\beta/3} \Longrightarrow 3\alpha - 2\beta - 3 = 0. \tag{5.21}$$

Connecting now the expressions 5.17 and 5.21, the values of α and β are,

$$\begin{cases} \alpha = 2 \\ \beta = 3/2. \end{cases} \tag{5.22}$$

Remarkably, the last term of the dynamic condition of system (5.16), the hydrostatic term in the Bernoulli equation near the corner, turns out to be negligible in the limit $t \ll 1$, since it scales with the time raised to the exponent $\beta - \alpha + 1 = 1/2$. This results means that, in the inner region, the gravity effects, which are the leading mechanism of the entire flow, disappear taking part in the solution, only as a condition in the matching with the outer potential.

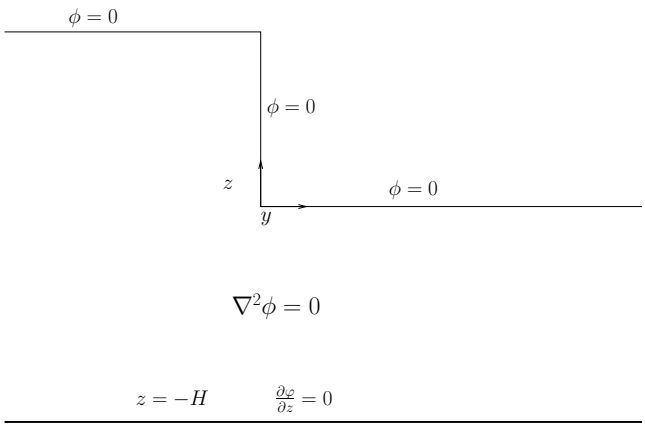

Figure 5.7: Sketch of the initial free surface used to check the self similar behavior of the corner wave.

To summarize, the self-similar solution valid near the corner at short times can be obtained solving the Laplace's equation for the rescaled self-similar potential, $\nabla^2\varphi = 0$, subject to the following boundary conditions at the free surface,

$$\begin{aligned} \frac{3}{2}\rho_s + \frac{\dot{\rho_s}}{\rho_s^2}\partial_\theta\varphi - \partial_\rho\varphi = 0 \\ 2\varphi - \frac{3}{2}\rho_s\partial_\rho\varphi + \frac{1}{2}\left((\partial_\rho\varphi)^2 + \frac{(\partial_\theta\varphi)^2}{\rho_s^2}\right) = 0, \end{aligned} \tag{5.23}$$

in the domain sketched in figure 5.6 and assuming that, the potential φ, when $\rho \to \infty$, tends to,

$$\varphi \to J\rho^{2/3}\sin\frac{2}{3}\theta \tag{5.24}$$

Rewriting system (5.11), with the out-coming values of α and β, the selfsimilar problem is expressed as,

$$\begin{aligned} \phi(r,\theta,t) &\sim t^2(J\rho^{2/3}\sin\frac{2\theta}{3}) \\ r &\sim t^{3/2}\rho \\ r_s(\theta,t) &\sim t^{3/2}\rho_s(\theta). \end{aligned} \tag{5.25}$$

To check the validity of the selfsimilar scaling (5.25), a series of cases, with the initial free surface, modeled as the sketched in figure 5.7, were solved for the complete problem. In these cases, a tempered radius of curvature R, was added to the corner points $(0,0)$ and $(0,1)$ in order to prevent numerical instabilities.

If we recall what was shown in section 5.2.2, where we used a BEM to validate the Pressure Impulse analysis, the evolution of the trajectory of the crest can be monitored

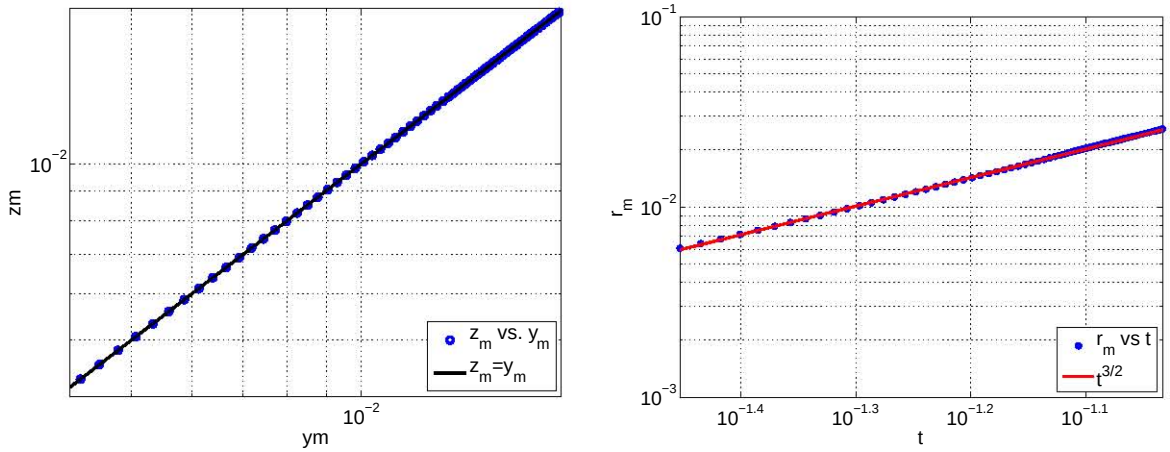

(a) (b)

Figure 5.8: Self-Similarity of the crest trajectories of the wave.(a) Vertical z_m trajectory of the crest as a function of its horizontal coordinate, y_m. (b) Dependence of both components of the trajectories, $r_m = \sqrt{y_m^2 + z_m^2}$, with time.

using the maximum of the normal velocity profile at each time. Therefore we can use such feature to check that the wave crest trajectory, $r_m = \sqrt{y_m^2 + z_m^2}$, follows the proposed time scaling, $r_s \sim r_m \sim t^{3/2}$.

Figure 5.8(a) shows the vertical, z_m, trajectory of the crest as a function of its horizontal coordinate, y_m, showing that, z_m is a linear function of y_m, $z_m \sim y_m$. This implies that both components of the trajectory follow the same power law. Notice that, there must exist a region for large values of time, where the trajectories begin to separate from the linear behavior. In that region, the crest of the wave starts to separate from the body of the free surface and begins the ballistic path explained in Chapter 3, in which the gravity terms are becoming more important.

Figure 5.8(b) shows the dependence of both components of the trajectories, $r_m = \sqrt{y_m^2 + z_m^2}$ with time. After a short time, in which the tempered radius of curvature at the corner, R, affects the trajectories, the crest of the wave is seen to follows precisely the proposed scaling of equation (5.25), $r_m \sim t^{3/2}$. This result confirms the self similar behavior of this flow for short times. On the other hand, in figure 5.9(a), one can observe that, when scaling the free surface profiles with $t^{3/2}$, the shape of the free surface profile remains invariant, thus backsliding in the self-similarity of the problem.

It must be pointed out that, due to the higher accelerations at that point, the crest evolves

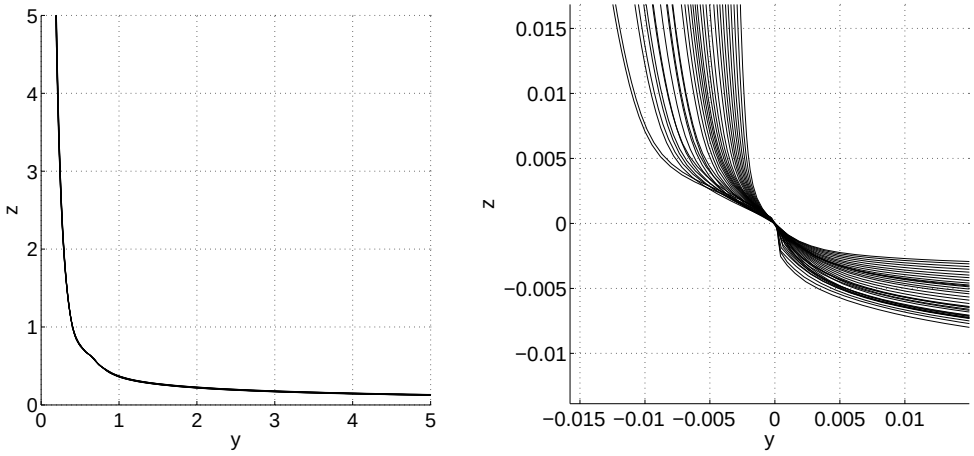

(a) (b)

Figure 5.9: (a) Self similar rescaled free surface profiles with $t^{3/2}$. The time range used in this figure is the same as in figure 5.8(b). (b) Free surface profile evolution translating the origin of coordinates at the crest of the wave. Notice that the free surface profiles are not equiespaced as the time step is not fixed (see section 4.3).

over time faster than the rest of the free surface, and therefore, faster than the initial self-similar solution. This is not a surprising fact since, as previously mentioned, the crest of the wave, when detaches from the rest of the free surface, follows a ballistics path, which implies that its time scale should range, over time, from $r_m \sim t^{3/2}$ to $r_m \sim t^2$.

Figure 5.9(b) shows the time evolution of the free surface translating the origin of coordinates at the crest of the wave at each time. As can be seen in this figure, the crest of the wave maintains its form as it evolves, and detaches, from the rest of the free surface.

It must be pointed out that, the selfsimilar solution does not predict any wave. This solution evolves smoothly the free surface from the corner until a certain curvature is attained. At that point, the corner wave rises up by the effect of such curvature, meaning, in our simulations, the tempered radius of curvature R or the vena contracta effect in the 3D case. The curvature near the origin, as was mentioned in section 5.2.1, behaves as a "hydrodynamic lens", concentrating the fluid particles towards a single point where, by conservation of mass, they cannot concur simultaneously and therefore, require an outlet in the form of a jet.

Other examples of such behavior are known to occur in axisymmetric standing waves when a jet arises out of a wave trough and in collapsing axisymmetric bubbles and cavities, Longuet-Higgins & Oguz (1997). In both examples studied by Longet-Higgins, the

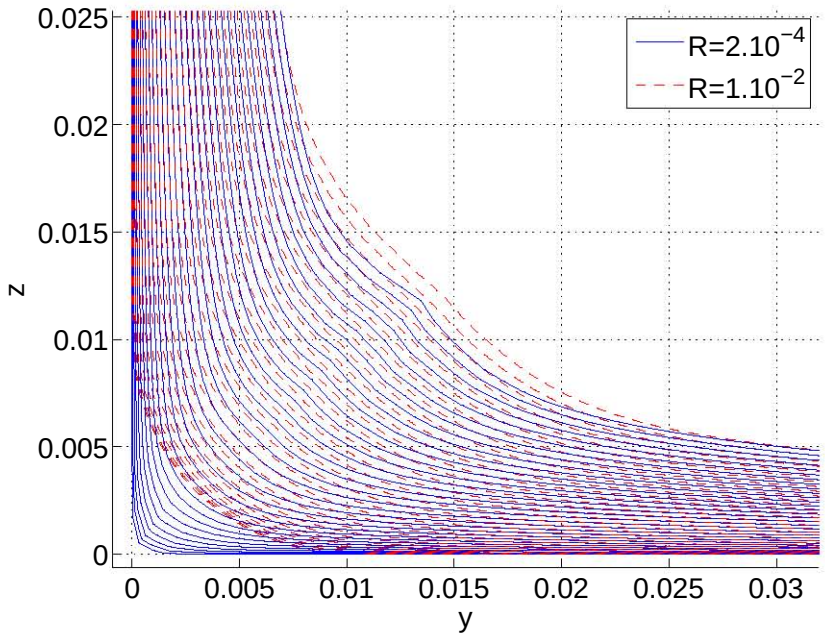

Figure 5.10: Effect of the finite curvature near the origin in the wave formation. The blue solid line represents the free surface evolution for $R = 2.10^{-4}$, whereas the red dash line corresponds to the case $R = 10^{-2}$.

acceleration of the formed jets shows to also follow a power-law dependence on the time. However, in absence of any complete analytical solution, the mentioned author, resorted to numerical solutions.

In Longuet-Higgins (2001), the author asserts that "high vertical accelerations and velocities can arise in the troughs of standing waves in deep water, particularly if the wave trough has a circular form. By conservation of mass, the particles directed towards the center cannot reach their destination simultaneously, and so require a vertical outlet in the form of a jet. Dynamically, the destruction of the horizontal momentum requires large horizontal pressure gradients, hence a high-pressure maximum at a point on the vertical plane of symmetry below the free surface. But the pressure at the surface itself remains a constant, by hypothesis. Hence there is a strong vertical pressure gradient, accelerating the particles near the surface vertically upwards."

Figure 5.10 shows the effect of the finite curvature near the origin, meaning, the tempered radius of curvature R in our simulations. In the mentioned figure, it can be appreciated that, at the same time, the steeper curvature produces higher accelerations in the particles that surround the vicinity of its maximum value, generating the jet faster that in the cases with smoother curvatures.

5.4 Initial free surface evolution

Once the self similar solution is attained, we can apply the knowledge of the outer potential, ϕ, to obtain the theoretical evolution of the free surface at short times. Recalling, the outer potential reads,

$$\phi = \varphi_1 t = t(Jr^{2/3}\sin\frac{2}{3}\theta - r\sin\theta). \tag{5.26}$$

As mentioned before, an extensive description of the analytical expression for the outer potential can be found in Appendix C.

Since the corner presents a singular solution, we will proceed to examine the evolution of the free surface on each one of the branches near the origin, $(y = 0, z \to 0)$ and $(z = 0, y \to 0)$. Beginning with the vertical branch, and using that $\theta = -3/2\pi$, its kinematic condition reads,

$$\partial_t y_s - \partial_z y_s - \frac{2}{3}Jtz^{-1/3} = 0, \tag{5.27}$$

where y_s is the free surface function of the mentioned branch in which $y \ll z$, $u_y = -u_\theta$ and $u_z = u_r$. Deriving equation (5.26), the velocities at that location read:

$$\begin{cases} u_y = -u_\theta = \frac{2}{3}Jtr^{-1/3} \quad \text{and, as} \quad z = 0, \quad u_y = \frac{2}{3}Jtz^{-1/3} \\ u_z = -1 \end{cases} \tag{5.28}$$

The p.d.e. (5.27) can be rewritten using the variables $\xi' = t + z$ and $\eta' = t$ yielding,

$$\partial_{\eta'} y_s - \frac{2}{3}J\eta'(\xi' - \eta')^{-1/3} = 0, \tag{5.29}$$

which general solution is given by,

$$\int_{y_s} dy_s = \frac{2}{3}J\int_{\eta'} \frac{\eta' d\eta'}{(\xi' - \eta')^{1/3)}} \to y_s = \frac{1}{5}J(5t + 3z)z^{2/3} + C(t + z). \tag{5.30}$$

Notice that since at $t = 0$, $y_s = 0$, the constant $C(z) = \frac{6}{5}J^{5/3}$ and,

$$y_s = \frac{6}{5}J^{5/3} + \frac{1}{5}J(5t + 3z)z^{2/3}. \tag{5.31}$$

On the other hand, in the horizontal branch $\theta = 0$, thus

$$\begin{cases} u_y = u_r = 0 \\ u_z = u_\theta = \frac{2}{3}Jtr^{-1/3} - t \quad \text{and, as} \quad y = 0, \quad u_y = \frac{2}{3}Jty^{-1/3} - t, \end{cases} \tag{5.32}$$

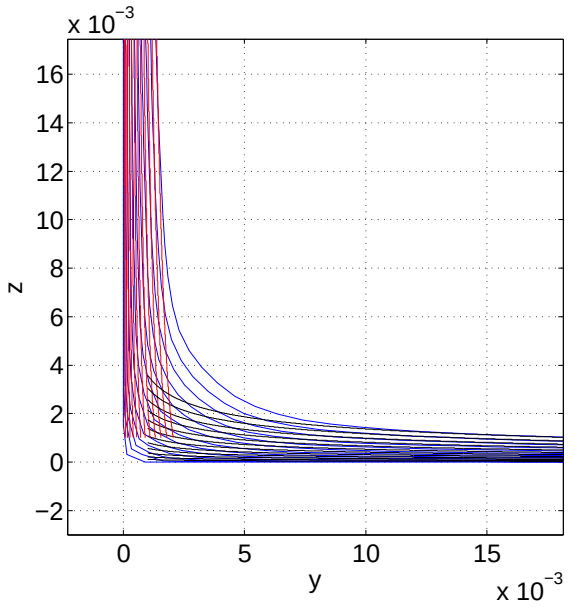

Figure 5.11: Free surface evolution of each branch of the free surface obtained using the velocity potential given by equation 5.26, in black and red, together with the results of the evolution of a numerical free surface obtained using a tempered free surface with $R = 5 \cdot 10^{-4}$, in blue.

and the kinematic condition for the horizontal branch of the free surface reads,

$$\partial_t z_s + u_y \partial_y z_s - u_z = 0 \quad \text{where } \partial_y z_s = 0, \text{ yielding,} \quad \partial_t z_s - u_z = 0. \tag{5.33}$$

Therefore, the equation that gives the time evolution of the horizontal branch becomes,

$$z_s = \int_t u_z(y,t)dt = t^2(\frac{1}{3}Jy^{-1/3} - \frac{1}{2}), \tag{5.34}$$

which satisfies the initial condition at $t = 0$.

Figure 5.11 shows the comparison between the predicted evolution of the free surface obtained using the velocity potential given by equation 5.26 together with the results of the evolution of a numerical free surface obtained using a tempered free surface with $R = 5 \cdot 10^{-4}$. Notice that there exists a region in which both branches cross at each time step. In this region, the free surface evolution can not be predicted.

Figure 5.12(a)-(b) shows a detailed view of the comparison between the predicted evolution of both branches of the free surface with the numerical one. As it can be observed, the agreement in the vertical branch lasts longer than in the horizontal one.

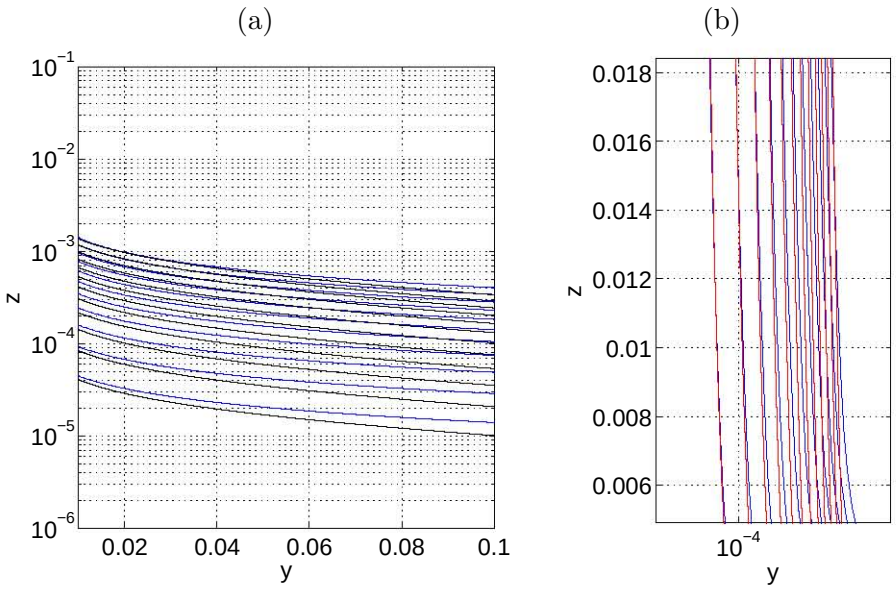

Figure 5.12: Detailed view of the comparison between the predicted evolution of both branches of the free surface with the numerical one. The predicted evolution of the free surface is plotted in black for the horizontal branch (a), whereas for the vertical branch is plotted in red (b). The numerical evolution of the free surface is plotted in blue.

5.5 Important Parameters in the corner wave formation

In this section we will assess which parameters can affect the corner wave formation and its initial development. In particular, we will focus in the parameters that may affect the results of the asymptotic outer solution given by equation (5.26), namely,

1. The distance H to the bottom.

2. The tempered radius of curvature R, used in the simulations.

3. The dimensionless width of the channel, $W_1 = W'/\Delta h$.

To quantify the influence of H in the corner wave formation and its repercussion in the future trajectories of the crest, a set of different cases varying the distance to the floor were processed.

As can be seen in Appendix C, the factor J, which multiplies the leading order of the asymptotic outer solution is directly related to H. Thus, it is quite revealing to see how J is affected by the different distances to the basin. Figure 5.13(a) shows the influence of H in the factor J. As expected, the depth has little effect on the solution near the corner.

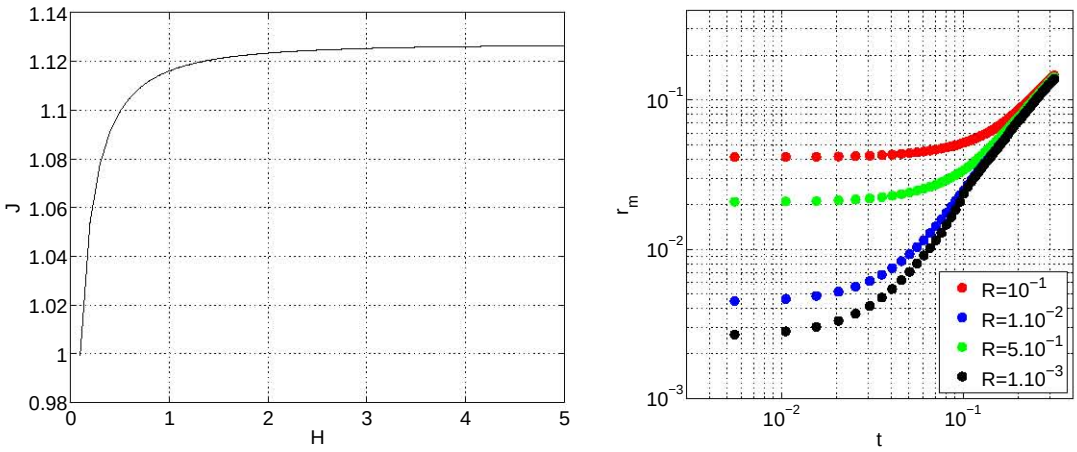

(a) (b)

Figure 5.13: Influence of the bottom depth and the initial curvature radius in the wave profiles. (a) Variations of J as a function of H. (b) Time evolution of crest trajectory as a function of the initial fillet R, at the corner.

In fact, J reaches an asymptote $J_\infty \simeq 1.125$ for $H \simeq 2$.

Figure 5.13(b) shows that the influence of R in the wave trajectory disappears as the time evolves and the wave develops. This later result can not be surprising when remembering that, as shown in Chapter 3, the wave trajectories are solely a function of the Froude number based in the maximum height difference, $Fr_{\Delta h}$. For this reason, considering $R \ll \Delta h$, the trajectories must remain invariant, after the necessary time has elapsed, when using the non dimensional variables proposed in Chapter 2.

Notice that, supporting the theory proposed for the formation mechanism of the wave in section 5.3, for short times, the fluid particles concur to the point of maximum curvature and form the wave faster in the cases with steeper curvature. In the cases with smooth curvature, the particles in that area experience less pronounced accelerations and, therefore, the jet forms later.

The effects of the dimensionless width of the channel, $W_1 = W'/\Delta h$, were characterized varying its value, while keeping $H = 2$, no producing any consequence in the initial velocity distribution when $W_1 \geq 5$.

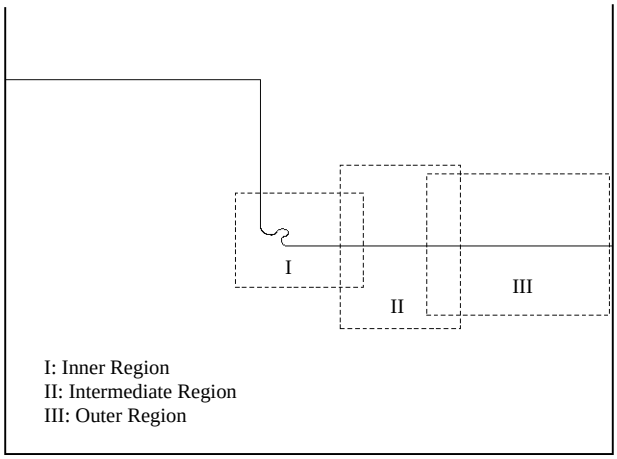

Figure 5.14: Sketch of the different regions of the flow. Notice that, if we assume the self-similar approach of section 5.3, the inner region must contain an inner-inner region of order $O(0)$, in which the potential goes as $\phi \sim \rho^{2/3}$.

5.6 Analysis of the far field of the free surface

In section 5.4, a novel expression for the outer potential near the corner was used. As can be seen in Appendix C, the achievement of this solution through the use of a conformal mapping involves a tremendous effort and can be hard to update in case of changes in the boundary conditions. However, there is an alternative method of treating the problem, instead of solving the boundary integral equation, which consists in separating the flow in three regions, as sketched in Figure 5.14. The first one, the nearest to the origin, is the inner region, in which the full problem (5.1) should be applied. Nevertheless, there exists another region far enough from the origin, the far field, in which the nonlinear terms diminish in importance and the problem can be simplified. Obviously, there must be an intermediate transition region to serve as a link between them.

In the far field, if we neglect the non-linear terms, the theory of gravity waves can be applied. The gravity wave theory asserts that, as separating from the origin, $\varsigma = y/t^2 \to \infty$, the nonlinear terms decays much faster than the gravitational ones. In this instance, it can be assumed that the local problem is equivalent to its gravity one counterpart,

$$\begin{aligned} \nabla^2\phi &= 0 \\ \partial_t\phi + h &= 0 \\ \partial_t h - \partial_z\phi &= 0, \end{aligned} \tag{5.35}$$

where the free surface function is defined as $F(y,z) = z - h = 0$, with $\phi(t=0) = 0$.

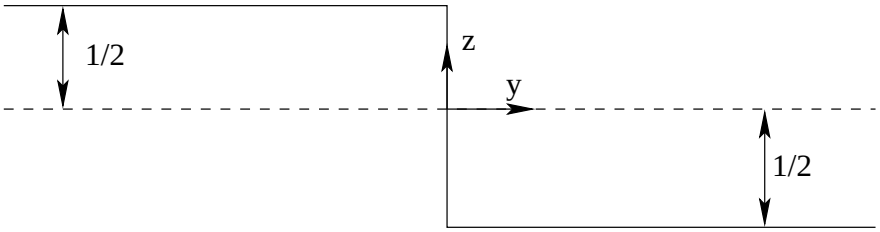

Figure 5.15: Sketch of the initial free surface with a translation of the origin of coordinates in order to take advantage of the symmetry of the problem

In order to take advantage of the symmetry of the problem, the free surface h can be defined as $h = \frac{1}{2} - H(y)$, by translating the coordinate origin. In fact, the scroll of the origin of coordinates identifies the initial free surface profile with a heavystep function, $H(y)$, as shown in figure 5.15.

System (5.35) can be solved using Fourier's functions, applied in the y direction:

$$-k^2\tilde{\phi} + \tilde{\phi}_{zz} = 0 \rightarrow \tilde{\phi} = F(k,t)e^{kz} + G(k,t)e^{-kz} \tag{5.36}$$

where $G(k) = 0, k > 0$ and $F(k) = 0, k < 0$, since $\tilde{\phi} \rightarrow 0$ when $z \rightarrow -\infty$. Observe that, due to the symmetry of the problem $|G| = |F|$. Introducing equation (5.36), into the boundary conditions of system (5.35), and forcing $k > 0$, we obtain:

$$\begin{aligned} \partial_t F + \tilde{h} &= 0 \\ \partial_t \tilde{h} - kF &= 0, \end{aligned} \tag{5.37}$$

that can be reduced into:

$$\partial_{tt}\tilde{h} + k\tilde{h} = 0, \tag{5.38}$$

returning

$$\begin{aligned} \tilde{h}(t=0) &= F^{-1}[\frac{1}{2} - H(y)] = \frac{i}{k} \\ F(t=0) &= \frac{1}{k}\partial_t \tilde{h} = 0 \end{aligned} \tag{5.39}$$

and therefore, a free surface function of the form,

$$\tilde{h} \sim \cos(\sqrt{k}t). \tag{5.40}$$

Obviously, looking at (5.40), $\tilde{h}$ must be real to have a physical meaning. Consequently we must impose that $\tilde{h}(k,t)$ must be odd in all times. Therefore, the kinematic condition

reads

$$\partial_t \tilde{h} + kG = 0 \rightarrow G = -\frac{1}{k}\partial_t \tilde{h}(k,t) = -\frac{1}{k}\partial_t(\tilde{-h}(-k,t)) = \\ = -\frac{1}{-k}\partial_t \tilde{h}(-k,t) = -\frac{1}{|k|}\partial_t \tilde{h}(|k|,t) = F. \tag{5.41}$$

Undoing the transformation, the free surface function h is determined by,

$$h = \frac{i}{2\pi}\int_{-\infty}^{\infty} \frac{\cos(\sqrt{k}t)}{k} e^{iky} dk = \frac{i}{2\pi} 2i \int_0^{\infty} \frac{\cos(\sqrt{k}t)\sin(kt)}{k} dk = \\ = \frac{-1}{\pi}\int_0^{\infty} \frac{\cos(\sqrt{k}t)\sin(kt)}{k} dk, \tag{5.42}$$

which, when setting, $kt^2 \rightarrow k$ and $yt^{-2} \rightarrow \varsigma$, turns into:

$$h = \frac{-1}{\pi}\int_0^{\infty} \frac{\cos(\sqrt{k})\sin(k\varsigma)}{k} dk. \tag{5.43}$$

Notice that integral (5.43) has an exact solution,

$$h = \frac{1}{2} + C^2(\frac{1}{\sqrt{2\pi\varsigma}}) + S^2(\frac{1}{\sqrt{2\pi\varsigma}}) \tag{5.44}$$

where the terms C and S are Fresnel's integrals, (Abramowitz & Stegun (1964), pg 301) and, from the same source:

$$\varsigma \rightarrow \infty : C \sim (\frac{1}{\sqrt{2\pi\varsigma}}) + o(\varsigma^{-5/2}) \\ S \sim \frac{\pi}{A}(\frac{1}{\sqrt{2\pi\varsigma}})^3 \sim \varsigma^{-3/2} \tag{5.45}$$

Hence, the asymptotic behavior of the free surface in the far field is given by,

$$h \sim \frac{-1}{2} + \frac{1}{2\pi\varsigma}. \tag{5.46}$$

Figure 5.16 shows the agreement between the original free surface obtained using the initial 2D+T system of equations (5.1), rescaled using t^2, and the tendency proposed by equation (5.46), $h \sim \frac{1}{2\pi\varsigma}$. In the far field, it can be appreciated that the rescaled free surface follows the above mentioned tendency but is separated from the asymptotic behavior as we approach to $y < 0.1$.

Figure 5.17 shows that the divergent tendency between both solutions appears when $h \sim \frac{1}{2}(\partial_n \phi)^2$, caused mainly for the incoming importance of the non-linear terms, which for these values of y cannot be neglected any more. This result reinforces the theory of the existence of an intermediate region which separates the far field from the full non-linear region near the corner point $(0,0)$. A properly defined system of equations for the

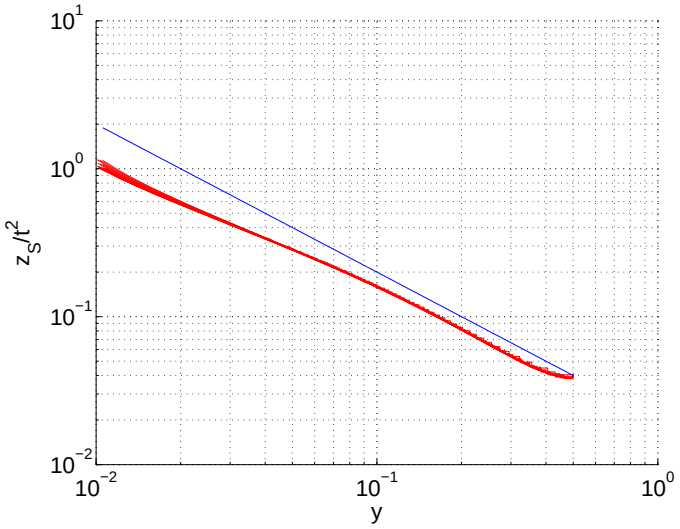

Figure 5.16: Scaling of h obtained using the equation (5.46) for $(0.01 < y < 1)$. The blue line, plotted together, represents the function $\frac{1}{2\pi\varsigma}$, whereas the red one is the rescaled original solution.

intermediate region must include, therefore, the non-linear terms, as i.e.

$$\begin{aligned} \nabla^2\phi &= 0 \\ \partial_t\phi + \frac{1}{2}|\partial_z\phi|^2 + h &= 0 \\ \partial_t h - \partial_z\phi &= 0. \end{aligned} \tag{5.47}$$

The proposed far field solution for the free surface function can also be used to predict the far field tendency for the velocity potential. Applying now, the same Fourier analysis to ϕ instead of h and, using $\varsigma = y/t^2$, the potential can be written as,

$$\phi = \frac{-t}{\pi}\int_0^\infty \frac{\sin(\sqrt{\alpha})\sin(\alpha\varsigma)}{\sqrt{\alpha^3}}d\alpha \tag{5.48}$$

which, using again the Fresnel integrals proposed in Abramowitz & Stegun (1964), pg 301, becomes,

$$\begin{aligned} \phi = \frac{-t}{\pi} + t[-2\sqrt{\frac{2\varsigma}{\pi}}\sin(\frac{1}{4\varsigma})C(\frac{1}{\sqrt{2\pi\varsigma}}) + \sqrt{\frac{2\varsigma}{\pi}}\cos(\frac{1}{4\varsigma})S(\frac{1}{\sqrt{2\pi\varsigma}}) + ... \\ C^2(\frac{1}{\sqrt{2\pi\varsigma}}) + S^2(\frac{1}{\sqrt{2\pi\varsigma}})] \simeq \\ \frac{-t}{2} + t[\frac{2}{\pi}\sqrt{2\pi\varsigma}(-\sin(\frac{1}{4\varsigma})C(\frac{1}{\sqrt{2\pi\varsigma}}) + \cos(\frac{1}{4\varsigma})S(\frac{1}{\sqrt{2\pi\varsigma}})) + ... \\ C^2(\frac{1}{\sqrt{2\pi\varsigma}}) + S^2(\frac{1}{\sqrt{2\pi\varsigma}})] \simeq \\ \frac{-t}{2} + t[\frac{2}{\pi}\sqrt{2\pi\varsigma}(\frac{-1}{4\varsigma}\frac{1}{\sqrt{2\pi\varsigma}}) + \frac{1}{\sqrt{2\pi\varsigma}} + o(\varsigma^3)] \simeq \frac{t}{6\pi\varsigma}, \end{aligned} \tag{5.49}$$

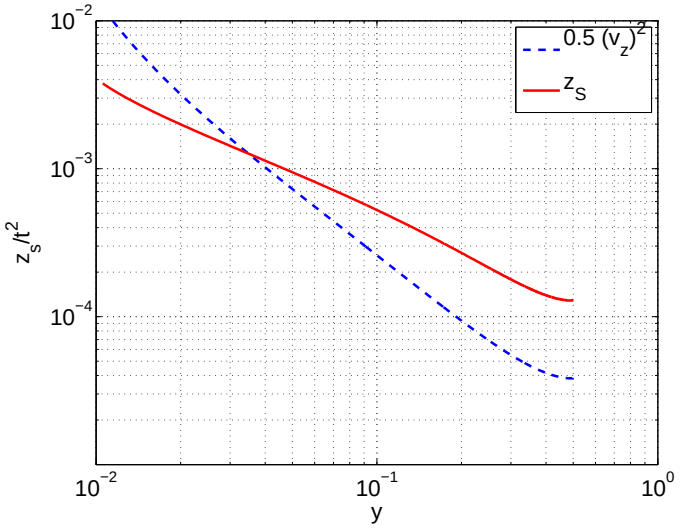

Figure 5.17: In red, the scaling of h obtained using the equation (5.46) for $(0.01 < y < 1)$ and compared, in blue, with the non-linear terms $\frac{1}{2}U_n^2$. In this figure, it can be seen that the non-linear terms become important as approaching to the coordinate origin, suggesting the existence of an intermediate region between the far field and inner region.

meaning consequently that the tendency for the potential is,

$$\phi \sim \frac{-t^3}{y}. \tag{5.50}$$

5.7 Concluding Remarks

In this chapter the hidden physics of the formation and initial development of a corner wave have been investigated. With this purpose, a Pressure-Impulse asymptotic analysis has been formulated and validated showing that, for short times, the first order of the impulse solution agrees fairly well with the original problem, extending the applicability of the analysis when including the $O(t^2)$ order terms.

The self similar behavior of the initial free surface evolution was investigated in an inner region of the flow in which the free surface was assumed to evolve as $r_s \sim t^{3/2}$. Numerical results showed a good agreement with the proposed time scaling law.

The first order of the velocity potential, φ_1, in the vicinity of the corner of the plate, for short times, was found to disagree with the one proposed in the potential flow theory around a right solid angle, $\varphi_1 = r^{2/3} \sin \frac{2}{3}\theta$, revealing that, in the case of which the boundaries are subject to changing conditions, as the dynamic and kinematic ones in a

free surface, an extra term, $-r\sin\theta$, should be added, thus reading

$$\varphi_1 = Jr^{2/3}\sin\frac{2}{3}\theta - r\sin\theta + O(r^{4/3}). \tag{5.51}$$

Using equation (5.51), the free surface was evolved finding a good agreement at short times with the one obtained using a BEM.

The influence on the solution of the distance of the plate to the basin, H, the initial curvature near the corner, R, and the width of the channel, W_1, was investigated.

Finally, the far field of the flow was analyzed finding that gravity waves theory can be applied to this region, given that, as separating from the origin, the nonlinear terms diminish in importance.

CHAPTER
SIX

Conclusions

The wave originated at the corner of a partially submerged vertical flat plate has been studied using a combination of experimental, numerical and theoretical tools. The conclusions can be classified attending to the techniques that have been used to obtain them:

Conclusions of the experimental study:

- The formation and initial development of the wave are nearly unaffected by the presence of the walls and bottom of the channel, even when their distances to the corner, where the wave originates, are of the order of the wave amplitude. This suggests that the formation of the wave is a local phenomenon, in the sense that it only depends on the structure of the flow field near the corner.

- Therefore, the main dimensionless parameter affecting the initial stages in the evolution of the corner wave is the Froude number, based on the available water height upstream the plate, Δh.

- The amplitude of the corner wave increases as the wave evolves downstream until it eventually breaks giving birth to either a spilling or plunging breaker. A systematic study has been performed to determine the transition criterion that separates both flow configuration in the space of dimensionless parameters. It has been observed that the transition nearly occurs when the ratio between the available water height above the corner, Δh, and the contraction of the free surface due to the *vena contracta* effect, δ, adopts a value of about $\Delta h/\delta \approx 3$, although the exact value has been seen to depend slightly on the Froude number based on δ, Fr_g . More specifically, when the height ratio $\Delta h/\delta$ exceeds the critical value, a plunging breaker is observed.

- In those configurations where a plunging breaker is formed, the resulting plunging jet has been seen to follow a ballistic trajectory, as is the case in time-evolving two-dimensional plunging breakers.

Conclusions of the theoretical/numerical study:

- The large values of both the Froude and Reynolds numbers allow the application of the so-called 2D+T approximation. This simplification allows the transformation of a three dimensional steady flow into a two dimensional time-evolving one.
- The resulting two-dimensional unsteady problem has been solved numerically using a boundary element method. The numerical results reproduce fairly well the formation of the wave, except for the *vena contracta* mentioned above, that is a genuine three-dimensional effect.
- A pressure-impulse asymptotic analysis has been performed to obtain the evolution of the wave at very short times. This technique accurately describes the initial stages in the formation of the wave.
- It has been shown that the flow near a sharp corner at short times has a self-similar structure. More exactly, the flow exhibits a similarity solution of the second kind. In other words, the scaling exponents of the velocity potential and the free surface cannot be determined solely by examining the structure of the flow near the corner. On the contrary, these exponents must be obtained imposing that the outer limit of the self-similar solution matches the inner limit of the pressure-impulse asymptotic solution near the corner.
- From the physical point of view, the occurrence of a similarity solution of the second kind rather than of the first kind can be explained taking into account that the order of magnitude of the velocity near the corner must depend on the available water height, which is a feature of the global flow configuration.
- Although it is not directly related to the formation of the wave, the flow field far away from the corner, and downstream the plate, has been analytically obtained using the gravity waves theory.

APPENDIX
A

Future Work

In this dissertation a classic fluid mechanics problem, the corner wave flow, has been presented and the physics involved in its formation have been unveiled. However, this flow is just the entrance door to many others problems as i.e:

- The estimation of the air entrainment in the ocean due to plunging breakers in the wake of high speed vessels.
- More realistic modeling of the the structure of the wake generated by high-speed vessels.
- The complete understanding of the rooster tail dynamics and the physics which form and evolve the divergent waves.

To analyze the feasibility of the research lines proposed above, this chapter presents some outcomes of the preliminary work done on these lines by the author.

A.1 Air Entrainment

The steadiness of the corner wave provides an excellent opportunity of obtaining detailed measurements of the ingested air at the splash region in plunging breakers. The possibility of consider a steady splash region, hard to achieve in other experiments, is a motivation to contemplate the mentioned flow as a powerful tool to study such process. The special configuration of the corner wave does not only provides the above mentioned steadiness but also, allows the monitoring and the tracking of the generated bubble cloud. The deep knowledge and understanding of the motion mechanics of the bubble cloud after a splash process is a critical phenomenon that acquires huge importance not only in oceanography but also in sonar applications. Additionally, as explained by Clanet & Lasheras (1997), the size and deep of penetration of the bubble cloud provides good information of the jet impingement process.

Figure A.1, shows a side view of a typical plunging corner corner wave together with an instantaneous zoom of the splash region. As can be observed in the mentioned figure, this

Figure A.1: (a) Side view of a typical plunging corner wave. (b) A detail of an instantaneous view of the bubble cloud ingested by the jet impingement of the plunging breaker. The impingement region is marked in figure (a) as a circle.

flow configuration provides an excellent opportunity to experimentally track and measure the evolution of the ingested air after a splash.

A.2 Realistic Models

The selection of a plate to generate the corner wave instead of using a more complex object, reduces the number of parameters of the problem, i.e, we can neglect the boundary layer at the hull's bottom. However, in order to approach to reality, a set of experiments using a dummy ship model must be done. The possibility of obtain a similar flow than the corner wave by using a dummy model was tested, as shown in figure A.2. To reconstruct the free surface downstream the model, LIF experiments, identical of the ones described in 3, were performed. Figure A.3 shows that, in this case, there can also be found a corner wave structure.

An important benefit of working with a dummy ship model is that due to the absence of a recirculating region, as the one found upstream from plate, the stream lines below the model can be directed using the form of the underbody. In consequence, the *vena contracta* effect disappears, facilitating both numerical and experimental advances.

The advantages of using dummy ship models are wide, as i.e. in terms of the possibilities of the location of the experimental instrumentation. However, detailed calculations of the slenderness ratio of the model should be accomplished to prevent undesirable separations of the flow in the sides. Future research in this topic include a parametric study

(a) (b)

Figure A.2: (a) Lateral and (b) top view of the flow field downstream a dummy ship model. It can be appreciated in both figures that the flows resembles the one studied in this PhD dissertation in absence of the *vena contracta* effect.

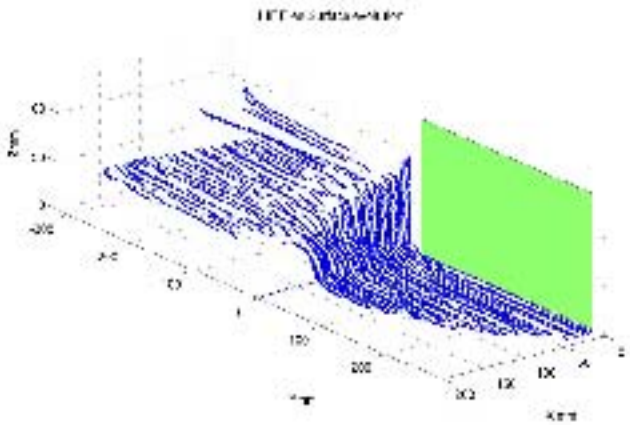

Figure A.3: LIF results of the free surface location downstream from a dummy ship model.

of the geometry of the model and the rest of the parameters reported in the corner wave flow to allow furthers comparisons with real ship models.

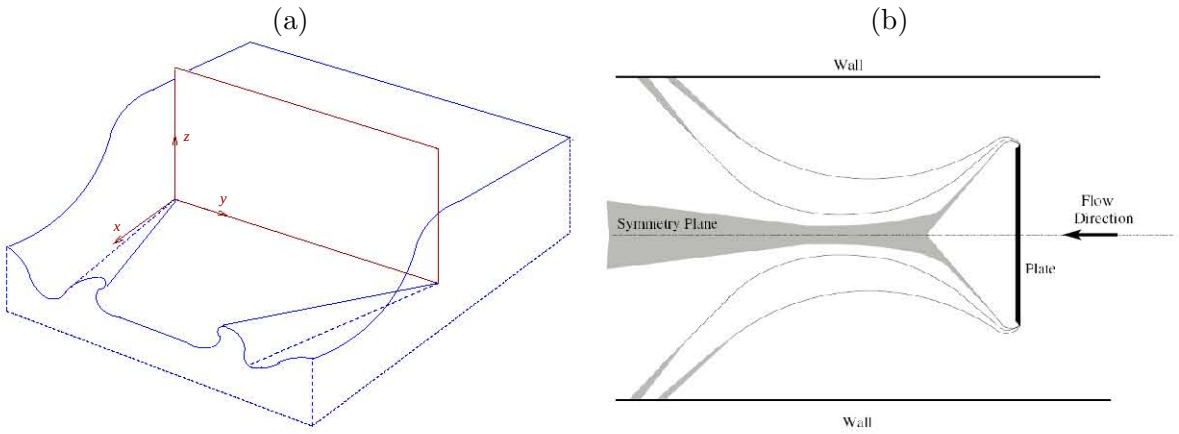

Figure A.4: Sketch of the flow set-up used to generate divergent waves. (a) General view. (b) Top view.

A.3 Divergent Wave & Rooster Tail

It is well known that the rooster tail is responsible for a big amount of the air entrainment in the wakes of high speed vessels. Nevertheless, at the same time, there exists another important contribution to the atmosphere-sea air exchange by the, so-called, divergent wave.

The divergent waves are formed due to the depression, or valley, originated by the advance of the corner wave which, at the point of the raising of the rooster tail, produces sudden jumps in the elevation of the free surface. This difference in height in the free surface gives birth to a wave in the opposite direction to the corner wave one. Usually, the above mentioned waves are denominated divergent waves.

Both, the rooster tail and the divergent wave, can be reproduced in a recirculating water channel taking into account that the experimental set-up must allow the formation of two corner waves, one on each side of the plate, needed to form the rooster tail. The set up should also provide enough distance from the rooster tail to the walls with the aim of granting the propagation of the divergent waves. This experiment can be done using a plate similar to that used in the flow reported in this dissertation but, placing it in the center of the test section. As mentioned above, the location of the plate has to contemplate that a couple of corner waves, one for each *wet corner*, will appear, colliding downstream from the plate in the middle of the wake. A sketch of this configuration is shown in figure A.4.

The divergent wave and the rooster tail can be numerically simulated in a similar way

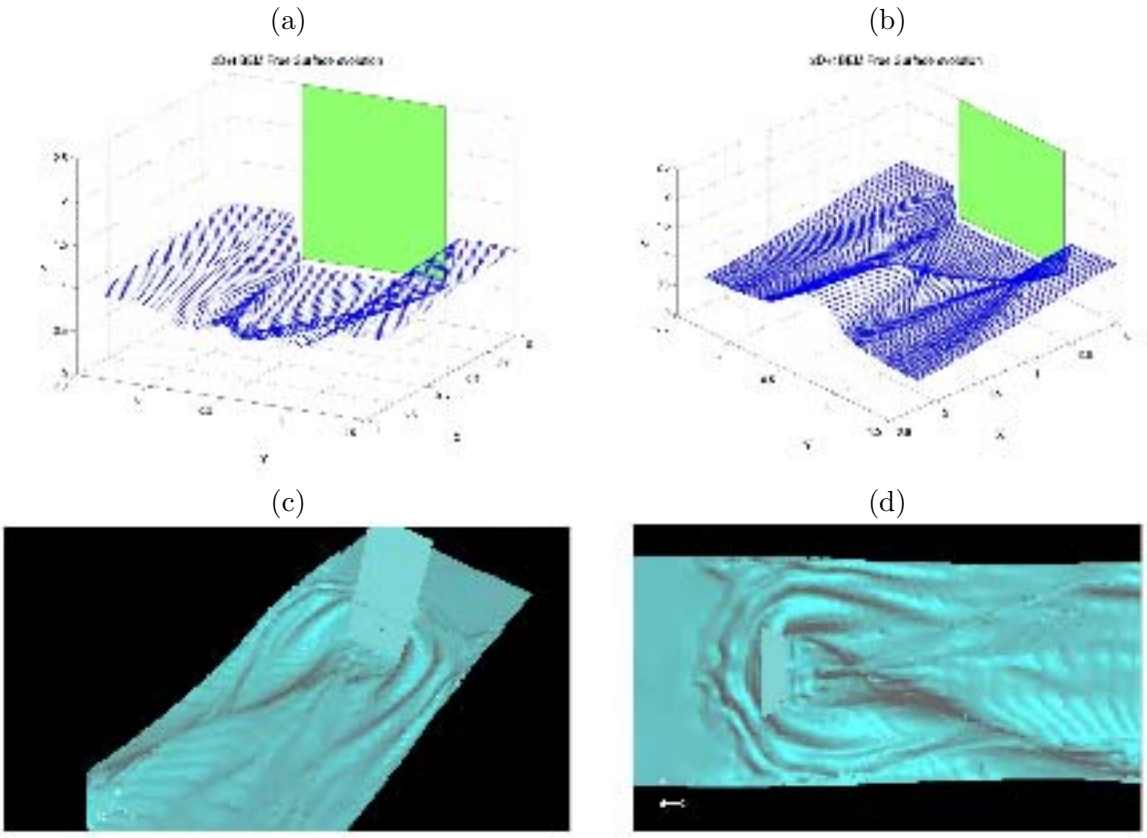

Figure A.5: Numerical results of the flow by placing the plate in the center of the test section of the channel. (a) and (b) shows calculations obtained using boundary element method. (c) and (d) use volume of fluid method to capture the free surface. In (b), (c) and (d) the rooster tail and the divergent wave can be clearly appreciated.

to the one used to model the corner wave and, attending to the desired information, a BEM or a VOF method, can be selected. Figure A.5 shows the free surface location of the divergent wave and the rooster tail, using both methods, implemented in the same way that in the corner wave one (see chapter 4).

The free surface location used to initialize both calculations was directly measured using a LIF experiment for a canonical case of the divergent wave by placing a plate of width $W = 0.3$ in the middle of the test section. The initial upstream velocity profile, necessary implement the VOF, was measured using a Pitot tube far upstream from the plate, to ensure that the velocity profile remains uniform. Detailed measurements of the velocity profile upstream the plates are reported in Appendix B.

Figure A.6 shows the ability of the VOF method capturing the free surface compared with experimental results obtained using image processing tools. It can be appreciated

(a) (b)

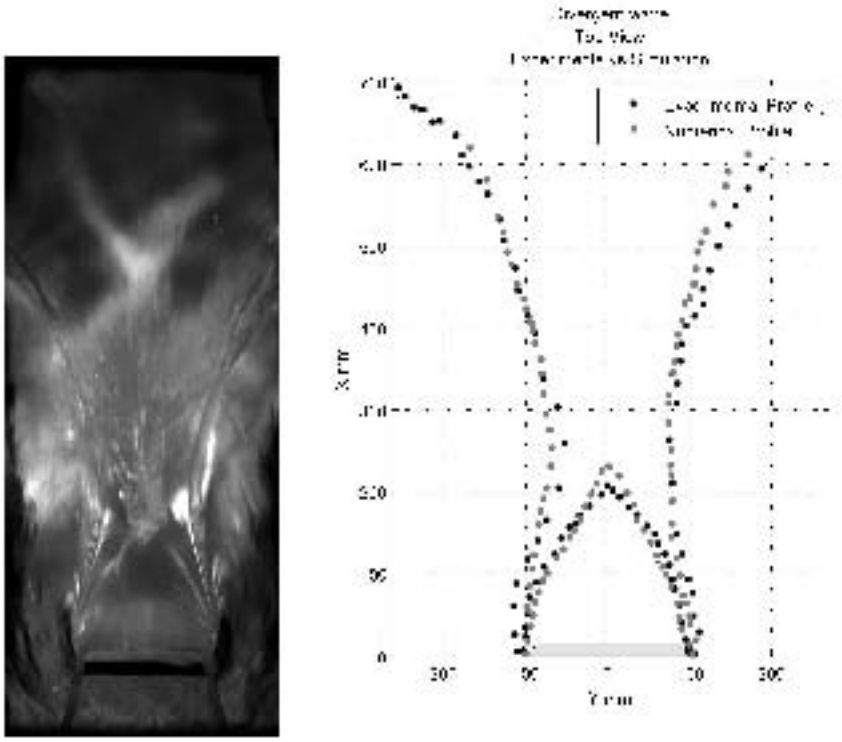

Figure A.6: (a) Experimental determination of the divergent wave location. (b) Comparison between the experimental free surface location of a divergent wave and the numerical predicted one, using the VOF method.

that, even for such complex flows, the VOF method is able to capture the free surface location with an adequate accuracy. However, more work is needed to be done in this problem to understand the rooster tail and the divergent wave dynamics.

APPENDIX
B

Velocity measurement in the corner wave flow

This appendix gathers the experimental measures of the velocity field in the corner wave obtained with particle image velocimetry.

B.1 Particle Image Velocimetry (PIV)

Particle image velocimetry (PIV) is an optical method of flow visualization used in education and research. PIV systems measure whole velocity fields by determining a particle displacement over a precisely selected time using a double-pulsed laser technique. A laser light sheet illuminates a plane in the flow, and the positions of particles, which are assumed to faithfully follow the flow dynamics (naturally present or added to the flow to have sufficient number of scatterers), in that plane, are recorded using a digital camera. A short time (micro or milliseconds) later, a second pulse illuminates the same plane, creating a second set of particle images. From these sets of images, unique PIV analysis algorithms obtain the particle displacements for the imaged region, to give the velocity information at thousands of locations-quickly, easily and reliably. Flow properties such as vorticity and strain rates are obtained for the entire region. Mean velocity, turbulence intensity, and higher order statistics are also obtained.

To set-up a typical PIV experiment, the following components are used; a digital CCD camera, a double-pulsed Nd:YAG twin lasers, an articulated arm, the properly optical arrangement and a synchronizer.

The synchronizer controls the timing between image exposures in the camera and also permits image pairs to be acquired at various times along the flow. For accurate PIV analysis, it is ideal that the region of the flow of interest displays an average particle displacement of about 8 pixels. This is a compromise between a longer time spacing, which would allow the particles to travel further between frames, making it harder to identify which interrogation window corresponds to which point, and a shorter time spacing, which could make it overly difficult to identify any displacement within the flow.

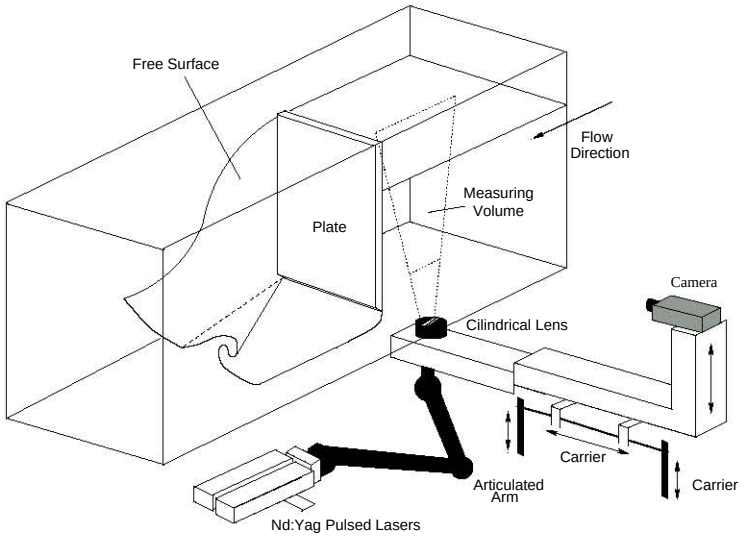

Figure B.1: Sketch of Particle image velocimetry (PIV) set-up in the $(x' - z')$ plane.

Once the images are acquired, the frames are split into a large number of interrogation areas, or windows. It is then possible to calculate a displacement vector for each window with help of signal processing and autocorrelation or cross-correlation techniques. This displacement is converted to a velocity using the time between laser shots and the physical size of each pixel on the camera. The size of the interrogation window should be chosen to have at least 6 particles per window on average.

This technique was used to obtain the velocity field at the corner wave. The goal was to characterize completely the flow field upstream and near the plate and, if were possible, obtain detailed measurements of the velocity field inside the corner wave. The first objective was accomplished, however, the strong curvature of the free surface of the wave generates light reflections, which made impossible to obtain good measurements of the velocity within the wave without damaging the equipment.

B.1.1 PIV set up

The PIV measurements in the corner wave were performed in two planes, $(x' - z')$ and $(x' - y')$. To that end, as sketched in figure B.1, for the $(x' - z')$ plane, the laser beam, generated by the double-pulsed Nd:YAG twin laser, was conducted to the bottom of the channel by an articulated arm and aligned in the vertical direction. To convert the laser beam into a sheet, a combination of cylindrical and spherical lens were attached to the head of the articulated arm, which was mounted in a traverse. To capture the motion of the seeding particles, a CCD camera, mounted in the same traverse, was used. The camera is a Kodak Megaplus 1.0 ES with a resolution of 1008×1010 pixels together with a NIKON lens of 60mm of focal distance and 1.5 f.

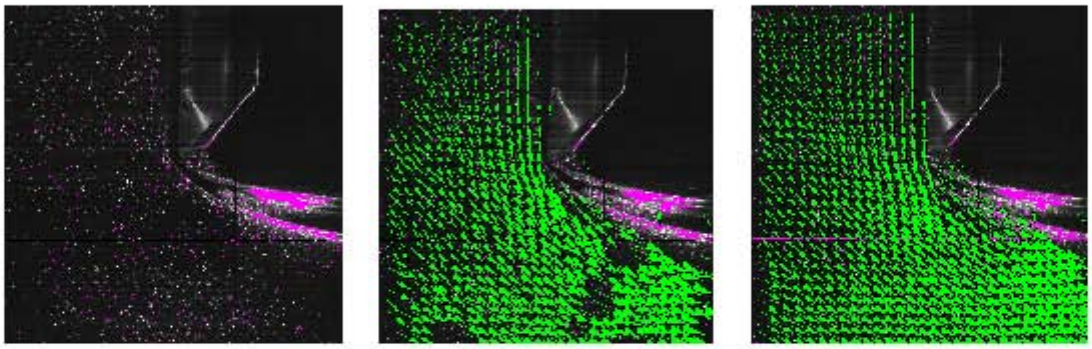

(a) (b) (c)

Figure B.2: Three images of the PIV process. (a) Typical acquisition image with the tracer bubbles illuminated by the laser sheet. (b) Initial velocity vectors obtained by the Insight software in first approximation. (c) Complete velocity field interpolated with Insight.

After taking a calibration image, using a grid attached to a plate submerged in the channel, the laser sheet and the camera, placed in the same traverse, were moved together in the y' direction to cover the widest range possible of the domain. Measurements in the $(x' - y')$ plane were obtained in the same way, but placing the camera in the position where the head of the articulated arm was located in the previous case and vice versa.

The tracer particles used in this experiment were hydrogen bubbles with a typical diameter of 20-30 μm. The use of these particles is always very attractive given the high scatering that generate when are crossed by the laser sheet. The non-neutral buoyancy of the hydrogen bubbles can be a disadvantage, but when working with large Froude and Reynolds numbers, as those found in this flow, the bubbles precisely follow the stream lines, being a reasonable suitable tracer particles. The hydrogen bubbles were generated using water electrolysis, which was produced by placing a cathode far upstream the measurement region and an anode at enough distance downstream. The quantity and size of the bubbles was regulated by using a variable DC source with a potentiometer.

The Nd:YAG twin lasers, of 50 mJ/pulse, and the articulated arm, were part of a TSI PIV all-in-one system. To synchronize the firing of the lasers and the camera trigger, a LASERPULSE Synchronizer (Model 610034) was used, and the time delay between the laser pulses fixed in 10 ns. This high temporal resolution, coupled with the short pulse width in the laser (5 ns), makes the system ideal for measurements in this kind of flows.

At the moment of the firing of the lasers two consecutive images, recording the light

Range	$(x' - z')$ plane	$(x' - y')$ plane
x'_{min} (mm)	-220	-165
x'_{max} (mm)	75	15
y'_{min} (mm)	-240	-100
y'_{max} (mm)	240	80
z'_{min} (mm)	-150	-125
z'_{max} (mm)	-75	85

Table B.1: Range of the PIV measurement regions.

scattered by the tracer particles, were captured with the CCD camera. The images were taken 0.4 milliseconds apart, corresponding to the firing of each laser.

Once the images were squired, the software Insight (TSI Inc., Saint Paul,MN) was used to compute the velocity field using interrogation windows of 64×64 pixels size, and interpolated over the rest of the image, as shown in figure B.2.

Two canonical cases, one for the case of a plunging breaker and one for the case of a spilling breaker, reported in Chapter 3 as cases A and B, were studied. For each one of the cases, the 3D flow field around the plate was reconstructed doing two different sets of PIV measurements one in the $(x' - z')$ plane and other in the $(x' - y')$ plane.

In the $(x' - z')$ set, 49 planes were taken for each case, from $y = -24$ cm to $y' = 24$ cm in a 1 cm step size. To increase the range of the measurement, the traverse was also moved along the streamwise direction. In the $(x' - y')$ set, 40 planes were taken, from $z' = -125$ cm to $z' = 85$ cm in a 1 cm step size. Table B.1 contains a resume of the complete range of the measurements.

Figure B.3 shows two typical streamwise velocity profiles for each one of the $(x' - y')$ and $(x' - z')$ planes in the plunging breaker corresponding to case A. It must be pointed out that, coinciding with Roth & Hager (1999), the velocity profile remains uniform upstream the plate.

The velocity field obtained using this technique, was implemented in the Volume of Fluid method, as the initial condition for the velocity in the simulations reported in Chapter 4.

(a)

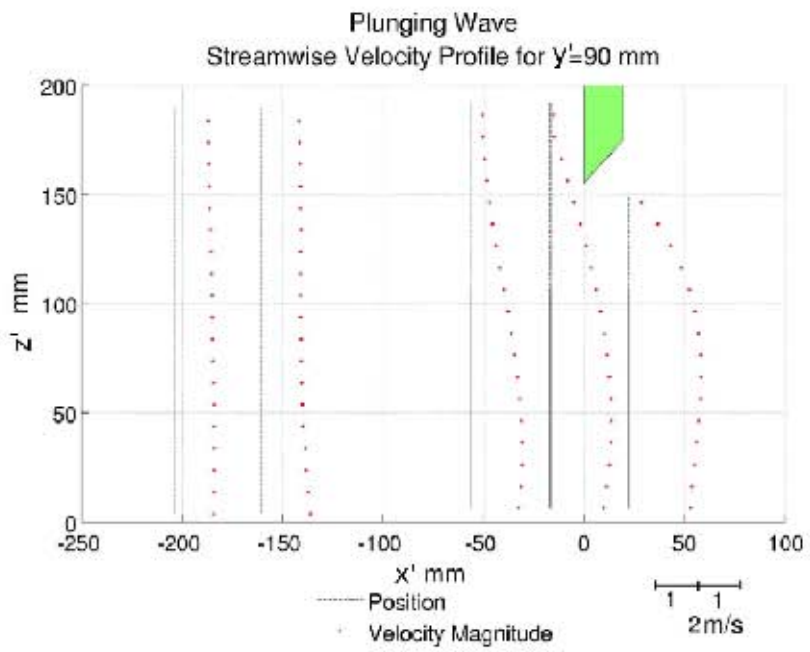

(b)

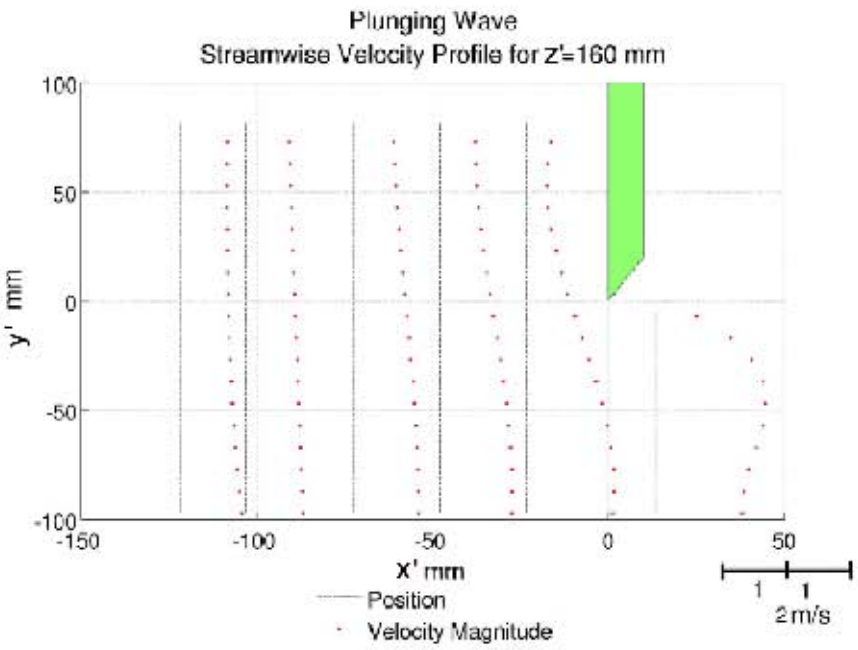

Figure B.3: Results of the streamwise velocity upstream and near the plate using PIV. (a) Typical streamwise velocity field in the $(x' - z')$ plane for a plunging breaker. (b) $(x' - y')$ plane.

APPENDIX
C

The Outer Solution

In this appendix, an analytical expression for the velocity potential of the corner wave is presented. To obtain such expression, the potential will be analyzed in the entire domain and not only near the corner of the plate.

C.1 Introduction

Consider, to begin, the vicinity of the corner of the plate at short times, as sketched in figure 5.5 with the free surface function identified as F. For this flow configuration, as proposed in Batchelor (1967) (sec 6.5), and considering that the liquid angle is $\frac{3}{2}\pi$, the velocity potential can be written as,

$$\phi = r^{2/3} \sin \frac{2}{3}\theta, \tag{C.1}$$

where $r = \sqrt{y^2 + z^2}$ and $\theta = \arctan \frac{z}{y}$. The assumption of equation (C.1), imposes that the potential goes as $\phi \sim r^{2/3}$ meaning consequently that the initial velocities near the corner, are identical,

$$\begin{aligned} \theta = 0 \rightarrow u_{n,y} &= -\frac{1}{r}\frac{\partial \phi}{\partial \theta}|_{\theta=0} = -\frac{2}{3} r^{-1/3} \\ \theta = \frac{3\pi}{2} \rightarrow u_{n,z} &= \frac{1}{r}\frac{\partial \phi}{\partial \theta}|_{\theta=\frac{3\pi}{2}} = -\frac{2}{3} r^{-1/3} \end{aligned} \tag{C.2}$$

Following the velocities proposed in (C.2), it becomes clear that, approaching to the origin, both branches of the free surface, $(y = 0, z \rightarrow 0)$ and $(z = 0, y \rightarrow 0)$, should evolve equally on time. Therefore, it should be expected that the corner wave appears at a fixed angle of $\simeq 45°$. However, when looking to the simulations presented in Chapters 4 and 5, such tendency can only be confirmed for very short times.

The reason of such disagreement between the predicted evolution of the corner wave, near the corner point $(0, 0)$, and the one proposed by the potential (C.1) is not easy to be understood. Possible error sources are;

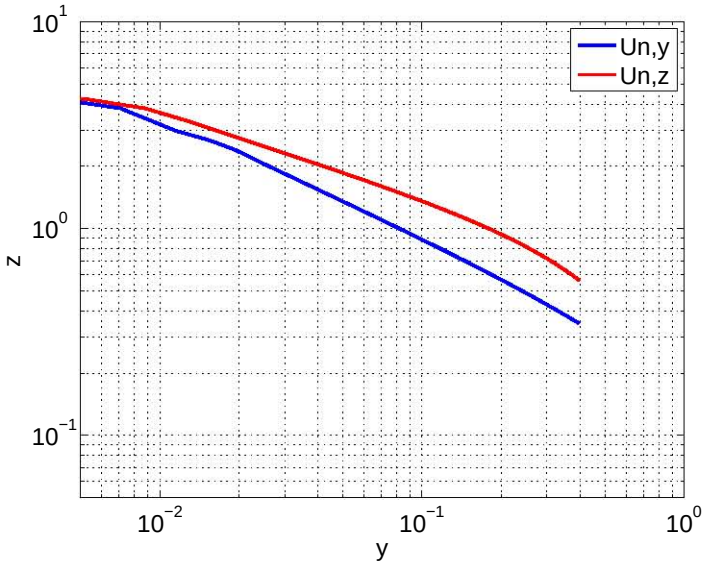

Figure C.1: Normal velocities of each branch of the free surface ($y = 0, z \to 0$) and ($z = 0, y \to 0$) near the corner.

- The necessity of including smoothed initial free surfaces profiles in the BEM code, in order to avoid numerical instabilities, with the subsequent loss of precision near the corner point.
- The possible influence of the rest of the flow field in the form of the potential. Figure C.1 shows that, for each branch of the free surface near the origin ($y = 0, z \to 0$) and ($z = 0, y \to 0$), the normal velocities evolve with different power laws, which would limit the application of equation (C.1) to a inner region, closer to the corner point.

To investigate the possible influence of the rest of the flow in the inner region, the leading order of the pressure impulse asymptotic analysis, exposed in Chapter 5, was studied.
In order to obtain a solution for the potential, φ_1, the domain sketched in figure C.2 was considered together with the following boundary conditions,

$$\varphi_1 = \begin{cases} -1 & \text{if } z = 1 \text{ and } y < 0, \\ -z & \text{if } y = 0, \\ 0 & \text{if } z = 0 \text{ and } y > 0, \\ \partial_{\vec{n}}\varphi_1 = 0 & \text{at } z = -H. \end{cases} \tag{C.3}$$

At this point, a finite element method (FEM) was used to solve the Laplace's equation, $\nabla^2\varphi_1 = 0$, with the boundary conditions (C.3). To implement the FEM method, the

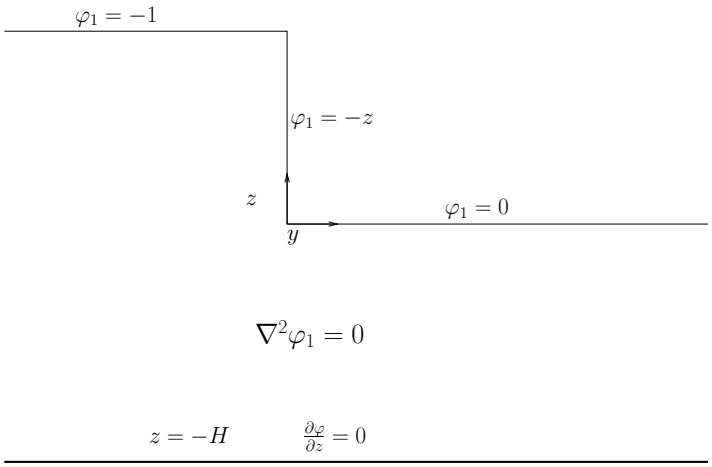

Figure C.2: Boundary conditions for the leading order of the potential, $\phi = \varphi_1$, using the P-I asymptotic expansion.

MATLAB pde toolbox using an adaptive mesh, was used. The adaptive grid was obtained by reducing the triangles of the original mesh at the locations where the largest values of the potential, after solving the Laplace's equation, $\nabla^2\varphi_1 = 0$, were found.

Figure C.3(a) shows the FEM solution for the potential near the corner. Once calculated, the solution of the potential was interpolated over an structured grid, of 2000 and 5000 points, near $y, z = 0$, for post-processing. The post-processing revealed that the grid convergence was excellent, obtaining residuals in the value of the potential of order $O(10^{-8})$. Finally, the gradient of the potential was calculated and extrapolated to the free surface, obtaining the normal velocity in each one of the branches.

Figure C.3(b) shows that, even approaching, using the FEM, closer to the corner point than with the BEM, both branches of the normal velocity still differ than the predicted by equation C.1. The good agreement between the results of the BEM and the FEM for the normal velocities of both branches of the free surface near the origin, suggest that the analytical form of the potential must be reexamined for the corner wave flow.
To accomplish this challenge, the Laplace's problem for the leading order of the potential φ_1, with the boundary conditions (C.3), is solved through an analytically study of the boundary integral equation,

$$\varphi_1(\vec{x_0}) = -\frac{1}{\pi}\int_{w,s}^{PV} \frac{\vec{x} - \vec{x_0}}{r^2} \cdot \vec{n}\varphi_1(\vec{x})dl(\vec{x}) + \frac{1}{\pi}\int_s \ln r \cdot \partial_{\vec{n}}\varphi_1 dl(\vec{x}). \tag{C.4}$$

Equation (C.4), presents improper integrals when solved in the physical plane so, it is analyzed by using a transformation to the complex plane; a conformal mapping.

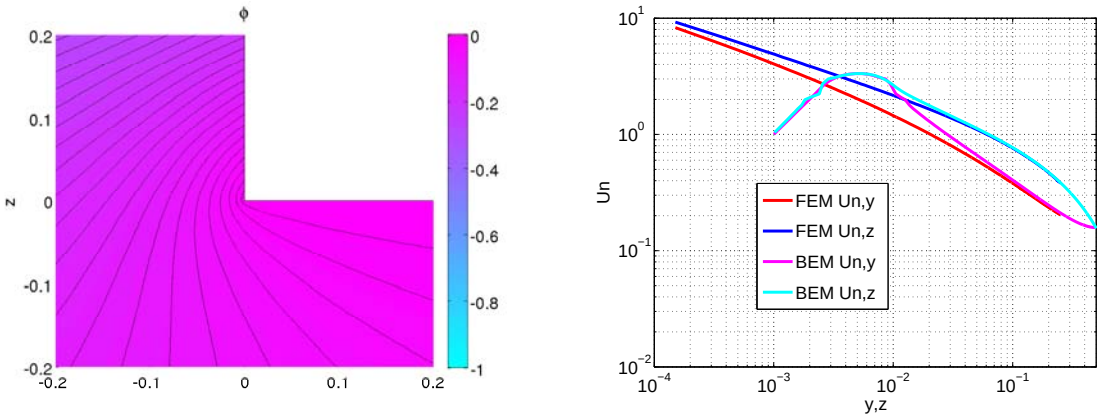

(a) (b)

Figure C.3: (a) Adaptive grid used in the FEM method. (b) Solution of the potential φ_1, near the corner, using the FEM method with an adaptive mesh.

C.2 The conformal mapping transformations

Potential flow, by the use of transformations to the complex plane in two dimensions, can be described using conformal mapping. The basic idea is to use an analytic function f, which maps the physical domain (y, z) to the transformed domain (φ', ψ'). While y, z, φ' and ψ' are all real valued, it is convenient to define the complex quantities,

$$z' = y + iz, \text{and} \qquad \mathrm{w} = \varphi' + \mathrm{i}\psi'. \tag{C.5}$$

Then, writing the mapping f as

$$f(y + iz) = \varphi' + i\psi', \qquad \text{or} \qquad \mathrm{f(z')} = \mathrm{w}. \tag{C.6}$$

Assuming now that f is a holomorphic function, the Cauchy-Riemann equation should be fulfilled,

$$\frac{\partial \varphi'}{\partial y} = \frac{\partial \psi'}{\partial z}, \qquad \frac{\partial \varphi'}{\partial z} = -\frac{\partial \psi'}{\partial y}, \tag{C.7}$$

and, based on this hypothesis it is clear that the velocity components (v, w), in the (y, z) directions respectively in the real plane read,

$$\frac{df}{dz'} = v - iw \tag{C.8}$$

Therefore, the velocity field $\vec{v} = (v, w)$ is given by

$$v = \frac{\partial \varphi'}{\partial y} = \frac{\partial \psi'}{\partial z}, \qquad w = \frac{\partial \varphi'}{\partial z} = -\frac{\partial \psi'}{\partial y}. \tag{C.9}$$

Both φ' and ψ' then satisfy Laplace's equation:

$$\Delta\varphi' = \frac{\partial^2\varphi'}{\partial y^2} + \frac{\partial^2\varphi'}{\partial z^2} = 0 \qquad \text{and} \qquad \Delta\psi' = \frac{\partial^2\psi'}{\partial \mathrm{y}^2} + \frac{\partial^2\psi'}{\partial \mathrm{z}^2} = 0, \tag{C.10}$$

in which, φ' can be identified as the velocity potential and ψ' is the stream function.

It is clear that any differentiable function may be used for f, including multi-valued functions such as the natural logarithm, must be confined to a single Riemann surface. In case of using a function f in power law, conformal map is applied, from $z' = y + iz$ to $w = \varphi' + i\psi'$:

$$w = Az'^n \tag{C.11}$$

which, when writing z' in polar coordinates as $z' = y + iz = r^{ei}\theta$, returns

$$\varphi' = Ar^n \sin n\theta, \qquad \text{and} \qquad \psi' = \mathrm{Ar^n} \cos \mathrm{n}\theta. \tag{C.12}$$

In particular, as explained in Batchelor (1967) (p.409), the exponent $n = 2/3$ corresponds to the flow around a right corner, as the one studied in this dissertation. However, as shown before, the certainty that the two branches of the normal velocity near the origin differ from the theory proposed by equation (C.1), $\phi \sim r^{2/3}$, advances that this theory remains only valid when the right angle is formed by the boundaries of a solid, loosing its validity if the fluid is surrounded by moving boundaries subject to changes.

For this reason the Schwartz-Christoffel mapping will be applied to the problem under consideration. Such transfomarion uses the conformal mapping theory, explained above, to transform a polygon in the physical plane, W, to a straight line in the complex plane, ξ, being suitable for the considered flow.

C.3 Schwartz-Christoffel Mapping in the corner wave

To applied the Schwartz-Christoffel transformation to the domain of the corner wave, Ω, each one of the corners of the polygon formed by the boundaries of the problem should be numerated sequentially in counterclockwise sense, and the exterior angles α_i computed, based in the previous and next face. These angles are bounded, $-\pi < \alpha_i < \pi$, considering that, when a corner of the polygon is pointing to the exterior of the domain, α becomes positive, while negative otherwise. For example, for the domain Ω, the corner point $(0, 1)$ returns an angle $\alpha_2 = \pi/2$ whereas the point $(0, 0)$ yields $\alpha_3 = -\pi/2 = 3\pi/2$. Obviously, regardless of form of the polygon, the sum of all angles must be equal to 2π.

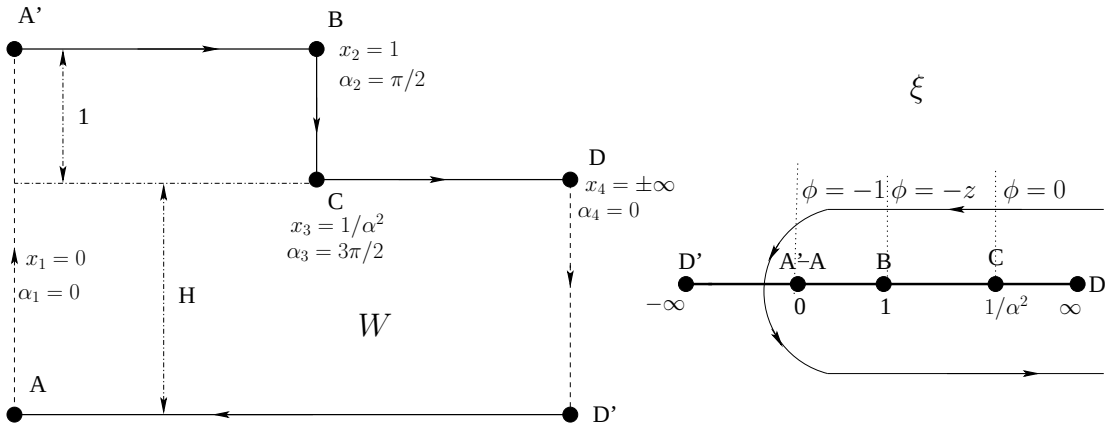

Figure C.4: Mapping the interior of the domain Ω, in the physical plane W, to the horizontal axis in the complex plane, ξ.

As explained i.e. by Pozrikidis (1997), the inverse mapping function of the domain Ω, in the physical plane W, can be obtained by integrating the following expression:

$$\frac{dW}{d\xi} = k\frac{(\xi - 1/\alpha^2)^{1/2}}{\xi(\xi-1)^{1/2}} \tag{C.13}$$

Returning:

$$W = i + \frac{1+H}{\pi}[\alpha \arg\cosh(\frac{\alpha^2 + 1 - 2\alpha^2\xi}{1-\alpha^2}) - \arg\cosh(\frac{2/\xi - \alpha^2 - 1}{1-\alpha^2})], \tag{C.14}$$

as sketched in figure C.4. Notice that it is permissible to set $\xi_1 = -\infty$ or $\xi_N = \infty$, in which cases, the corresponding factors in the integration are omitted. Observe also, that the boundary condition $\phi = -z$, in the vertical branch near $(0,0)$, is now a function of ξ, $-z = -f(\xi)$, reading:

$$z = 1 - \frac{1+H}{\pi} i[\alpha \arg\cosh(\frac{\alpha^2 + 1 - 2\alpha^2\xi}{1-\alpha^2}) - \arg\cosh(\frac{2/\xi - \alpha^2 - 1}{1-\alpha^2})] = f(\xi). \tag{C.15}$$

Once in the complex plane, and with the new boundary conditions, the potential at any point can be solved by using the boundary integral equation in its conservative form,

$$\int_s (\phi \nabla f(\xi) - f(\xi)\nabla\phi) \cdot \vec{n} ds = 0. \tag{C.16}$$

The expressions of the integrals which appear in (C.16), using the domain ξ as shown in figure C.4, are quite difficult to solve but this disadvantage can be over-passed by doing a transformation of the complex domain defining $\xi = \tau^2$ which would return a new complex plane, τ, sketched in Figure C.5.

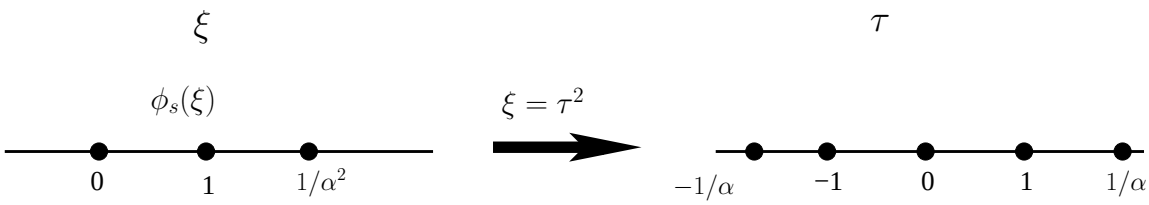

Figure C.5: The conformal mapping domain doing the transformation $\xi = \tau^2$.

It must be pointed out that the above transformation guarantees that the potential mantains $\partial_n\phi|_{\theta=\pi} = 0$ in the $[Re[\xi] < 0, \quad Im[\xi] = 0]$ axis of the ξ plane.

Applying equation (C.16), and using Sobolev (2005)'s book, the solution for the potential in the τ plane, where $\tau = \tau_{y0} + i\tau_{z0}$, becomes,

$$\phi(\tau_{y0},\tau_{z0}) = \frac{1}{\pi}\int_{-1/\alpha}^{1/\alpha}\phi(\tau_{y0},0)\frac{\partial}{\partial_{\tau_z}}(log(\frac{1}{r}))d\tau_y = \quad \text{(C.17)}$$

$$\frac{1}{\pi}\int_{-1/\alpha}^{1/\alpha} -\frac{\tau_z-\tau_{z0}}{(\tau_y-\tau_{y0})^2+\tau_{z0}^2}\phi(\tau_{y0},0)d\tau_y = \frac{\tau_{z0}}{\pi}\int_{-1/\alpha}^{1/\alpha} -\frac{\phi(\tau_{y0},0)}{(\tau_y-\tau_{y0})^2+\tau_{z0}^2}d\tau_y =$$

$$\frac{\tau_{z0}}{\pi}\int_{-1}^{1}\frac{-d\tau_y}{(\tau_y-\tau_{y0})^2+\tau_{z0}^2} + \frac{\tau_{z0}}{\pi}\int_{-1/\alpha}^{-1}\frac{-d\tau_y}{(\tau_y-\tau_{y0})^2+\tau_{z0}^2}\phi(\tau_{y0},0)+$$

$$\frac{\tau_{z0}}{\pi}\int_{1}^{1/\alpha}\frac{d\tau_y}{(\tau_y-\tau_{y0})^2+\tau_{z0}^2}\phi(\tau_{y0},0).$$

As it is shown, the potential in expression (C.17), can be split into three integrals $\phi = \phi_I + \phi_{II} + \phi_{III}$ in which ϕ_I has an exact solution that yields a first contribution to the potential,

$$\phi_I(\tau_{y0},\tau_{z0}) = \frac{-1}{\pi}\left[\arctan\frac{1-\tau_{y0}}{\tau_{z0}} + \arctan\frac{1+\tau_{y0}}{\tau_{z0}}\right], \quad \text{(C.18)}$$

which represents the solution of the boundary integral equation at the free surface. Notice that, the other two integrals, ϕ_{II} and ϕ_{III}, appear as the contribution from the distribution $\phi = -z$ along the boundary segment $[y = 0, 0 \geq z \geq -1]$.
To calculate an expression for integrals ϕ_{II} and ϕ_{III}, it is useful to rewrite equation (C.15) as,

$$z = 1 - \frac{1+H}{\pi}i\left[\alpha\arg|\cosh(\cos\theta_1)| - \arg|\cosh(\cos\theta_2)|\right] = 1 - \frac{1+H}{\pi}i[\alpha\theta_1 - \theta_2]i, \quad \text{(C.19)}$$

which results in

$$z = 1 + \frac{1+H}{\pi}[\alpha\theta_1 - \theta_2]. \quad \text{(C.20)}$$

Heed that, the circumstance that the arguments of the cosh vary between -1 an 1, when $1 \leq \xi \leq 1/\alpha^2$, have been used to simplify equation (C.19), in which $\arg|\cosh(\cos\theta_i)| = \theta_i i$.

Applying now the potential value in the interval $[-1/\alpha, -1]$, $\phi(0, \tau_{z0}) = -z(\tau_{z0})$, the contributions to the potential ϕ_{II} and ϕ_{III}, can be assembled into a simple expression $F(\tau_{y0}, \tau_{z0})$, whereby $\phi_2 = \phi_{II} + \phi_{III} = \frac{-\tau_{z0}}{\pi} \cdot F(\tau_{y0}, \tau_{z0})$, with,

$$F(\tau_{y0}, \tau_{z0}) = \int_{-1/\alpha}^{-1} \frac{-z(\tau_y)}{(\tau_y - \tau_{y0})^2 + \tau_{z0}^2} d\tau_y + \int_{1}^{1/\alpha} \frac{-z(\tau_y)}{(\tau_y - \tau_{y0})^2 + \tau_{z0}^2} d\tau_y, \tag{C.21}$$

in which $z(\tau_y)$ is the z-coordinate in the physical plane W. Using now that $z(\tau)$ is an even function, $z(\tau) = z(-\tau)$, as long as $\xi = \tau^2$, equation (C.21) can be cleaned up,

$$\begin{aligned} F(\tau_{y0}, \tau_{z0}) &= \int_{-1/\alpha}^{-1} \frac{-z(\tau_y)}{(\tau_y - \tau_{y0})^2 + \tau_{z0}^2} d\tau_y + \int_{1}^{1/\alpha} \frac{-z(\tau_y)}{(\tau_y - \tau_{y0})^2 + \tau_{z0}^2} d\tau_y, \\ &= \int_{1/\alpha}^{1} \frac{-z(\tau_y)}{(\tau_y - \tau_{y0})^2 + \tau_{z0}^2} - d(-\tau_y) + \int_{1}^{1/\alpha} \frac{-z(\tau_y)}{(\tau_y - \tau_{y0})^2 + \tau_{z0}^2} d\tau_y = \\ &= \int_{1}^{1/\alpha} \left[\frac{-z(\tau_y)}{(\tau_y - \tau_{y0})^2 + \tau_{z0}^2} + \frac{-z(\tau_y)}{(\tau_y + \tau_{y0})^2 + \tau_{z0}^2} \right] d\tau_y, \end{aligned} \tag{C.22}$$

and, the potential $\phi(\tau_0)$ can be now rewritten as $\phi(\tau_0) = \phi_I(\tau_0) + \phi_2(\tau_0)$, meaning:

$$\begin{aligned} \phi(\tau_0) = \frac{-1}{\pi} \left[\arctan \frac{1 - \tau_{y0}}{\tau_{z0}} + \arctan \frac{1 + \tau_{y0}}{\tau_{z0}} \right] \\ + \frac{\tau_{z0}}{\pi} \int_{1}^{1/\alpha} z(\tau_y) \left[\frac{1}{(\tau_y - \tau_{y0})^2 + \tau_{z0}^2} + \frac{1}{(\tau_y + \tau_{y0})^2 + \tau_{z0}^2} \right] d\tau_y, \end{aligned} \tag{C.23}$$

with the above mentioned parameters:

$$\begin{cases} z = 1 + \frac{1+H}{\pi}[\alpha\theta_1 - \theta_2)] \quad ; \quad \alpha = \frac{1}{1+H} \\ \theta_1 = \arccos(\frac{\alpha^2+1-2\alpha^2\tau^2}{1-\alpha^2}) \quad ; \quad \theta_2 = \arccos(\frac{2/\tau^2-\alpha^2-1}{1-\alpha^2}) \end{cases} \tag{C.24}$$

C.4 The potential near the origin

Now that it has been found an expression that describes the potential in the plane τ (equation (C.23)), it can be assessed its value in the vicinity of the origin. Notice that, the origin of the physical plane W corresponds to $\tau = \pm 1/\alpha$ and thus, near the corner point, the expression can be linearized in polar coordinates using,

$$\tau_0 = 1/\alpha + Pe^{i\gamma} \quad , \quad P \ll 1 \tag{C.25}$$

$$\tau_{y0} = 1/\alpha + P\cos\gamma \quad , \quad \tau_{z0} = P\sin\gamma \tag{C.26}$$

Inserting now expressions (C.26), into the piecewise-constant part of equation (C.23), it becomes:

$$\phi_I = \frac{-1}{\pi}\left[\arctan\frac{1-1/\alpha-P\cos\gamma}{P\sin\gamma}+\arctan\frac{1+1/\alpha+P\cos\gamma}{P\sin\gamma}\right]= \tag{C.27}$$
$$\frac{-1}{\pi}\left[\arctan(\frac{1-1/\alpha}{P\sin\gamma}-\cot\gamma)+\arctan(\frac{1+1/\alpha}{P\sin\gamma}+\cot\gamma)\right],$$

which assuming that $1/\alpha \ll 1$, turns into:

$$\phi_I = \frac{-1}{\pi}\left[-\arctan(\frac{1/\alpha-1}{P\sin\gamma}+\cot\gamma)+\arctan(\frac{1+1/\alpha}{P\sin\gamma}+\cot\gamma)\right]. \tag{C.28}$$

Equation (C.28), is described by Abramowitz & Stegun (1964)(eq. 4.4.28), and can be rewritten as,

$$\phi_I = \frac{-1}{\pi}\left[\frac{-i}{2}\log(\frac{i+\cot\gamma+\frac{1/\alpha-1}{P\sin\gamma}}{i-\cot\gamma-\frac{1/\alpha-1}{P\sin\gamma}})+\frac{i}{2}\log(\frac{i+\cot\gamma+\frac{1/\alpha+1}{P\sin\gamma}}{i-\cot\gamma-\frac{1/\alpha+1}{P\sin\gamma}})\right]= \tag{C.29}$$
$$\frac{i}{2\pi}\left[\log(\frac{1/\alpha-1+P\sin\gamma(i+\cot\gamma)}{1/\alpha-1+P\sin\gamma(-i+\cot\gamma)})-\log(\frac{1/\alpha+1+P\sin\gamma(i+\cot\gamma)}{1/\alpha+1+P\sin\gamma(-i+\cot\gamma)})\right].$$

This latter expression can be reduced, using MAPLE, into:

$$\phi_I = \frac{-2}{\pi}\left[\frac{P\sin\gamma}{1/\alpha^2-1}-2\frac{P^2\sin\gamma\cos\gamma}{\alpha(1/\alpha^2-1)^2}\right]+O(P^3). \tag{C.30}$$

On the other hand, when approaching to the origin, the factors in the integral part of equation (C.23), turn into:

$$\frac{1}{(\tau-1/\alpha-P\cos\gamma)^2+P^2\sin^2\gamma}+\frac{1}{(\tau+1/\alpha+P\cos\gamma)^2+P^2\sin^2\gamma}= \tag{C.31}$$
$$\frac{1}{(\tau-1/\alpha)^2-2P(\tau-1/\alpha)\cos\gamma+P^2}+\frac{1}{(\tau+1/\alpha)^2+2P(\tau-1/\alpha)\cos\gamma+P^2}=$$
$$\frac{1}{(\tau-1/\alpha)^2}[\frac{1}{1-2P\cos\gamma(\tau-1/\alpha)^{-1}}]+\frac{1}{(\tau+1/\alpha)^2}[\frac{1}{1+2P\cos\gamma(\tau+1/\alpha)^{-1}}]=$$
$$\frac{1}{(\tau-1/\alpha)^2}[1+2P\cos\gamma(\tau-1/\alpha)^{-1}]+\frac{1}{(\tau+1/\alpha)^2}[1-2P\cos\gamma(\tau+1/\alpha)^{-1}]=$$
$$\frac{1}{(\tau-1/\alpha)^2}+\frac{1}{(\tau+1/\alpha)^2}+2P\cos\gamma[\frac{1}{(\tau-1/\alpha)^3}-\frac{1}{(\tau+1/\alpha)^3}]=$$
$$\frac{2(\tau^2+1/\alpha^2)}{(\tau^2-1/\alpha^2)^2}+4P\cos\gamma\frac{3\tau^2\alpha^2+1}{\alpha^3(\tau^2-1/\alpha^2)^3},$$

and finally, the integral term in the potential turns into:

$$\phi_2 = -\frac{P\sin\gamma}{\pi}\int_1^{1/\alpha}\frac{2z(\tau)(\tau^2+1/\alpha^2)}{(\tau^2-1/\alpha^2)^2}d\tau \tag{C.32}$$
$$-\frac{P^2\sin\gamma\cos\gamma}{\pi}\int_1^{1/\alpha}\frac{4(3\tau^2\alpha^2+1)}{\alpha^3(\tau^2-1/\alpha^2)^3}z(\tau)d\tau.$$

Both integrals in equation (C.32) seem to diverge when $\tau = 1/\alpha$, which means that the potential ϕ_2 does not admit a Taylor expansion near the origin. Notice that this problem is actually caused by the first integral, that might be rewritten, in its original form as,

$$\phi_{2s} = \frac{-P\sin\gamma}{\pi}\int_1^{1/\alpha} z(\tau)\frac{d\tau}{(\tau - 1/\alpha - P\cos\gamma)^2 + P^2\sin^2\gamma}, \tag{C.33}$$

in which the integral part will be named F_1.

With the purpose to investigate the cause of the singularity of the integral F_1 near the origin, $\tau \to 1/\alpha$, we can define a new parameter, $\epsilon = 1/\alpha - \tau$. Notice that, using ϵ, θ_1 now reads,

$$\theta_1 = \arccos\left(\frac{\alpha^2 + 1 - 2\alpha^2(1/\alpha - \epsilon)}{1-\alpha^2}\right) = \arccos\left(-1 + \frac{4\alpha\epsilon}{1-\alpha^2} - \frac{2\alpha^2\epsilon^2}{1-\alpha^2}\right) = \tag{C.34}$$

$$= -i\log(-1 + \vartheta + i\sqrt{2\vartheta - \vartheta^2}); \quad \text{where } \vartheta = \frac{4\alpha\epsilon}{1-\alpha^2} - \frac{2\alpha^2\epsilon^2}{1-\alpha^2}. \text{ Therefore,}$$

$$\theta_1 \simeq \pi - \sqrt{2\vartheta} - \frac{\sqrt{2}}{12}\vartheta^{3/2} + O(\vartheta^{3/2}), \quad \text{which, without using } \vartheta, \text{ becomes}$$

$$\theta_1 \simeq -2\sqrt{\frac{2\alpha\epsilon}{1-\alpha^2}} - \epsilon^{3/2}\left(\frac{\sqrt{2}}{2}\sqrt{\frac{\alpha^3(\alpha^2-5)}{(1-\alpha^2)^3}} + \frac{8\sqrt{2}}{3}(\frac{\alpha}{1-\alpha^2})^{3/2}\right) + O(\epsilon^{5/2}).$$

On the other hand, θ_2 can be written as

$$\theta_2 = \arccos\left(\frac{\frac{2}{(1/\alpha-\epsilon)^2} - \alpha^2 - 1}{1-\alpha^2}\right) \simeq \tag{C.35}$$

$$\theta_2 \simeq \pi - 2\sqrt{\frac{2\alpha^3\epsilon}{1-\alpha^2}} + \sqrt{\frac{2\alpha^3}{(1-\alpha^2)^3}}\left[\frac{1}{2}\alpha(7\alpha^2-3) - \frac{8}{3}\alpha^3\right]\epsilon^{3/2} + O(\epsilon^{5/2})$$

and, in consequence, z reads,

$$z = 1 + \frac{1+H}{\pi}(\alpha\theta_1 - \theta_2) = \cancel{\left(-2\alpha\sqrt{\frac{2\alpha}{1-\alpha^2}} + 2\sqrt{\frac{2\alpha^3}{1-\alpha^2}}\right)}\epsilon^{1/2}\frac{1+H}{\pi} + O(\epsilon^{3/2}) \tag{C.36}$$

Notice that, since the first non-vanishing term in (C.36) is of $O(\epsilon^{3/2})$, the integral F_1 converges for $P = 0$ and thus, the integrand behaves near the limit $\tau = 1/\alpha$ as

$$\frac{z(\tau)}{(\tau - 1/\alpha - P\cos\gamma)^2 + P^2\sin^2\gamma} \sim \frac{\epsilon^{3/2}}{(\epsilon + P\cos\gamma)^2 + P^2\sin^2\gamma}, \tag{C.37}$$

which, when is integrated between $\epsilon = 0$ and a finite value, behaves as $\sim P^{1/2}$. This suggest that the proper expansion of F_1 might be in powers of $P^{1/2}$ rather than P.

To capture the $P^{1/2}$ term, the integral F_1 can be expanded as;

$$F_1 = -\int_1^{1/\alpha} \frac{z(1/\alpha-\epsilon)}{(\epsilon+P\cos\gamma)^2+P^2\sin^2\gamma}d\epsilon = \tag{C.38}$$
$$\int_0^{\frac{1-\alpha}{\alpha}} \frac{z(1/\alpha-\epsilon)-C_z\epsilon^{3/2}}{(\epsilon+P\cos\gamma)^2+P^2\sin^2\gamma} + C_z\int_0^{\frac{1-\alpha}{\alpha}} \frac{\epsilon^{3/2}}{(\epsilon+P\cos\gamma)^2+P^2\sin^2\gamma},$$

where C_z comes from $z(\epsilon) = C_z\epsilon^{3/2} + O(\epsilon^{5/2})$.

Notice that, the first integral of equation (C.38) can be expended in Taylor series up to terms of order P, as the numerator goes as $\sim \epsilon^{5/2}$ and the coefficients of P contain the factor ϵ^3 in the denominator.

With the above idea in mind, the parameter C_z expressed in terms of α becomes,

$$C_z = \frac{1}{\pi(1-\alpha)}[\sqrt{2}\alpha(\frac{\alpha}{(1-\alpha)^2})^{3/2}(\frac{-1}{2}(\alpha^2-5)-\frac{8}{3})- \tag{C.39}$$
$$\sqrt{2}(\frac{\alpha}{1-\alpha^2})^{3/2}\alpha(\frac{7\alpha^2-3}{2}-\frac{8}{3}\alpha^2)] =$$
$$= \frac{4\sqrt{2}\alpha^2}{3\pi(1-\alpha)}\sqrt{\frac{\alpha}{1-\alpha^2}}$$

Using now the recently obtained value of C_z, an exact solution for the second integral of F_1 can be calculated, resulting in,

$$C_z\int_0^{\frac{1-\alpha}{\alpha}} \frac{\epsilon^{3/2}}{(\epsilon+P\cos\gamma)^2+P^2\sin^2\gamma} = \tag{C.40}$$
$$2\sqrt{a^*} + \frac{P^{1/2}}{\sin\gamma}i\left[e^{i\frac{3}{2}\gamma}\arctan(\frac{\sqrt{a^*}}{P}e^{-i\gamma/2}) - e^{-i\frac{3}{2}\gamma}\arctan(\frac{\sqrt{a^*}}{P}e^{i\gamma/2})\right]$$

where $a^* = \frac{1-\alpha}{\alpha}$.
Notice that the solution (C.40) can be written in its asymptotic form yielding:

$$C_z\int_0^{\frac{1-\alpha}{\alpha}} \frac{\epsilon^{3/2}}{(\epsilon+P\cos\gamma)^2+P^2\sin^2\gamma} = \tag{C.41}$$
$$2\sqrt{\frac{1-\alpha}{\alpha}} - \pi\frac{\sin\frac{3}{2}\gamma}{\sin\gamma}\sqrt{P} + 4P\cos\gamma\sqrt{\frac{\alpha}{1-\alpha}} + O(P^{3/2})$$

C.5 Summary

As explained in the previous sections, the potential can be divided into the following contributions:

$$\phi = \phi_I + \phi_{2p} + \phi_{2m} + \phi_{2s} \tag{C.42}$$

with,

$$\phi_I = \frac{-1}{\pi}[\arctan\frac{1-1/\alpha-P\cos\gamma}{P\sin\gamma}+\arctan\frac{1+1/\alpha+P\cos\gamma}{P\sin\gamma} \tag{C.43}$$

$$\boxed{\phi_I = \frac{-2}{\pi}\frac{\alpha^2}{1-\alpha^2}P\sin\gamma+\frac{4}{\pi}\frac{\alpha^3}{(1-\alpha^2)^2}P^2\sin\gamma\cos\gamma+O(P^3)},$$

$$\phi_{2p} = -\frac{P\sin\gamma}{\pi}\int_1^{1/\alpha}\frac{z(\tau)}{(\tau+1/\alpha+P\cos\gamma)^2+P^2\sin^2\gamma}d\tau \tag{C.44}$$

$$\boxed{\phi_{2p} = -\frac{P\sin\gamma}{\pi}\int_1^{1/\alpha}\frac{z(\tau)}{(\tau+1/\alpha)^2}d\tau+\frac{2P^2\sin\gamma\cos\gamma}{\pi}\int_1^{1/\alpha}\frac{z(\tau)\alpha^3}{(\tau\alpha+1)^3}d\tau+O(P^3)}$$

$$\phi_{2m} = -\frac{P\sin\gamma}{\pi}\int_1^{1/\alpha}\frac{z(\tau)-C_z(1/\alpha-\tau)^{3/2}}{(\tau-1/\alpha-P\cos\gamma)^2+P^2\sin^2\gamma}d\tau \tag{C.45}$$

$$\boxed{\begin{aligned}\phi_{2m} = -\frac{P\sin\gamma}{\pi}\int_1^{1/\alpha}\frac{z(\tau)-C_z(1/\alpha-\tau)^{3/2}}{(\tau-1/\alpha)^2}d\tau-\\ \frac{2P^2\sin\gamma\cos\gamma}{\pi}\int_1^{1/\alpha}\frac{z(\tau)-C_z(1/\alpha-\tau)^{3/2}}{(\tau-1/\alpha)^3}d\tau+O(P^3)\end{aligned}}$$

and

$$\boxed{\phi_{2s} = -\frac{C_z}{\pi}2\sqrt{\frac{1-\alpha}{\alpha}}P\sin\gamma+C_z\sin\frac{3}{2}\gamma P^{3/2}-\frac{4}{\pi}C_z\sqrt{\frac{1-\alpha}{\alpha}}P^2\sin\gamma\cos\gamma+O(P^{5/2})} \tag{C.46}$$

The coefficients corresponding to integrals in equations (C.44) and (C.45), will be denoted as C_{p1}, C_{p2}, C_{m1} and C_{m2}. Notice that they are exclusively functions of α. Figure C.6 shows the numerical integration of these coefficients, and their variations with α. To calculate the coefficients C_{pi} and C_{mi} the numerical method tries to approximate the integral of the function from A to B to within an error of 1.e-6 using recursive adaptive Simpson quadrature. This numerical method is implemented in MATLAB (quad.m).

Once the value of the coefficients C_{p1}, C_{p2}, C_{m1} and C_{m2} has been obtained, all the contributions to the potential can be evaluated for a fixed value of H (and therefore of α). In figure C.7, the equipotential lines are plotted using the exact and the asymptotic solution. Notice that there is a very good agreement between both, specially when $R \leq 5.10^{-3}$. With this result, the next step is just to undo the mapping and come back, from the complex plane τ, to the physical one W.

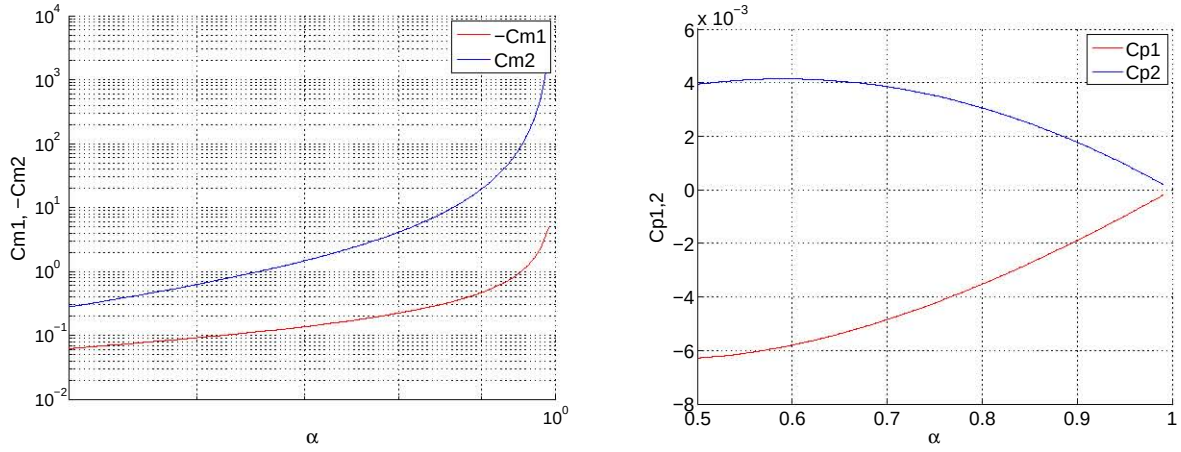

(a) (b)

Figure C.6: Numerical integration of the coefficients C_{p1}, C_{p2}, C_{m1} and C_{m2} as a function of α. For C_{m1} and C_{m2}, the integration was performed from 1 to $\frac{1-\epsilon}{\alpha}$ with $\epsilon = 10^{-5}$ to avoid the singularity and confirmed its validity until $\epsilon = 10^{-6}$. Notice that α is always bounded at 1 as $\alpha = \frac{H}{1+H}$.

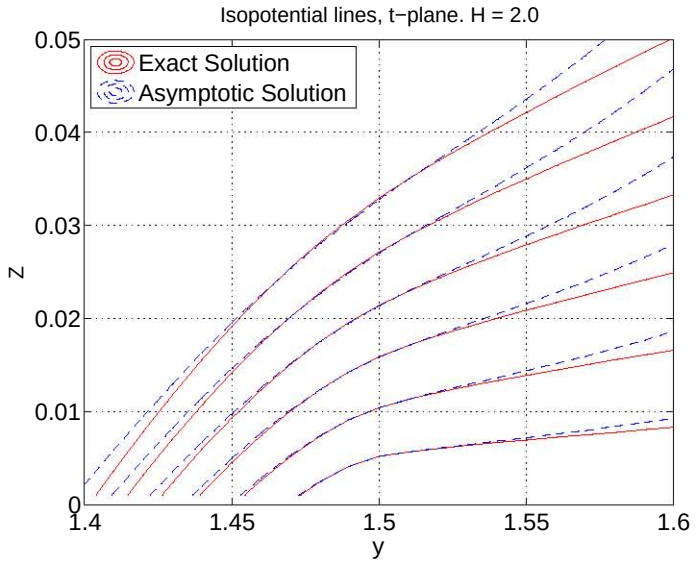

Figure C.7: Comparison of equipotential lines plotted using the exact (red) and the asymptotic solution (blue).

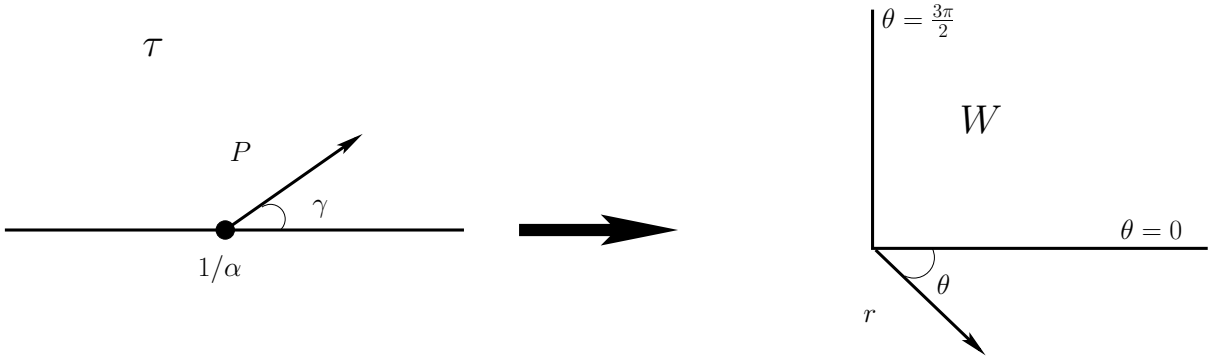

Figure C.8: Undoing the conformal mapping from τ to W.

C.6 Undoing the mapping

The previous section shows that the potential, in plane τ, can be expressed as,

$$\phi = AP\sin\gamma + BP^{3/2}\sin\frac{3}{2}\gamma + O(P^2). \tag{C.47}$$

This expression, undoing the mapping as sketched in figure C.8, will be transformed to the physical plane W. To accomplish such transformation, the Schwartz-Christoffel mapping is linearized near the corner point in both, complex and physical, planes,

$$re^{i\theta} = (Pe^{i\gamma})^{3/2}\frac{4\alpha^2}{3\pi(1-\alpha)}\sqrt{\frac{2\alpha}{1-\alpha^2}} + O(P^{5/2}) \tag{C.48}$$

$$Pe^{i\gamma} = Kr^{2/3}e^{i\frac{2\theta}{3}}; \quad \text{with} \quad K = \left(\frac{1}{\pi(1-\alpha)}\frac{4\alpha^2}{3}\sqrt{\frac{2\alpha}{1-\alpha^2}}\right)^{-2/3}$$

which, in summary, returns:

$$\boxed{P = Kr^{2/3}} \tag{C.49}$$

$$\boxed{\gamma = \frac{2}{3}\theta}$$

Notice that K depends on the dimensionless depth H by $\alpha = \frac{H}{1+H}$.
Using all the above, the final expression for the potential in the physical plane, W, reads:

$$\phi = AKr^{2/3}\sin\frac{2}{3}\theta + BK^{3/2}r\sin\theta + O(r^{4/3}). \tag{C.50}$$

It must be pointed out that, although the form of the potential could be inferred from the eigenfunctions of the problem near the corner point, knowing the constants is indeed very important and that information can only be computed following the above mentioned steps, which means to solve the global problem. In fact, when using the eigenfunction methods, $BK^{3/2} = 1$ and, using that, as sketched in figure C.8 ,in the corner

wave formulation $\theta = -\theta$, the potential reads,

$$\phi = AKr^{2/3}\sin\frac{2}{3}\theta - r\sin\theta + O(r^{4/3}). \tag{C.51}$$

With equation C.51, is now possible to obtain the normal velocities in each one of the branches near the corner point $r \to 0; \quad \theta = \{0, \quad \frac{3\pi}{2}\};$

$$\begin{aligned} \theta = 0 \to u_{n,y} &= -\frac{1}{r}\frac{\partial\phi}{\partial\theta}|_{\theta=0} = -\frac{2}{3}AKr^{-1/3} - 1 \\ \theta = \frac{3\pi}{2} \to u_{n,z} &= \frac{1}{r}\frac{\partial\phi}{\partial\theta}|_{\theta=\frac{3\pi}{2}} = -\frac{2}{3}AKr^{-1/3} \end{aligned} \tag{C.52}$$

in which, A should be negative to have physical sense. Therefore, equation C.51, defining $J = -Ak$, reads,

$$\boxed{\phi = Jr^{2/3}\sin\frac{2}{3}\theta - r\sin\theta + O(r^{4/3}),} \tag{C.53}$$

which should be recalled that is the analytical solution of the leading order φ_1 of the potential $\phi \simeq t\varphi_1$, as described in the Pressure-Impulse analysis.

Figure C.9, shows the good agreement between the normal velocities obtained with the Finite Element Method and analytical ones described by system (C.52).

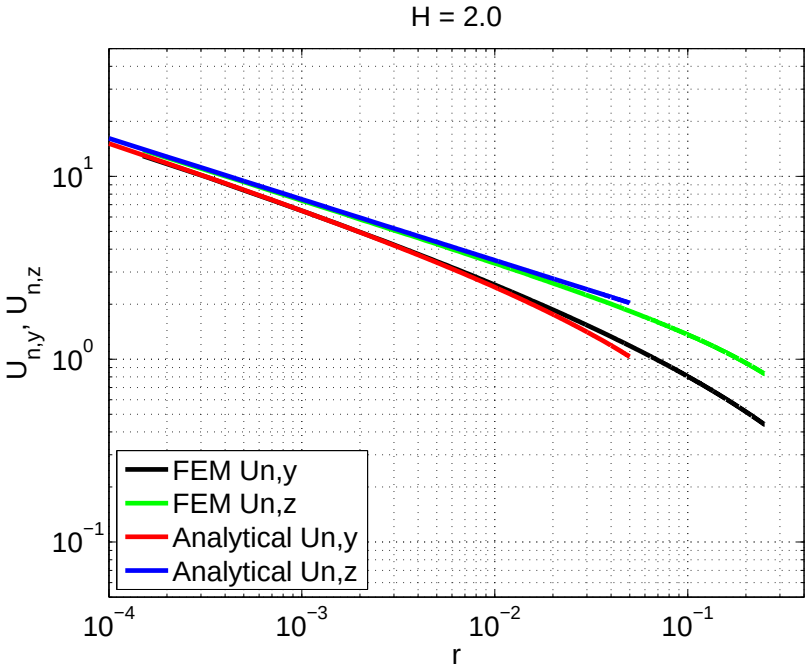

Figure C.9: Comparison between the predicted normal velocities for each branch of the corner point $(0, 0)$ using the conformal mapping (red and blue) and the results of the finite element method (black and green) for a dimensionless depth $H = 2$.

Bibliography

Abdolmaleki, K., Thiagarajan, K. P. & Morris-Thomas, M. T 2004 Simulation of the dam break problem and impact flows using a navier-stokes solver. *Proc. of the 15th Australasian Fluid Mechanics Conference. Sydney. AU.* .

Abramowitz, Milton & Stegun, Irene A. 1964 *Handbook of Mathematical Functions with Formulas, Graphs, and Mathematical Tables*, ninth dover printing, tenth gpo printing edn. New York: Dover.

Alcrudo, F. & Garcia-Navarro, P. 1993 A high-resolution godunov-type scheme in finite volumes for the 2d shallow-water equations. *International Journal for Numerical Methods in Fluids* **16**, 489–505.

Andrillon, Y. & Alessandri, B. 2004 A 2d+t vof fully coupled formulation for the calculation of breaking free-surface flow. *Journal of Marine Scice and Technology* **8**, 159–168.

Ang, W. T. 2007 *A Beginner's Course in Boundary Element Methods*. Universal Publishers.

Banner, M. L. & Peregrine, D. H. 1993 Wave breaking in deep water. *Annual Review of Fluid Mechanics* **25**, 373–397.

Batchelor, G. K. 1967 *An introduction to Fluid dynamics*. Cambridge University Press.

Benjamin, T.B. 1956 Steady flow past a sluice gate. *Journal of Fluid Mechanics* **1**, 227.

Bonmarin, P. & Ramamonjiarisoa, A. 1985 Deformation to breaking of deep water gravity waves. *Experiments in Fluids* **3**, 11–16.

Carlson, A., Kudinov, P. & Narayanan, C. 2008 Prediction of two-phase flow in small tubes: A systematic comparison of state-of-the-art cmfd codes. *Proc. of the 5th European Thermal-Sciences Conferences. The Netherlands* .

Chow, V. T. 1959 *Open-Channel Hydraulics*. Mcgraw-Hill.

Clanet, C. & Lasheras, J. C. 1997 Depth of penetration of bubbles entrained by a plunging water jet. *Physics of Fluids* **9(7)**, 1864–1866.

Drazen, D., Melville, W. K. & Lenain, L. 2008 Inertial scaling of dissipation in unsteady breaking waves. *Journal of Fluid Mechanics.* **611**, 307–332.

Duncan, J. H. 2001 Spilling breakers. *Annual Review of Fluid Mechanics* **33**, 519–547.

Duncan, J. H., Qiao, H., Philomin, V. & Wenz, A. 1999 Gentle spilling breakers: crest profile evolution. *J.Fluid Mech.* **379**, 191–222.

Fontaine, E. & Tulin, M.P. 1998 On the prediction of nonlinear free-surface flows past slender hulls using 2d+t theory: the evolution of an idea. *RTO MP-15* .

Galvin, C. J. 1968 Breaker type on three laboratory beaches. *Journal of Geophysical Research* **73**, 3651–3659.

Godunov, S. K 1959 A difference scheme for numerical solution of discontinuous solution of hydrodynamic equations. *Math. Sbornik* **47**, 271–306.

Hager, W. H. & Mazumder, S. K. 1992 Supercritical flow at abrupt expansions. *Proccedings of Institution Civil Engineers Water, Maritime and Energy* **96**, 153–166.

Hager, W. H. & Yasuda, Y. 1997 Unconfined expansion of supercritical water flow. *Journal of Engineering Mechanics* **123**, 451–457.

Harlow, F.H. & Welch, J.A. 1965 Numerical calculation of time-dependent viscous incompressible flow. *Physics of Fluids* **8**, 2182–.

Helluy, P. & Golay, F. 2005 Numerical simulations of wave breaking. *ESAIM-Mathematical Modelling and Numerical Analysis* **39**, 591–607.

Hirt, C.W. & Nichols, B.D. 1981 Volume of fluid (vof) method for the dynamics of free boundaries. *Journal of Computational Physics* **39**, 201–225.

Hirt, C. W., Cook, J.L. & Butler, T.D 1970 A lagrangian method for calculating the dynamics of an incompressible fluid with free surface. *Journal of Computational Physics* **5**, 103–.

Iafrati, A. & Broglia, R. 2010 Comparisons between 2d+t potential flow models and 3d rans for planing hull hydrodynamics. *Proceedings 25th International Workshop on Water Waves and Floating Bodies* **1**, 65–69.

Iafrati, A. & Korobkin., A. 2004 Initial stage of flat plate impact onto liquid free surface. *Physics of Fluids* **16**, 2214–2227.

Jeong, J. H. & Yang, D. Y. 1998 Finite element analysis of transient fluid flow with free surface using vof (volume-of-fluid) method and adaptive grid. *International Journal in Numerical Methods in Fluids* **26**, 1127–1154.

Kim, D-G. 2007 Numerical analysis of free flow past a sluice gate. *KSCE Journal of Civil Engineering* **11(2)**, 127–132.

Kurganov, A. & Tadmor, E. 2000 New high-resolution central schemes fo nonlinear conservation laws and convection-diffusion equations. *Journal of Computational Physics* **160**, 241–282.

Longuet-Higgins, M. 1995 On the disintegration of the jet in a plunging breaker. *Journal of Physical Oceanography* **25**, 2458–2462.

Longuet-Higgins, M.S 2001 Vertical jets from standing jets. *Phil. Trans. R. Soc. Lond.* **A 457**, 495–510.

Longuet-Higgins, M.S & Oguz, H. N. 1997 Critical jets in surface waves and collapsing cavities. *Phil. Trans. R. Soc. Lond.* **A 355**, 625–639.

Molland, A. 2008 *The Maritime Engineering Reference Book*. Butterworth-Heinemann.

Montes, J.S. 1997 Irrotational flow and real fluid effects under planar sluice gates. *Journal of Hydraulic Engeneering-ASCE* **123**, 219–232.

Munk, M.M. 1924 The aerodynamic forces on airship hulls. *NACA Rept.* **184**, –.

Naghdi, P.M. & Vongsrnpigoon, L. 1986 Steady flow past a sluice gate. *Physics of Fluids* **29(12)**, 3962–3970.

Nakayama, T. 1990 A computational method for simulating transient motions of an incompressible inviscid fluid with a free surface. *International Journal in Numerical Methods in Fluids* **10**, 683–695.

Needham, D. J., Billingham, J. & King, C. 2007 The initial development of a jet caused by fluid,body and free-surface interaction. part 2. an impulsively moved plate. *J. Fluid Mech.* **578**, 67–84.

Newman, J.N. 1977 *Marine hydrodynamics*. Cambridge, Massachusetts: MIT Press.

Nichols, B.D & Hirt, C. W. 1971 Calculating three-dimensional free surface flows in the vicinity of submerged and exposed structures. *Journal of Computational Physics* **12**, 234–.

Nichols, B.D & Hirt, C. W. 1974 An arbitrary lagrangian-eulerian computing method for all flow speeds. *Journal of Computational Physics* **14**, 227–.

Nichols, B.D & Hirt, C. W. 1975 Methods for calculating multidimensional, transient free surface flows past bodies. *Conference on Numerical Ship Hydrodynamics Gaithersburg, ML, Oct. 20-23* .

Nichols, B.D & Hirt, C. W. 1980 Numerical simulation of bwr vent-clearing hydrodynamics. *Nuclear Science Engineering* **73**, 196–.

Ogilvie, T. F. 1967 Nonlinear high-froude-number free-surface problems. *Journal of Engineering Mathematics* **1(3)**, 215–235.

Peregrine, D. H. 1971 A ship's waves and its wake. *Journal of Fluid Mechanics.* **49**, 353–360.

Pozrikidis, C. 1997 *Introduction to theoretical and computational fluid dynamics*. Oxford University Press.

Pozrikidis, C. 2002 *A practical guide to boundary element methods with the software library BEMLIB*. Chapman and Hall/ CRC.

Rapp, J. H. & Melville, W. K. 1990 Laboratory measurements of deep-water breaking waves. *Philosophical Transactions of the Royal Society of London* **331**, 735–800.

Rodríguez-Rodríguez, J., Marugán, C., Aliseda, A. & Laheras, J. C. 2011 Dynamics of large turbulent structures in a steady breaker. *Experimental Thermal and Fluid Science* **35**, 301–310.

Roth, A. & Hager, W. H. 1999 Underflow of a standar sluice gate. *Experiments in Fluids* **27**, 339–350.

Schultz, W. W., Huh, J. & Griffin, O. M. 1994 Potential energy in steep and breaking waves. *Journal of Fluid Mechanics.* **278**, 201–228.

Shakeri, M., Maxeiner, E., Fu, T. & H.Duncan, J. 2009*a* An experimental examination of the 2d+t approximation. *Journal of Ship Research.* **53**, 59–67.

Shakeri, M., Tavakolinejad, M. & H.Duncan, J. 2009*b* An experimental investigation of divergent bow waves simulated by a 2d+t technique. *Journal of Fluid Mechanics.* **634**, 217–243.

Sobolev, S. L. 2005 *Some Applications of Functional Analysis in Mathematical Physics*. American Mathematical Soc.

Sorensen, R. M. 1966 *Ship Waves*. University of California, Berkeley.

Spalart, P. R., Moser, R. D. & Rogers, M. M. 1991 Spectral methods for the navier-stokes equations with one infinite and two periodic directions. *Journal of Computational Physics* **96**, 297–324.

Storr, G.J. & Behnia, M. 2000 Comparisons beteen experiment and numerical simulation using a free surface technique of free-faling liquid jets. *Experiments in Thermal and Fluid Science* **22**, 79–91.

Sumer, B. M. & Fredsoe, J. 1997 *Hydrodynamics around cylindrical strucures*. World Scientific.

Tsai, Wu Ting & Yue, Dick K.P. 1996 Computation of non-linear free surface flows. *Annual Review of Fluid Mechanics* **28**, 249–278.

Tulin, M.P. 1957 Theory of slender surface planing at high speeds. *Schiffstechnik, 14.* **Heft 21**, 125–133.

Tulin, M. P. & Wu, M. 1997 Divergent bow waves. *Proccedings of the 21th Symposium on Naval Hydrodinamics.* **1**, 661–669.

Vanden-Broeck, J-M. 1986 Flow under a gate. *Physics of Fluids* **29(10)**, 3148–3151.

Wagner, H. 1932 über stoβ und gleitvorgänge ander oberfläche von flüssigkeiten. *ZAMM.* **12**, 193–215.

Wood, D. J., Pedersen, G. K. & Jensen, A. 2003 Modelling of run up steep non-breaking waves. *Ocean Engineering* **30**, 625–644.

Wright, T. 1983 *Ship Hydrodynamics*. PhD Thesis, University of Manchester.

Yeung, R. W. 1982 Numerical methods in free-surface flows. *Annual Review of Fluid Mechanics* **14**, 394–442.